

Millimeter-Wave Transmitarray and Reflectarray Antennas for Communications Systems

Mei, Peng

DOI (link to publication from Publisher):
[10.54337/aau456472446](https://doi.org/10.54337/aau456472446)

Publication date:
2021

Document Version
Publisher's PDF, also known as Version of record

[Link to publication from Aalborg University](#)

Citation for published version (APA):
Mei, P. (2021). *Millimeter-Wave Transmitarray and Reflectarray Antennas for Communications Systems*. Aalborg Universitetsforlag.

General rights

Copyright and moral rights for the publications made accessible in the public portal are retained by the authors and/or other copyright owners and it is a condition of accessing publications that users recognise and abide by the legal requirements associated with these rights.

- Users may download and print one copy of any publication from the public portal for the purpose of private study or research.
- You may not further distribute the material or use it for any profit-making activity or commercial gain
- You may freely distribute the URL identifying the publication in the public portal -

Take down policy

If you believe that this document breaches copyright please contact us at vbn@aub.aau.dk providing details, and we will remove access to the work immediately and investigate your claim.

MILLIMETER-WAVE TRANSMITARRAY AND REFLECTARRAY ANTENNAS FOR COMMUNICATIONS SYSTEMS

**BY
PENG MEI**

DISSERTATION SUBMITTED 2021



AALBORG UNIVERSITY
DENMARK

AALBORG UNIVERSITY
DEPARTMENT OF ELECTRONIC SYSTEMS,
ANTENNAS, PROPAGATION, AND MILLIMETER-WAVE SYSTEMS
SECTION

PH.D. THESIS

MILLIMETER-WAVE TRANSMITARRAY AND
REFLECTARRAY ANTENNAS FOR
COMMUNICATIONS SYSTEMS

PENG MEI

AALBORG, 2021

Dissertation submitted: August 2021

PhD supervisor: Prof. Gert Frølund Pedersen
Department of Electronic Systems
Aalborg University

Ph.D. Co-supervisor: Assoc. Prof. Shuai Zhang
Department of Electronic Systems
Aalborg University

PhD committee: Professor Søren Bech (chairman)
Aalborg University

Professor Niels Kuster
Eidgenössische Technische Hochschule Zürich (ETH)

Professor Jorge Rodrigues da Costa
University Institute of Lisbon

PhD Series: Technical Faculty of IT and Design, Aalborg University

Department: Department of Electronic Systems

ISSN (online): 2446-1628
ISBN (online): 978-87-7210-985-5

Published by:
Aalborg University Press
Kroghstræde 3
DK – 9220 Aalborg Ø
Phone: +45 99407140
aauf@forlag.aau.dk
forlag.aau.dk

© Copyright: Peng Mei

Printed in Denmark by Rosendahls, 2021

Contents

Abstract	vi
Resume	viii
Preface	x
Thesis Details	xii
Part I	1
Introductory Chapters	1
1. Introduction	3
1.1 Motivations	3
1.2 Aims of the thesis	10
2. General knowledge and discussions	13
2.1 Transmitarray/Reflectarray antenna	13
2.2 Phase quantization	16
2.3 Reconfigurable antenna	20
2.3.1 Polarization reconfigurable	21
2.3.2 Radiation pattern reconfigurable	24
2.4 Fabry-Perot antenna	28
2.5 Folded transmitarray antenna	30
2.6 Dual-band reflectarray antenna	32
3. Contributions	34
3.1 Paper A	35

3.2 Paper B	36
3.3 Paper C	38
3.4 Paper D	39
3.5 Paper E	40
4. Conclusion.....	42
References	44
Part II Papers	57
Paper A.....	59
Paper B	75
Paper C	91
Paper D.....	117
Paper E	147

Abstract

It is an inevitable trend to investigate and develop millimeter-wave technologies for communications systems as millimeter-wave can provide high data rate, broad channel capacities, etc., compared to the microwave band. This thesis mainly involves five millimeter-wave antennas with different performance such as wideband, polarization-reconfigurable, beam-steerable, etc. These antennas are implemented based on the forms of transmitarray and reflectarray antennas to cope with the increasingly complex electromagnetic environments and various application scenarios.

A wideband transmitarray antenna is proposed based on polarization-rotating elements. Two elements with different configurations are designed to offer a 2-bit transmission phase in a wide band with high transmission efficiency without resizing their dimensions. A wideband 3-D printed reflectarray antenna is studied with mechanically reconfigurable polarization by using dielectric-based elements. Four elements are proposed to provide a 90-degree out of phase for transverse electric (TE) and transverse magnetic (TM) incidence waves and a 2-bit reflection phase simultaneously. By rotating the reflective panel that is implemented with the proposed four elements, the proposed reflectarray antenna is capable of offering linear polarization (LP), left-hand circular polarization (LHCP), and right-hand circular polarization (RHCP) in a wide band. Different from the currently beam-steerable reflectarray antennas enabled by loading PIN diodes, a low-cost, high-efficiency, and full-metal reflectarray antenna is studied to achieve 2D beam-steerable capabilities. A full-metal element is proposed to provide a 1-bit reflection phase for TE and TM incidence waves. By mechanically controlling the rotation of each element, the proposed reflectarray antenna will be able to achieve flexible beams as expected.

Dual-band and triple-band shared-aperture antennas are firstly developed with high figures of merit by combining the transmitarray/reflectarray and Fabry-Perot antennas. These shared-aperture antennas provide solutions to achieve dual-polarization, low loss, simple configuration, high aperture reuse efficiency, and the number of the operating bands in the designs of shared-aperture antennas.

Resume

Det er en uundgåelig tendens at undersøge og udvikle millimeter-bølgelængde antenne teknologien til kommunikations systemer da millimeter-bølgelængder ville kunne opnå høje data overførselsagtigheder, bred kanal kapacitet osv. sammenlignet med mikrobølge båndene. Denne afhandling omhandler fem millimeter-bølgelængde antenner med forskellige funktioner såsom eksempelvis bredbåndet, polarisering konfigurerbar, strålescanning, osv. Disse antenner er implementerede baseret på transmitterarray og reflektionsarray formen til at kunne klare komplekse elektromagnetiske miljøer og forskellige applikationsscenarie.

En bredbåndet transmitarray antenne foreslås baseret på polarisering-roterende elementer. To elementer med forskellige konfigurationer er designet til at tilbyde en 2-bits fase transmission i et bredt bånd med høj transmissions effektivitet uden at ændre deres størrelse. En bredbåndet 3-D printet reflektionsarray antenne er udviklet med en mekanisk konfigurerbar polarisering ved brugen af dielektriske baserede elementer. Fire elementer er foreslået til at give en 90-graders ud-af-fase til tværgående elektrisk (TE) og tværgående magnetiske indfaldene bølger samtidig med en 2-bits fase refleksion. Ved at rotere refleksions panelet er den foreslåede reflektionsarray antenne i stand til at tilbyde lineær polarisering, venstrehånds polarisering eller højrehånds polarisering i et bredt bånd. Forskelligt fra de nuværende stråle-scannings reflektionsarray antenner fungerende med PIN-dioder, er der her undersøgt en billig, effektiv og full-metal reflektionsarray antenne til at opnå 2D stråle-scanning. Et full-metal element er foreslået til at give en 1-bit fase refleksion af TE og TM indkommende bølger. Ved mekanisk at kontrollere rotationen af hvert element kan det foreslåede reflektionsarray antenne opnå fleksible antenneudstråling.

Dobbeltbånds- og tredobbelt-bånds antenner med delt udstrålingsområde er udviklet med høj fortjeneste ved at kombinere transmitterarray- eller reflektionsarray-antenne med en Fabry-Perot-antenne. Disse antenner med delt udstrålingsområde giver løsningen til at opnå en antenne med double-polariseret, lav omkostninger, simple konfigurerbar, høj område genanvendelses effektivitet, og med flere operation bånd.

Preface

First of all, I would like to thank my supervisor Prof. Gert Frølund Pedersen for offering me funds to pursue my Ph.D. degree and unconditional support for my career plan. My deep appreciations go to my co-supervisor Associate Prof. Shuai Zhang, who helped me when I was at my hardest time and gave me lots of freedom to do my research. Best wishes to my supervisors.

I am indebted to Dr. Kun Zhao and Dr. Zhinong Ying from the Sony Research Center, Lund, Sweden, for their kind help in hosting online collaboration.

Many thanks go to our laboratory engineers: Ben Krøyer, Kim Olesen, and Kristian Bank, for their generous help in the fabrication and measurement of the antenna prototypes.

I would like to thank my friends at Aalborg, Denmark. Every moment that I talk to, work, or play with them enriches my life outside my academic research.

Finally, and most importantly, I am deeply grateful to my beloved family members: my parents, my sisters, my brothers-in-law, and my lovely niece and nephews for their constant love. As the youngest child in my family, I always receive lots of love and care from my family members. I will you all the best.

Peng Mei
Aalborg University, June, 2021

Thesis Details

Thesis Title: Millimeter-Wave Transmitarray and Reflectarray
 Antennas for Communications Systems
Ph.D. Candidate: Peng Mei
Supervisors: Prof. Gert Frølund Pedersen - Aalborg University
 Assoc. Prof. Shuai Zhang - Aalborg University

This thesis is submitted as part of the requirements for the degree of Doctor of Philosophy (Ph.D.) from Aalborg University, Denmark. The thesis is compiled as a collection of papers, resulting in a short introduction and the main part of the thesis being scientific papers published in peer-reviewed journals. The work presented in the thesis is the result of two years and two months of research, in the period May 2019 – June 2021, as a Ph.D. fellow in the Section of Antennas, Propagation, and Millimeter-Wave Systems (APMS), Department of Electronic Systems, Aalborg University, Denmark.

The Ph.D. stipend (nr. 8-17073) has been funded as a part of the RANGE project.

The main body of this thesis consists of the following papers:

- A. P. Mei**, G. F. Pedersen, and S. Zhang, “A Broadband and FSS-Based Transmitarray Antenna for 5G Millimeter-Wave Applications,” *IEEE Antennas and Wireless Propagation Letters*, vol. 20, no. 1, pp. 103-107, Jan. 2021.
- B. P. Mei**, S. Zhang, and G. F. Pedersen, “A Wideband 3-D Printed Reflectarray Antenna with Mechanically Reconfigurable Polarization,” *IEEE Antennas and Wireless Propagation Letters*, vol. 19, no. 10, pp. 1798-11802, Oct. 2020.
- C. P. Mei**, S. Zhang, and G. F. Pedersen, “A Low-Cost, High-Efficiency and Full-Metal Reflectarray Antenna with Mechanically 2-D Beam-Steerable Capabilities for 5G Applications,” *IEEE Transactions on Antennas and Propagation*, vol. 68, no. 10, pp. 6997-7006, Oct. 2020.

- D. P. Mei**, S. Zhang, and G. F. Pedersen, "A Dual-Polarized and High-Gain X-/Ka-Band Shared-Aperture Antenna with High Aperture Reuse Efficiency," *IEEE Transactions on Antennas and Propagation*, vol. 69, no. 3, pp. 1334-1344, Mar. 2021.
- E. P. Mei**, X. Q. Lin, G. F. Pedersen, and S. Zhang, "Design of A Triple-Band Shared-Aperture Antenna with High Figures of Merit," *IEEE Transactions on Antennas and Propagation, Early Access*, DOI: 10.1109/TAP.2021.3090837

According to the Ministerial Order no. 1039 of August 27, 2013, regarding the Ph.D. Degree § 12, article 4, statements from each co-author about the Ph.D. student's contribution to the above-listed papers have been provided to the Doctoral school for approval prior to the submission of this thesis. These co-author statements have also been presented to the Ph.D. committee and included as a part of their assessment.

In addition to the above-listed papers as the main content of this thesis, the following papers were also authored and co-authored during the Ph.D. studies. Since these papers are not a part of the main body of this thesis, they have not been included in the print. The reader is, therefore, kindly referred to the respective publishing channels as listed hereafter.

Journals:

- 1. P. Mei**, Y. M. Zhang, and S. Zhang, "Decoupling of a Dual-Polarized, Wideband, and Large-Scale Antenna Array with Dielectric Stubs," *IEEE Transactions on Vehicle and Technology*, vol. 70, no. 8, pp. 7363-7374, Aug. 2021.
- 2. P. Mei**, S. Zhang, and G. F. Pedersen, "A Low-Profile and Beam-Steerable Transmitarray Antenna: Design, Fabrication, and Measurement," *IEEE Antennas Propagation Magazine*. (In press)
- 3. P. Mei**, S. Zhang, X. Q. Lin, and G. F. Pedersen, "Design of an Absorptive Fabry-Perot Polarizer and Its Application," *IEEE Antennas and Wireless Propagation Letters*, vol. 18, no. 7, pp. 1352-1356, July. 2019.
- 4. P. Mei**, S. Zhang, X. Q. Lin, and G. F. Pedersen, "A Millimeter-Wave Gain-Filtering Antenna Design Using a Hybrid Lens," *IEEE Antennas Wireless and Propagation Letters*, vol. 18, no. 7, pp. 1362-1366, July. 2019.

5. **P. Mei**, S. Zhang, Y. Cai, X. Q. Lin, and G. F. Pedersen, “A Reflectarray Antenna Designed with Gain Filtering and Low-RCS Properties,” *IEEE Transactions on Antennas and Propagation*, vol. 67, no. 8, pp. 5362-5371, Aug. 2019.

Conferences:

1. S. S. Zhekov, **P. Mei**, W. Fan, and G. F. Pedersen, “Water-Based Dual-Band Metamaterial Absorber,” *15th European Conference on Antennas and Propagation (EuCAP)*, 2021, 1-5.
2. **P. Mei**, S. Zhang, X. Q. Lin, and G. F. Pedersen, “Retrieval of Effective Permittivity and Permeability of Periodic Structures on Dielectric and Magnetic Substrates,” *14th European Conference on Antennas and Propagation (EuCAP)*, 2020, 1-5.
3. **P. Mei**, S. Zhang, X. Q. Lin, and G. F. Pedersen, “A Low-Profile Patch Antenna with Monopole-Like Radiation Patterns,” 2019 *IEEE-APS Topical Conference on Antennas and Propagation in Wireless Communications (APWC)*, 2019.

Patent:

1. **P. Mei**, S. Zhang, Z. Xu, and G. F. Pedersen, “MIMO Antenna Array Decoupler,” (WO-patent pending and filed by Huawei)

Part I

Introductory Chapters

1. Introduction

1.1 Motivations

Communication techniques have always upgraded with the developments and emergence of new technologies. In ancient times, people communicated with their friends or family by flying pigeons, which was unstable and not instant. The emergence of radio waves offers a possible solution for wireless communication with others. Guglielmo Marconi carried out a series of wireless communications in 1897, accelerating the applications of radio waves in wireless communications. At that time, the frequencies of the radio waves were low (around the order of kHz). With the developments of solid components and circuits, the operating frequencies of radio waves are increasingly high. The high frequencies can provide wide channel capacity according to the Shannon Theorem. In the past several decades, wireless communications have been updated from first-generation (1G) to fifth-generation (5G). The allocations of the operating frequencies of 1G to 4G are mainly microwave bands, while 5G is broadly subdivided into the microwave and millimeter-wave bands. The era of 5G millimeter-wave is coming and being deployed gradually around the globe. Compared to the microwave band, millimeter-wave is highlighted by its extremely high wireless data transmission speed due to its widely absolute bandwidth. As a result, it can be potentially used in IEEE 802.11ad WiGig technology, virtual reality headsets, security check applications at airports, satellite and radar communications, automotive communication, and smart city, as shown in Fig. 1.1 to offer high-quality and reliable communications and connections.

Antennas, serving as components to receive and transmit electromagnetic (EM) waves, are indispensable in wireless communication systems. Unlike the EM waves at the microwave band, the propagation loss in free space is significant at the millimeter-wave and it would be extremely high at some certain frequencies due to the existence of the atmospheric window. To this end, it is a good solution to use high gain millimeter-wave antennas to

compensate for the free space path loss to ensure the signal strengths that deliver to receivers. In particular, high-gain millimeter-wave antennas are preferred for long-distance communications such as satellite to ground communications, inter-satellite communications, etc.

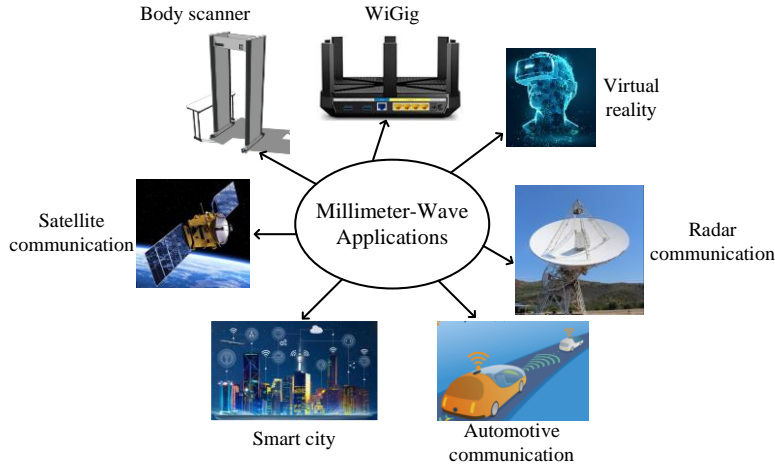


Fig. 1.1. The applications scenarios of millimeter-wave

There are already some technologies to achieve high gain millimeter-wave antennas such as horn antenna, planar antenna array, parabolic antenna, transmitarray/reflectarray antenna, etc., every type of which has its respective pros and cons:

- **Horn antenna:** The bandwidth of a horn antenna is wide. The gain of a horn antenna is closely related to its dimension. If a high gain is desired, the profile and aperture of the horn antenna will be large accordingly. Due to the metal structure of a horn antenna, the efficiency and power handling of horn antennas are high;
- **Planar antenna array:** The bandwidth of a planar antenna array is typically limited. The bandwidth is associated with the specific feeding approaches (e.g., aperture-coupling, direct feeding, etc.) and the type of antenna element (e.g., microstrip patch antenna element, slot antenna element, magnetoelectric antenna element, etc.). The gain of a planar antenna array is becoming higher with the size of the antenna array (the number of antenna elements). For a planar antenna array, a feeding network is necessary to excite all antenna elements to achieve a high gain. The feeding network will be complicated and lossy for a dual/circularly-polarized or large-scale antenna array at the millimeter-wave band. Planar antenna arrays implemented with PCB

technologies have low efficiency and power handling abilities. By contrast, planar antenna arrays based on gap waveguide technologies are more competitive in efficiency and power handling;

- **Parabolic antenna:** The bandwidth is wide, the gain can be very high, and efficiency and power handling are high. However, parabolic antennas suffer from the bulky volume, heavy mass, and complicated curved surfaces with a typically cross-sectional shape of a parabola. The bandwidth and gain are highly related to the specific curvature of the curved surface;
- **Transmitarray/reflectarray antenna:** The bandwidth can be wide if the elements implementing the phase-shifting surfaces are properly designed, and the gains of transmitarray/reflectarray antennas could be very high. Compared to the planar antenna arrays, complicated feeding networks can be avoided to achieve a high gain, and the dual/circular polarization can be obtained by simply adopting a dual/circular feed source and symmetrical elements. The main drawback for the transmitarray/reflectarray antennas lies in the relatively high profile compared to the planar antenna arrays;

A horn antenna typically consists of a flared waveguide and a standard waveguide, where the standard waveguide is for exciting the flared waveguide. In [1], the authors carried out a theoretical analysis on the mechanisms of a horn antenna from Maxwell's equations viewpoint, where it was concluded that the dimensions of flared waveguide (length, flare angle) are in high association with the bandwidth and gain of the horn antenna. Specifically speaking, there is always an optimum flare angle and a constant length for which the gain is highest. The gain of a horn antenna can reach 25dBi, but with a typical value of 10 - 20dBi.

The antenna array is a straightforward and widely used technique to achieve high gain by properly arranging the antenna elements in a one- or two-dimensional manner, corresponding to a linear and planar array, respectively [2]-[17]. By exciting antenna elements in-phase, the electric fields emanating from antenna elements are superimposed in the far-field, thereby resulting in a high gain. The bandwidth of a planar antenna array is associated with the type of antenna element and the specific feeding approach. Microstrip patch and slot antennas are generally acknowledged as resonant-type antennas with narrow bandwidths. In [2], the authors designed a 4×4 microstrip patch antenna array at the millimeter-wave band for energy harvesting application, where 4×4 patch antenna elements were directly excited by a microstrip-

based feeding network. The bandwidth ($|S_{11}| < -10\text{dB}$) of the antenna array is around 2.8 %. In [9], a single-layer SIW slot antenna array was proposed by using a CPW center-fed technique, where 32×4 slot elements were included and excited by a CPW feeding network directly. The proposed slot antenna array could achieve a gain of large than 22.8 dBi over 24.05 – 24.25 GHz. The impedance bandwidth of the proposed slot antenna array was 23.85 – 24.15 GHz, corresponding to a fractional bandwidth of 1.25%. A 12×12 slot array based on the SIW scheme was reported in [12] for 60 GHz band applications with an impedance bandwidth of 4.16%, where a one to twelve power divider was incorporated to excite every 12×1 slot array directly.

The aperture-coupling feeding technique effectively achieves a wideband antenna array [13]-[15], where the corresponding antenna arrays are usually multilayer. A wideband slot-coupled patch antenna array was reported in [15] for X/Ku-band multimode radars, where a bowtie-shaped slot was etched on the metal ground to couple the electromagnetic waves from the feeding line to the radiating patch. The fractional bandwidth of the patch antenna array was around 44%, which is wider than the direct feeding technique. The aperture-coupling technique is also used in the millimeter-wave gap (ridge)-waveguide-based antennas [16]-[18]. In [16], a wideband patch antenna array using gap waveguide technologies was reported for 60-GHz applications, where a coupling slot was used to direct the electromagnetic waves from the gap waveguide to the patch antenna array. A bandwidth of $|S_{11}|$ below -10dB was around 15.5 % for the patch antenna array.

Unlike microstrip patch and slot antennas, the bandwidth of the magnetoelectric dipole antenna was wide [19], [20]. Using magnetoelectric dipole antennas as elements to implement an antenna array, the bandwidth of such antenna array would be wide [21]-[23]. In [22], the authors designed a wideband antenna array with magnetoelectric dipole antenna elements. The proposed antenna array can reach a fractional bandwidth of 53.7% by exciting the antenna elements through the aperture-coupling technique.

A parabolic antenna, according to its configuration, is composed of a parabolic reflector and a feed source [24]-[26]. The parabolic reflector is a parabola-shaped curved surface, and the feed source usually locates at the focal point of the parabolic reflector. When the parabolic antenna serves as a transmitting antenna, the feed source at the focal point illuminates the parabolic reflector first. The propagating electromagnetic waves will be reflected into a pencil beam in the boresight direction. By contrast, an incoming plane wave from free space will be focused at the focal point of the

parabolic reflector according to the antenna reciprocity theorem when the parabolic antenna is viewed as a receiving antenna. The feed source is usually a low-gain type antenna such as patch antenna, open-ended waveguide, horn antenna, etc. The gain of a parabolic antenna can be extremely high when the size of the parabolic reflector is electrically large in terms of wavelength at the frequency of interest.

In general, reflectarray antennas can be viewed as derivations of the parabolic antennas, where the parabolic reflector was replaced with a planar phase-shifting surface to convert the spherical wave from the feed source to a plane wave [27]. The operating principle of a reflectarray antenna can still apply for a transmitarray antenna that is also composed of a feed source and a phase-shifting surface. For a transmitarray antenna, the phase-shifting surface is transparent, meaning that the electromagnetic waves can propagate through it freely. Therefore, the feed source and the focused beam of a reflectarray antenna are on the same sides of the phase-shifting surface, while they are located at the two different sides of the phase-shifting surface for a transmitarray antenna.

The bandwidth of a reflectarray antenna is highly related to the performance of the unit cells [28]. The single-layer microstrip patch with variable size or rotation angle was a popular unit cell to implement a reflectarray antenna [29]-[31]. By varying the size or rotation angle of the microstrip patch, its reflection phase was changed accordingly. However, the bandwidth of such reflectarray antenna was narrow since the microstrip patch unit cell was at its resonant state. To enhance the bandwidth of a reflectarray antenna, some modifications and improvements on the unit cells have been developed, such as multilayer unit cell [32]-[35], phase-delay-line-based unit cell [36]-[38], and single-layer double rings unit cell [39]-[42]. The principles of using multilayer or single-layer double rings unit cells are introducing one more resonance to make the phase shift of the unit cell smoother, thereby broadening the bandwidth of the corresponding reflectarray antenna. In [35], a wideband reflectarray antenna was designed by using double-layer subwavelength patch elements, resulting in a 1-dB gain bandwidth of 19.1%. A quasi-spiral phase-delay-line-based unit cell was proposed to implement a broadband reflectarray antenna [37]. The reflectarray antenna achieved a 1-dB bandwidth of 16.5%. A wideband microstrip reflectarray antenna operating at the millimeter-wave band enabled by dual-resonance unit cells was reported in [42], demonstrating a 1-dB gain bandwidth of greater than 29.3%. Some non-resonant structures such as dielectric-based unit cells could

be utilized to enhance the bandwidth of a reflectarray antenna [43]-[45]. In [43], the authors designed a unit cell based on a cubic-shaped dielectric stub, where the reflection phase of the unit cell was controlled by tuning the height of the cubic-shaped dielectric stub. A reflectarray antenna was implemented then based on the cubic-shaped dielectric stubs, where a 3dB gain bandwidth of 20.66% was achieved. The dielectric-based reflectarray antennas could be massively produced with low-cost and efficient 3D printing technology.

Likewise, the bandwidth of a transmitarray antenna is also closely associated with the performance of the unit cells. In [46], the authors have proven that a four-layered, metallic double-square unit cell can offer both a full phase-cycle (2π) and an acceptable attenuation (less than 1 dB) [46]. For a four-layered and double-ring unit cell, a 360-degree transmission phase coverage can be obtained by tuning the dimensions of the double rings (e.g., the radius of the ring). However, the passband is also shifted simultaneously, leading to a narrow bandwidth of the overlapping passband within the 360-degree transmission phase coverage. The narrow bandwidth is the natural characteristic of the resonance-based unit cell. The bandwidth of a transmitarray antenna can be improved by optimizing the unit cell structures [46]-[51]. Very recently, the phase quantization was applied on the transmission phases of the unit cells, where 1-bit ($0, \pi$), 2-bit ($-\pi, -\pi/2, 0, \pi/2$), or 3-bit ($-\pi, -3\pi/4, -\pi/2, -\pi/4, 0, \pi/4, \pi/2, 3\pi/4$) phase quantization was usually adopted to replace the continuous phase to enhance the bandwidth of a transmitarray antenna. The phase quantization, of course, will introduce extra phase errors, resulting in a gain reduction of the corresponding transmitarray antenna. However, the reduced gain can be compensated back from the small attenuations of unit cells due to the phase quantization. Many wideband transmitarray antennas have been developed using 1-bit or 2-bit phase quantization [52]-[57]. The polarization-rotating structure is a perfect candidate to perform the phase quantization as it naturally offers a 1-bit phase quantization, by rotating a certain metallic layer 90 degrees with the dimensions of the structure fixed. In [53], the authors designed two transmitarray antennas by utilizing 1-bit and 2-bit phase quantization, respectively. The measured results demonstrated that it could achieve 3-dB gain bandwidth and maximum gain were 33.4% and 24.5dBi for the 1-bit phase quantization prototype, respectively. By contrast, the 3-dB gain bandwidth and maximum gain were 24.1% and 27.2dBi for the 2-bit phase quantization prototype, respectively. The unit cell based on dielectric material is another solution to implement wideband transmitarray antennas as the dielectric-based unit cells are non-resonant structures [58]-[60]. In [60], the

authors proposed a three-layer unit cell based on a dielectric material, a 1dB gain bandwidth of 21.5 was achieved for the corresponding transmitarray antenna. The dielectric-based transmitarray antennas can be produced with 3D printing technology as well.

For dual- or circularly-polarized reflectarray/transmitarray antennas, the phase-shifting surfaces should be implemented with symmetrical unit cells and were illuminated by the corresponding dual- or circularly-polarized feed source, thereby avoiding using any complicated and lossy feeding networks.

On the other hand, millimeter-wave antennas are also required to be capable of steering their radiation beams to accommodate the increasingly complex electromagnetic environments and application scenarios such as wireless communications with mobile users. The first technology that came to mind is the phased array, where each antenna element was connected to a phase shifter. By tuning the phase shift of each phase shifter, the phased array can provide 2D steerable beams [61]-[63]. The main drawbacks of the phased array lie in bulky volume, high loss, and high cost, which limit its applications to some extent. Some other technologies have been developed to steer the radiation beams in different architectures such as SIW slot array fed by the beam-forming network [64]-[68], Luneburg lens fed by multiple feed sources [69]-[71], reflectarray antenna illuminated by multiple feed sources [72]-[76], reconfigurable reflectarray antennas enabled by PIN diode loaded or mechanical-rotation-based unit cells [77]-[83]. Among them, the SIW slot array fed by the beam-forming network was typically capable of 1D scanning beam [64]-[66]. It could also perform 2D beam steering by using a more complicated beam-forming network (high-order Butler matrix) [67], [68]. However, the 2D scanning coverage was limited due to the ability of the beam-forming network. The Luneburg lens was highlighted by its extremely stable gain (very minor gain roll-off) within the entire scanning coverage and large scan angle. However, the architectures of the Luneburg lens make it only suitable for 1D beam steering. A reflectarray antenna illuminated by multiple feed sources could achieve beam steering, where the number and relative positions of the feed sources determine the number and scanning resolution of the radiation beams. A noticeable gain drop exists for such beam-steerable reflectarray antennas, while the gain drop can be reduced and minimized by optimizing the phase-shifting surfaces using bifocal synthesis. The beam-steerable reflectarray antenna reported in [72]-[76] can only perform 1D beam steering as a linear antenna array was adopted as the multiple feed sources. Reconfigurable reflectarray antennas enabled by PIN diode loaded or

mechanical-rotation-based unit cells can perform 2D beam steering as these unit cells can provide independent and tunable reflection phases. The main drawback of the PIN diode enabling reconfigurable reflectarray antenna is the significant loss introduced by PIN diodes. The operating frequency of the PIN diode also limits the applications of such reconfigurable reflectarray antennas. As a result, a low-cost, high-efficiency, 2D beam-steerable reflectarray antenna is preferred.

Shared-aperture antennas are emerging antennas, which are usually implemented by properly integrating multiple antennas into the same architecture so that all sub-antennas can radiate to free space through a shared aperture. Due to the highlights of compact size, dual-band, high space reuse efficiencies, etc., shared-aperture antennas have been widely studied and discussed [84]-[92]. A shared-aperture antenna is a good antenna candidate, covering the operating bands of 4G and the evolved 5G or upcoming 6G. The current challenges for shared-aperture antennas lie in the realizations of dual-polarization, high gain, low loss, high aperture reuse efficiency, and more than two operating bands with a simple and efficient configuration. The operating polarization of a shared-aperture antenna is mainly dependent on the specific forms of the sub-antennas. For example, a slot antenna (array) usually works in a single polarization, a shared-aperture antenna involved with slot antennas is therefore usually single-polarized accordingly. The previously reported high gain and dual-polarized shared-aperture antennas were achieved with the aid of complicated and lossy feeding networks. A dual-polarized shared-aperture antenna was proposed in [88], where the authors designed two feeding networks to excite the two antenna arrays. This method can also be applied to enable a triple-band dual-polarized shared-aperture antenna as reported in [91]. But more complicated and lossy feeding networks are essential to excite the three different antenna arrays accordingly. A dual-polarized shared-aperture antenna at sub-6GHz was implemented with a stacked configuration [92], making full use of the space. However, the stacked configuration is not suitable for millimeter-wave shared-aperture antenna designs due to its structural limitation. As a result, it is urgently demanded to develop a new architecture to facilitate the design of dual-polarized, high gain, high aperture reuse efficiency, and triple-band shared-aperture antennas.

1.2 Aims of the thesis

As the reflectarray/transmitarray antennas have noticeable highlights such as high gain, simple structure, low loss, etc., this Ph.D. thesis mainly involves

the studies and implementations of broadband, polarization-reconfigurable, beam-steerable, and shared-aperture millimeter-wave antennas based on the forms of reflectarray/transmitarray antennas. The techniques described in this thesis can provide solutions or alternative solutions to design the antennas with similar performance.

Broadband transmitarray antenna

The bandwidth of a transmitarray/reflectarray antenna is narrow as the phase-shifting surface is usually composed of resonance-based unit cells. A 360-degree transmission phase coverage of the resonance-based unit cell is obtained by resizing its dimensions. It is found that the transmission phase coverage and the bandwidth of the passband with high transmission efficiency are highly dependent. A large transmission phase coverage always results in a narrow bandwidth. As a result, a smaller transmission phase coverage (e.g., a 1-bit or 2-bit phase quantization) could be a solution to broaden the bandwidth of a transmitarray antenna. It has been demonstrated that a 1-bit phase quantization reduces the gain of the corresponding transmitarray antenna, while a 2-bit phase quantization can achieve comparable results with the continuous transmission phase. The previously reported approach to obtain a 2-bit transmission phase still relied on resizing a single unit cell, which would shrink the overlapping passband bandwidth to suppress the bandwidth of the corresponding transmitarray antenna. Therefore, the goal is to propose a new methodology to develop a wideband transmitarray antenna, where the desired 2-bit transmission phase will no longer depend on resizing the dimensions of a single unit cell. Two kinds of unit cells with different configurations were proposed. By properly optimizing the configurations of the unit cells, they can provide the desired 2-bit transmission phase in a wide band with high transmission efficiencies, thereby achieving a wideband transmitarray antenna.

Wideband polarization-reconfigurable reflectarray antenna

A unit cell made of dielectric material is an excellent candidate to implement a wideband transmitarray/reflectarray antenna since it can offer wideband phase shifts due to its non-resonant properties. On the other hand, by properly optimizing the dimensions of a dielectric-based unit cell, a 90-degree phase difference can be obtained when transverse electric (TE) and transverse magnetic (TM) incidence waves impinge the unit cell. The 90-degree phase difference is a critical factor to form a circular polarization. The abilities of the dielectric-based unit cells implementing a circularly-polarized reflectarray antenna are twofold: the first one is to offer desired phase shift, the other one is to provide a 90-degree phase difference for TE and TM incidence waves.

Such a unit cell can be achieved by simply cascading two kinds of unit cells responsible for phase shift and 90-degree phase difference, respectively. However, it suffers from a high profile. In this thesis, therefore, the author proposes a dielectric-based unit cell that emerging the two abilities as mentioned above into a single unit cell rather than cascading two kinds of unit cells, thereby reducing the profile of the unit cell. A 2-bit phase quantization is adopted to simplify and facilitate the implementation of the proposed reflectarray antenna. The dimensions of the unit cell are needed to optimize to find out the desired four kinds of unit cells. The phase-shifting surfaces can be implemented with the proposed unit cells. By simply rotating the phase-shifting surface $+45^\circ/-45^\circ$, the proposed reflectarray antenna can convert its polarization from linear to circular mode.

2D beam-steerable reflectarray antenna

Most of the 2D beam-steerable reflectarray antennas are enabled by loading PIN diodes on unit cells. By electrically switching ON/OFF states of PIN diodes, each unit cell can offer a 1-bit reflection phase independently. The loss of the PIN diodes is a noticeable issue since it lowers the total efficiency of the beam-steerable reflectarray antenna, especially at the millimeter-wave and even higher frequency bands. Moreover, the complexity of such a beam-steerable reflectarray antenna is also high as the feeding network should be appropriately designed and arranged to excite the PIN diodes without introducing extra resonances to impact the performance of the beam-steerable reflectarray antenna. To this end, the author focuses on developing an alternative solution to design a low-cost and high-efficiency beam-steerable reflectarray antenna in this thesis. A full-metal unit cell is proposed to provide a 1-bit reflection phase by simply rotating it along its axial, avoiding using any PIN diodes.

Shared-aperture antenna

A shared-aperture antenna is a good solution to include antennas operating at microwave and millimeter-wave bands in the same architecture for a smooth transition from 4G to the evolved 5G or upcoming 6G millimeter-wave band. Currently, shared-aperture antennas face the challenges of realizing dual-polarization, high gain, high aperture reuse efficiency, and multiple operating bands simply and efficiently. This thesis aims to develop a new architecture to design shared-aperture antennas with attractive features such as dual-polarization, high gain, high space reuse efficiency by finding out some proper antennas with similar configurations and integrating them efficiently.

2. General knowledge and discussions

In this chapter, the general knowledge and some discussions are presented to understand the theory and methods in the papers of Part II.

2.1 Transmitarray/Reflectarray antenna

Transmitarray/reflectarray antennas are kinds of aperture antennas, typically consisting of a feed source and a phase-shifting surface. The schematic diagrams of transmitarray and reflectarray antennas are presented in Fig. 2.1. The main difference between the transmitarray and reflectarray antennas lies in whether the electromagnetic waves can propagate through or be reflected by the phase-shifting surface. For a transmitarray antenna, the electromagnetic waves can propagate through it freely, while the electromagnetic waves are fully reflected by it for a reflectarray antenna.

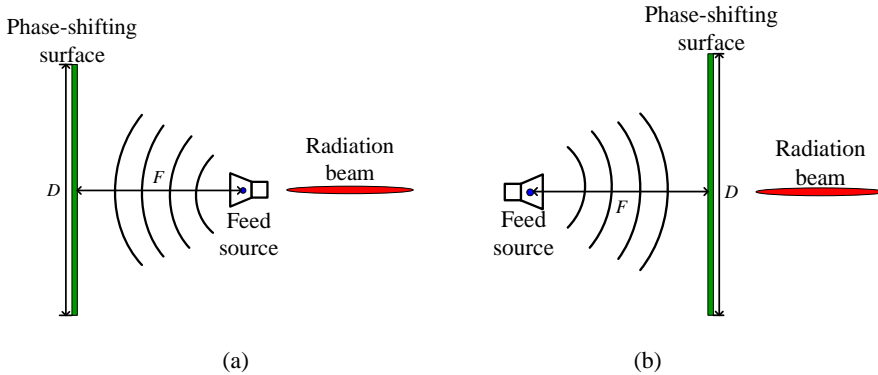


Fig.2.1. The schematic diagrams of transmitarray and reflectarray antennas. (a). A reflectarray antenna. (b). A transmitarray antenna.

As is known, the plane wave is a kind of wave that can naturally produce a focused beam (high gain) due to its in-phase characteristic. The operating principle of a transmitarray/reflectarray antenna achieving high gain is to convert the spherical waves emanating from the feed source to a plane wave through the phase-shifting surface. The phase-shifting surface is composed of lots of unit cells, each of which is responsible for a specific phase shift, where the specific value of the phase shift that each unit cell should offer is dependent on the behaviors of the incoming electromagnetic waves on the plane of the phase-shifting surface. Fig. 2.2 illustrates a simple model to

determine the specific phase shift of each unit cell in a transmitarray or reflectarray antenna design. The emitting electromagnetic waves from the feed source propagate in free space, and the phase when the electromagnetic waves arrive at a point $(x_i, y_i, 0)$ is calculated as [27]:

$$\varphi = -\frac{2\pi}{\lambda} \cdot \left(\sqrt{(x_f - x_i)^2 + (y_f - y_i)^2 + (z_f)^2} \right) \quad (2.1)$$

where (x_f, y_f, z_f) is the specific location of the phase center of the feed source, λ is the wavelength at the frequency of interest. Referring to Eq. (2.1), the phase of each unit cell on the phase-shifting surface can be obtained, typically ranging from $-\pi$ to π . According to the calculated phase distributions, the unit cells can be properly designed and allocated to compensate for the desired phase shifts to convert the spherical wave to a plane wave, thereby resulting in a focused beam at the boresight direction.

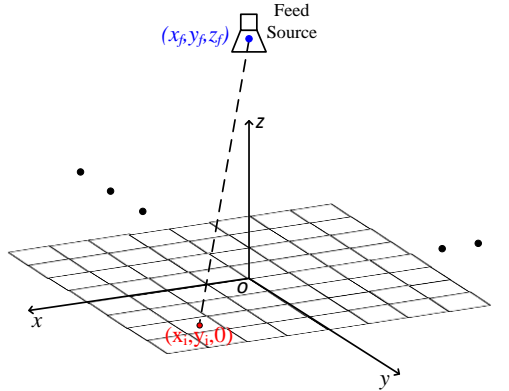


Fig. 2.2. A simple model to determine the phase shift of each unit cell.

Aperture efficiency: One of the metrics to assess the performance of a transmitarray/reflectarray antenna is aperture efficiency, which is defined as [27]:

$$\eta = \frac{G\lambda^2}{4\pi S} \quad (2.2)$$

where G is the gain of the transmitarray/reflectarray antenna, λ is the wavelength at the frequency of interest, S is the physical area of the phase-shifting surface. Equation (2.2) implies that the aperture efficiency of a transmitarray/reflectarray antenna is in high association with the gain, frequency, and size of the phase-shifting surface. Once the operating

frequency and the size of the phase-shifting surface are determined, the aperture efficiency is directly related to the gain of the corresponding transmitarray or reflectarray antenna.

The ratio of focal length to diameter (F/D): The radiation pattern of the feed source and the relative position of the feed source with respect to the phase-shifting surface affect the gain of a transmitarray/reflectarray antenna. The effects can be characterized by spillover efficiency and illumination efficiency when the feed source illuminates the phase-shifting surface. The spillover efficiency is defined as the ratio of the power received by the phase-shifting surface and the total power radiated by the feed source. Or, in other words, how much power the phase-shifting surface can receive from the feed source. The illumination efficiency means how uniform the electric fields on the phase-shifting surface are. Referring to the definitions of spillover and illumination efficiencies, it can be deduced that spillover efficiency is negatively correlated with illumination efficiency. In other words, a high spillover efficiency always leads to a low illumination efficiency and vice versa. A parameter of the ratio of focal-length-to-diameter (F/D) is, therefore, proposed to link the spillover and illumination efficiencies of a transmitarray or reflectarray antenna. The distance between the phase center of the feed source and the phase-shifting surface is F . If the phase-shifting surface is circular, D is the diameter, or D is the side length if the phase-shifting surface is square. As a result, when both the feed source and the size of the phase-shifting surface are determined, the ratio of F/D needs to be optimized to achieve a better aperture efficiency.

1- and 3-dB gain bandwidth: Except for the impedance bandwidth that is a general metric for all kinds of antennas, the 1- and 3-dB gain bandwidth are widely used in transmitarray/reflectarray antennas to assess their performance. The 1- or 3-dB gain bandwidth is defined as the frequency band within which the gain drops 1 or 3dB with respect to its peak gain. A wide 1-dB gain bandwidth indicates that a transmitarray/reflectarray antenna can provide relatively stable gains in a wide frequency band, which is attractive in wireless communications.

Blockage effects of feed source: For a centrally-fed reflectarray antenna, as illustrated in Fig. 2.3(a), the feed source is in line with the main beam of the reflectarray antenna when the main beam is at broadside direction, the blockage of the feed source will degrade the gain of the reflectarray antenna. Such a blockage does not exist in a transmitarray antenna since the beams of the feed source and the transmitarray antenna are in the same direction. The

blockage effects can be alleviated by adopting the offset feeding technique, where the feed source obliquely illuminates the phase-shifting surface as shown in Fig. 2.3(b) so that the feed source will not block the main beam of the reflectarray antenna. However, the offset feeding technique usually results in a lower aperture efficiency accordingly.

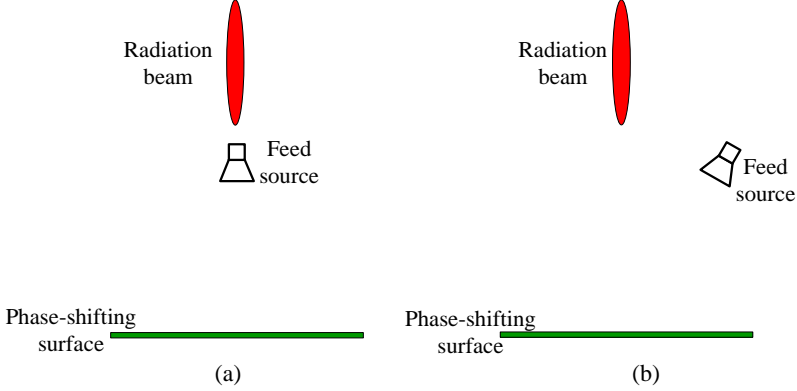


Fig. 2.3. The schematic diagrams of two reflectarray antennas. (a). Centrally-fed reflectarray antenna. (b). Offset-fed reflectarray antenna.

2.2 Phase quantization

In this section, phase quantization to enhance the bandwidth of a transmitarray antenna is studied from full-wave simulations rather than the theoretical calculations as the full-wave simulations would consider all losses introduced by the unit cells that are hard to be modeled in the theoretical calculations.

As verified in [46], a four-layered and double-ring (square) structure usually serves as the unit cell to implement a transmitarray antenna. The unit cell can provide a bandpass response so that the electromagnetic waves can propagate through it freely. A full phase-cycle (2π) is usually obtained by tuning certain dimensions of the unit cell. A phenomenon is observed here that the transmission phase shift is closely associated with the frequencies of the passband. Specifically speaking, when the unit cell dimension is tuned to offer different phase shifts, the passband will shift toward a high- or low-frequency band as well. The high dependence between the phase shift and transmission efficiency limits the bandwidth of the corresponding transmitarray antenna.

To intuitively demonstrate this phenomenon, the author designs a unit cell as shown in Fig. 2.4 to check its frequency response. The supporting substrates are 0.305mm-thick Rogers 4003C that is characterized by a dielectric constant

of 3.55, a loss tangent of 0.0027. The dimensions of the unit cell are appropriately determined to make it operate at the 28 GHz band, where the periodicity of the unit cell is typically around half-wavelength.

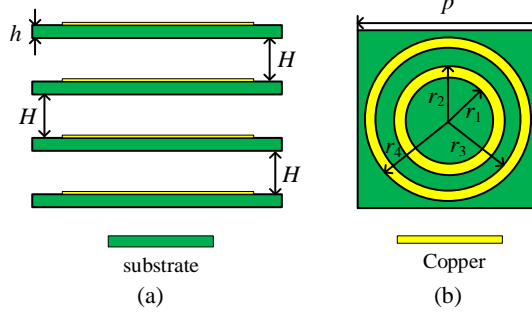


Fig. 2.4. The configurations of the unit cell. (a). Side view. (b). Front view. ($p = 5.0$ mm, $h = 0.305$ mm, $H = 2.5$ mm, $r_4 = 2.25$ mm, $r_3 = 1.75$ mm, $r_2 - r_1 = 0.5$ mm)

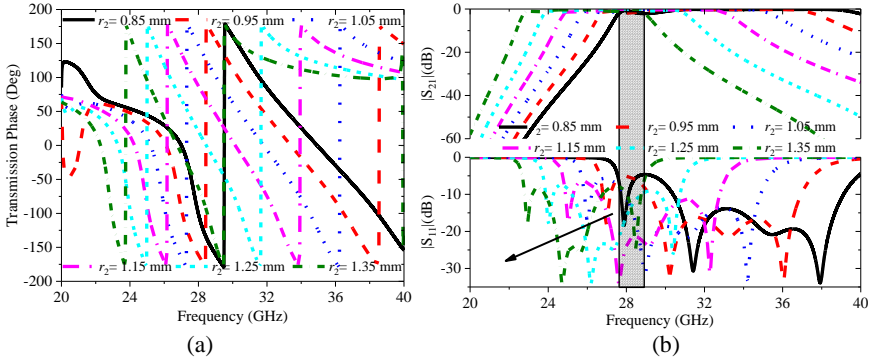


Fig. 2.5. S-parameter of the unit cell with different values of r_2 . (a) Transmission phase. (b). Amplitudes of reflection and transmission coefficients.

The unit cell can offer a full phase-cycle by simply adjusting the radius of r_2 with the inner ring and the other parameters fixed [46]. The S-parameters (amplitudes and phases) of the unit cell are simulated with different values of r_2 . As seen in Fig. 2.5 (a), the transmission phase of the unit cell is varied with the different values of r_2 . However, the passband with high transmission efficiency ($|S_{21}|$ is close to 0dB) is also shifting toward lower frequencies with the increment of r_2 at the same time, leading to a narrow bandwidth with overlapping frequencies, as shown in Fig. 2.5(b). It is found that the high correlation between the transmission phase and amplitude is an inherent characteristic for the resonance-based unit cell. As seen in Fig. 2. 5(a), when the value of r_2 varies from 0.85 to 1.35mm, the unit cell can offer a 360-degree transmission phase coverage from 26 to 32GHz. By contrast, the passband

with high transmission efficiency (e.g., $|S_{21}|$ is less than 1.0dB) is only from 27.8 to 28.8 GHz. At 26GHz, for example, the attenuation reaches 20 and 30 dB when r_2 is equal to 0.95 and 0.85mm, respectively. Such high attenuations will degrade the gain of the corresponding transmitarray antenna at 26 GHz.

As seen in Fig. 2.5, the bandwidth with overlapping frequencies is inversely proportional to the transmission phase coverage. Specifically speaking, when the unit cell only offers a 180-degree transmission phase coverage, the bandwidth with overlapping frequencies is wider than the unit cell capable of a 360-degree transmission phase coverage. This conclusion inspires one to consider using a small transmission phase coverage (e.g., 1-bit, 2-bit, 3-bit, etc.) to implement a transmitarray antenna rather than a full phase-cycle coverage to avoid unit cells with high attenuations, thereby enhancing the bandwidth of a transmitarray antenna. No doubt that using a small transmission phase coverage will introduce a large phase error that is usually called quantization loss, resulting in a reduced gain of the corresponding transmitarray antenna. The reduced gain, however, is promising to be compensated back by the small attenuations of the unit cells.

To verify the effectiveness of the smaller transmission phase coverage on broadening the bandwidth of a transmitarray antenna, the continuous transmission phase is discrete into four different coverages:

- Scenario 1: a full phase-cycle ($-\pi$ to π) for reference;
- Scenario 2: 2 transmission phase states (0 and π);
- Scenario 3: 3 transmission phase states ($-\pi$, $-\pi/3$, and $\pi/3$);
- Scenario 4: 4 transmission phase states ($-\pi$, $-\pi/2$, 0, and $\pi/2$);
- Scenario 5: 6 transmission phase states ($-\pi$, $-2\pi/3$, $-\pi/3$, 0, $\pi/3$, and $2\pi/3$)

When scenarios 2, 3, 4, and 5 are applied, some approximations should be made since the phase shift that each unit needs to compensate for is ranging from $-\pi$ to $+\pi$ continuously according to equation (2.1). To this end, equations (2.3) – (2.6) are adopted to discretize the continuous transmission phase. Fig. 2.6 plots the realized gains of transmitarray antennas implemented by the unit cells with the above-mentioned five different transmission phase coverages, where the dimensions of the phase-shifting surfaces, the feed sources, and the F/D are all kept the same for fair and reasonable comparisons.

$$\varphi_{actual} = \begin{cases} 0, & -\pi/2 < \varphi_{desired} < \pi/2 \\ \pi, & \text{Otherwise} \end{cases} \quad (2.3)$$

$$\varphi_{actual} = \begin{cases} -\pi, & -\pi < \varphi_{desired} < -\pi/3 \\ -\pi/3, & -\pi/3 < \varphi_{desired} < \pi/3 \\ \pi/3, & \pi/3 < \varphi_{desired} < \pi \end{cases} \quad (2.4)$$

$$\varphi_{actual} = \begin{cases} -\pi, & -\pi < \varphi_{desired} < -\pi/2 \\ -\pi/2, & -\pi/2 < \varphi_{desired} < 0 \\ 0, & 0 < \varphi_{desired} < \pi/2 \\ \pi/2, & \pi/2 < \varphi_{desired} < \pi \end{cases} \quad (2.5)$$

$$\varphi_{actual} = \begin{cases} -\pi, & -\pi < \varphi_{desired} < -2\pi/3 \\ -2\pi/3, & -2\pi/3 < \varphi_{desired} < -\pi/3 \\ -\pi/3, & -\pi/3 < \varphi_{desired} < 0 \\ 0, & 0 < \varphi_{desired} < \pi/3 \\ \pi/3, & \pi/3 < \varphi_{desired} < 2\pi/3 \\ 2\pi/3, & 2\pi/3 < \varphi_{desired} < \pi \end{cases} \quad (2.6)$$

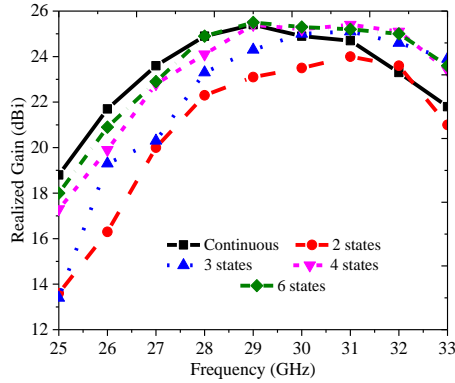


Fig. 2.6. Realized gains of a TA antenna implemented by the elements with five different transmission phase scenarios.

It is found, in Fig. 2.6, that the realized gains of the transmitarray antennas with 4 and 6 transmission phase states are very close to each other and are

higher than the transmitarray antenna with a 360-degree transmission phase coverage at some frequencies. The realized gain is reduced for the transmitarray antenna with 2 transmission phase states. The 3dB gain bandwidth of the transmitarray antenna with 4 or 6 transmission phase states is wider than the transmitarray antenna implemented with a continuously 360-degree transmission phase. From Fig. 6, it is also found that 4 transmission phase states are sufficient to replace the continuous transmission phase to achieve comparable realized gains and wide 3dB gain bandwidth. The author also checked the realized gains of the transmitarray antennas with those five different transmission phase coverages mentioned above under another two different F/D , where the same conclusion can still be obtained.

Some wideband transmitarray antennas have been reported based on 1-, 2-, or 3-bit phase quantization [52]-[56]. The Introduction part states that the polarization-rotating structure is a perfect candidate to perform 1-bit phase quantization. Even though the polarization-rotating structure is also a kind of resonant structure, the bandwidth of a polarization-rotating structure with high transmission efficiency can be very wide if its dimensions are properly chosen [93], [94]. The main drawback of 1-bit phase quantization lies in the degraded gain of the corresponding transmitarray antenna. The polarization-rotating structure can also be extended to enable a 2-bit phase quantization by resizing its dimensions [52], [53]. Once the action of resizing the unit cell happens, the passband will be shifted accordingly, referring to Fig. 2(c) in [53]. The shifted passband still results in a narrow bandwidth with overlapping frequencies, leading to decreasing the bandwidth of the corresponding transmitarray antenna.

In summary, it is found that, for PCB-based unit cells, the passband will, generally, shift toward lower or higher frequencies accordingly when the actions of resizing the unit cell to tune the transmission phase happen. The high dependence between the transmission phase and band is a critical factor to suppress the bandwidth of the corresponding transmitarray antenna. As a result, resizing the unit cell to obtain various transmission phases should be avoided in the design of a wideband transmitarray antenna.

2.3 Reconfigurable antenna

According to the reconfigurable targets of an antenna, it can be broadly subdivided into frequency reconfigurable that tunes the operating bands of an antenna, polarization reconfigurable that controls the operating polarization of

an antenna, and radiation pattern reconfigurable that steers the radiation beam of an antenna. In this section, the author mainly introduces the principles to generate reconfigurable polarization and radiation patterns.

2.3.1 Polarization reconfigurable

According to the orientation of the electric field of electromagnetic waves during the propagation in free space, in other words, the shape of the trace that the electric field changes with time, the polarization of an electromagnetic wave is divided into linearly-polarized, circularly-polarized, and elliptically-polarized waves. Any polarization can be represented by two orthogonal linear polarizations with their respective amplitudes and phases, as illustrated in Fig. 2.7. The phase difference of the two components is defined $\delta = \varphi_x - \varphi_y$ for the convenient description in the following.

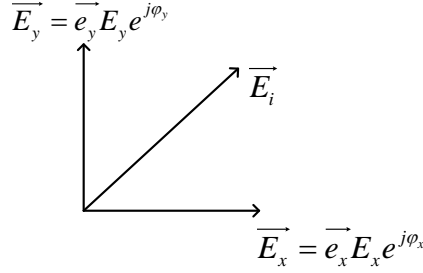


Fig. 2.7. A simple diagram to explain the principle to generate linearly-, circularly-, and elliptically-polarized waves.

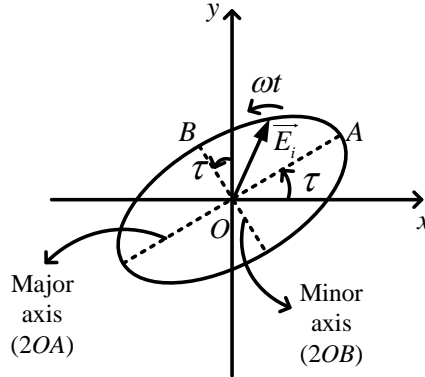


Fig. 2.8. The trace of the elliptically-polarized wave with time

Linear polarization: The electric field is confined to a single plane along the direction of propagation, $|E_x|$ can be different from $|E_y|$, but $\delta = 0$ or $n\pi$;

Circular polarization: The electric field can be decomposed into two linear components. The two components are perpendicular to each other, equal in amplitude, and have a 90-degree phase difference, e.g., $|E_x| = |E_y|$, and $\delta = \pm \pi/2$. As a result, the resultant electric field rotates in a circle around the direction of propagation. According to $\delta = -\pi/2$ or $+\pi/2$, the circularly-polarized wave is further divided into left- and right-hand circularly polarized waves;

Elliptical polarization: The amplitudes of two components are not equal, and the phase difference is not $\pi/2$ either, $|E_x|$ is not equal to $|E_y|$, and δ is not equal to $\pm \pi/2$;

As the elliptical polarization is the most general description of the electromagnetic wave, where the linearly- and circularly-polarized waves can be viewed as the two special cases of the elliptically-polarized wave, the elliptically-polarized wave is therefore studied. The trace of the electric field of an elliptically-polarized wave is typically ellipse, as illustrated in Fig. 2.8. The axial ratio (AR) is defined as follows [95]:

$$AR = \frac{\text{major axis}}{\text{minor axis}} = \frac{OA}{OB} \quad (2.7)$$

where:

$$OA = \sqrt{\frac{1}{2} \left(E_x^2 + E_y^2 + \sqrt{E_x^4 + E_y^4 + 2E_x^2 E_y^2 \cos(2\delta)} \right)} \quad (2.8)$$

$$OB = \sqrt{\frac{1}{2} \left(E_x^2 + E_y^2 - \sqrt{E_x^4 + E_y^4 + 2E_x^2 E_y^2 \cos(2\delta)} \right)} \quad (2.9)$$

The tilted angle of the ellipse is defined and calculated as [95]:

$$\tau = \frac{1}{2} \arctan \left(\frac{2E_x E_y}{E_x^2 - E_y^2} \cos \delta \right) \pm \frac{\pi}{2} \quad (2.10)$$

According to equations (2.7), (2.8), and (2.9), the axial ratio is closely related to the amplitudes and phase difference of the two components, ranging from one to infinity. Specifically speaking, the AR is infinity for a purely linearly-polarized wave that $\delta = 0$. By contrast, the AR is 1 for a purely circularly-polarized wave that $|E_x| = |E_y|$ and $\delta = \pm \pi/2$. In the antenna community, an antenna can be viewed as circularly polarized when its AR is

below 3dB. The 3dB AR bandwidth means the frequency band that the AR of an antenna is below 3dB.

Based on the above studies, the critical factor to achieve a circularly-polarized wave is producing two orthogonal components with equal amplitudes and a 90-degree phase difference. As a reflectarray antenna is usually illuminated by a linearly-polarized feed source, a unit cell able to convert a linear-polarized wave to a circularly-polarized one is essential to realize a polarization-reconfigurable reflectarray antenna. As stated in the Introduction part, the dielectric material is a good candidate for a wideband phase-shifting medium by simply tuning its height. Fig. 2.9 gives a general dielectric-based unit cell. As seen in Fig. 2.9 (b), the unit cell demonstrates the same frequency responses for x - and y -polarized incidence waves as the unit cell is highly symmetrical (polarization-insensitive). Such a unit cell, therefore, can only work for linear polarization applications.

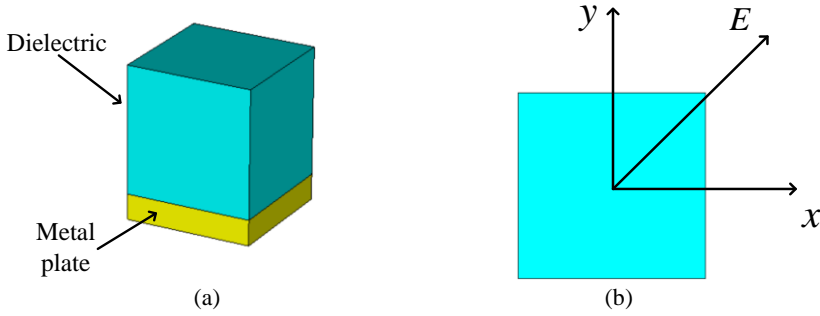


Fig. 2.9. The dielectric-based unit cell for linear polarization. (a). Perspective view. (b). Front view.

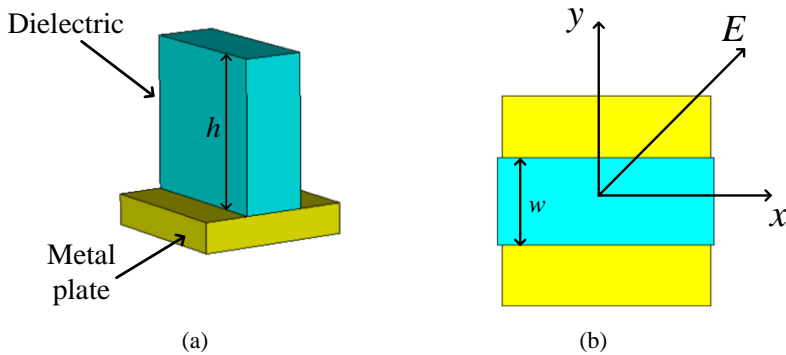


Fig. 2.10. The dielectric-based unit cell for circular polarization. (a). Perspective view. (b). Front view.

Fig. 2.10 presents a dielectric-based unit cell that is possible for generating a circular polarization. The length and width of the unit cell are not the same. The frequency responses (reflection phase is mainly concerned) are distinct for x - and y -polarized incidence waves as the boundary conditions of the unit cell are different. By properly optimizing the width and height of the unit cell, it can provide a 90-degree phase difference for x - and y -polarized incidence waves, which is capable of polarization reconfigurable. Specifically speaking, when the incidence wave is a x - or y -polarized wave, the unit cell can only reflect the corresponding x - or y -polarized wave. By contrast, for a ± 45 -degree linearly-polarized incidence wave, the reflected waves can be decomposed into x -component and y -component. According to the phase of the x -component lags or advances 90 degrees of the y -component, the resulting reflected wave is a right (left)-hand circularly-polarized one accordingly.

There are lots of different combinations of width and height of the dielectric-based unit cell to achieve a 90-degree phase difference for x - and y -polarized incidence waves. Among them, it is possible to find out four combinations of width and height so that the four dielectric-based unit cells can offer a 2-bit reflection phase simultaneously. The phase-shifting surface of a reflectarray antenna can be implemented with the four dielectric-based unit cells. When a linearly-polarized feed source illuminates the phase-shifting surface, the reflectarray antenna can convert its operating mode from a linear-polarization to a right (left)-hand circular polarization or a left (right)-hand circular polarization by simply rotating the phase-shifting surface ± 45 or ∓ 45 degrees.

Unlike PCB-based unit cells, where some metallic patterns are printed on a dielectric substrate, the dielectric-based unit cell can be massively produced with currently popular 3D printing technology fast and economically.

2.3.2 Radiation pattern reconfigurable

The reconfigurable radiation pattern is an attractive feature for an antenna since it allows the antenna to accurately track individual users to offer better and reliable connections. The fundamental principle to steer the beam of a reflectarray antenna is to manipulate the reflection phase of each unit cell. The specific direction of the main beam is related to the phase differences among the adjacent unit cells of a reflectarray antenna. The relationship between the beam direction and phase difference is derived by studying a simple eight-element linear antenna array.

Fig. 2.11 illustrates a simple diagram of an eight-element linear antenna array, where all antenna elements are identical and the distance between the adjacent antenna elements is equal. For a linear antenna array, its radiation beam can only be steered in a one-dimensional plane. When the beam of the linear antenna array is specified at θ off-broadside direction as depicted in Fig. 2.11, the phase difference of the adjacent antenna elements needs to satisfy the following equation:

$$\Delta\varphi = \frac{2\pi}{\lambda} \cdot d \cdot \sin \theta \quad (2.11)$$

where λ is the wavelength at the frequency of interest, d is the distance between the adjacent antenna elements. For example, when $\theta = 30^\circ$ and $d = \lambda/2$, the phase difference of the adjacent antenna elements is $\pi/2$.

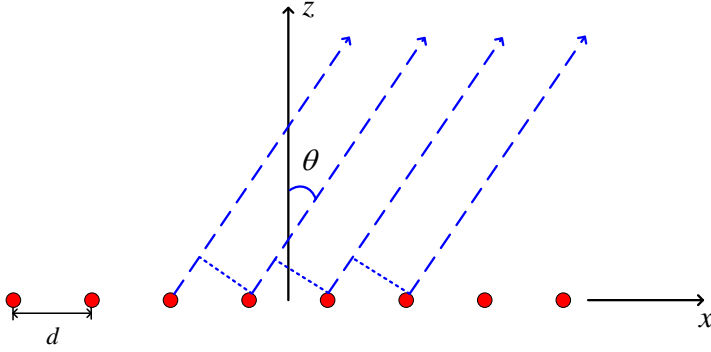


Fig. 2.11. A simple diagram of an eight-element linear antenna array.

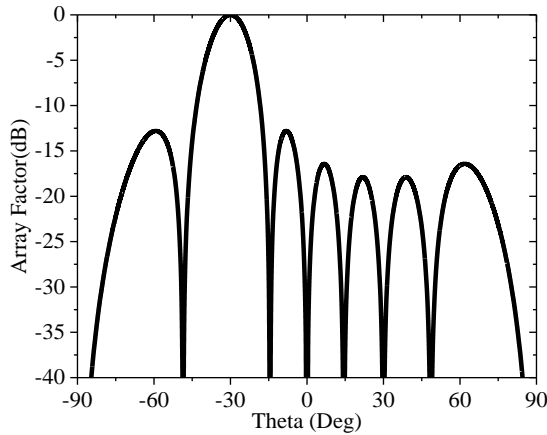


Fig. 2.12. The array factor of the eight-element linear antenna array.

Knowing the phase difference of the adjacent antenna elements, the array factor of the eight-element linear antenna array is simply formulated as:

$$\begin{aligned}
 AF = 1 + e^{j(\frac{2\pi}{\lambda} \cdot d \cdot \sin \theta + \frac{\pi}{2})} + e^{j(\frac{2\pi}{\lambda} \cdot 2 \cdot d \cdot \sin \theta + 2 \cdot \frac{\pi}{2})} + e^{j(\frac{2\pi}{\lambda} \cdot 3 \cdot d \cdot \sin \theta + 3 \cdot \frac{\pi}{2})} \\
 + e^{j(\frac{2\pi}{\lambda} \cdot 4 \cdot d \cdot \sin \theta + 4 \cdot \frac{\pi}{2})} + e^{j(\frac{2\pi}{\lambda} \cdot 5 \cdot d \cdot \sin \theta + 5 \cdot \frac{\pi}{2})} + e^{j(\frac{2\pi}{\lambda} \cdot 6 \cdot d \cdot \sin \theta + 6 \cdot \frac{\pi}{2})} \\
 + e^{j(\frac{2\pi}{\lambda} \cdot 7 \cdot d \cdot \sin \theta + 7 \cdot \frac{\pi}{2})}
 \end{aligned} \tag{2.12}$$

According to equation (2.12), the array factor of the eight-element linear antenna array can be plotted as illustrated in Fig. 2.12, where the main beam directing to 30 degrees is observed. It should be mentioned here, the calculation of the array factor in equation (2.12) is based on assumptions that the mutual couplings among antenna elements are not considered and each antenna element has the same radiation pattern. The resulting radiation pattern of the eight-element antenna array can be obtained by multiplying the array factor by the antenna element's radiation pattern. If the phase difference of the adjacent antenna elements is $-\pi/2$, the main beam of the eight-element linear antenna array will direct to -30-degree off-broadside direction.

The reflectarray antenna can perform 2D beam steering as it is a kind of planar array. The phase difference of the adjacent array elements for 2D beam steering is a little complicated than that for 1D beam steering, but it can still be derived from the 1D beam steering case. For the main beam of a reflectarray antenna specified at (θ, φ) , the progressive phase phases of the adjacent array elements in x - and y -direction are formulated as [95]:

$$\Delta \varphi_x = \frac{2\pi}{\lambda} \cdot d_x \cdot \sin \theta \cos \varphi \tag{2.13}$$

$$\Delta \varphi_y = \frac{2\pi}{\lambda} \cdot d_y \cdot \sin \theta \sin \varphi \tag{2.14}$$

where λ is the wavelength at the frequency of interest, d_x and d_y are the distances between the adjacent array elements in x - and y -direction, respectively. Once the specified direction of the main beam of the reflectarray antenna is known, the phase differences of any two adjacent array elements can be determined according to equations (2.13) and (2.14).

For a passive reflectarray antenna, each unit cell can only provide a single reflection phase shift so that such a reflectarray antenna, generally, cannot

steer its beam. However, if the unit cells are capable of providing tunable reflection phases that ideally cover a 360-degree coverage, the corresponding reflectarray antenna can perform 2D beam steering. However, it is difficult to offer a 360-degree reflection phase coverage with an efficient approach. Fortunately, a 1-bit or 2-bit reflection phase can be readily achieved by loading PIN diodes on the unit cells. By electrically switching the ON/OFF states of the PIN diodes, the unit cell can offer 0° and 180° reflection phases at the frequency of interest. A 2-bit reflection phase usually needs more PIN diodes, increasing instabilities, complexity, and energy consumption. As a result, a 1-bit reflection phase is widely adopted in designing beam-steerable reconfigurable reflectarray antennas even though the 1-bit reflection phase can reduce the gain of the corresponding reflectarray antenna.

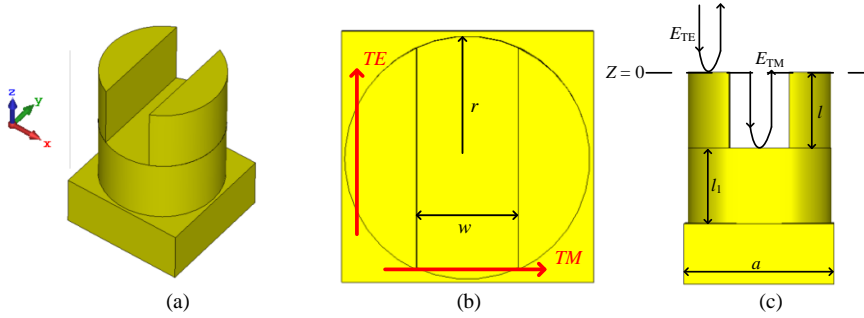


Fig. 2.13. The full-metal unit cell in Paper C to provide a 1-bit reflection phase. (a). Perspective view. (b). Front view. (c). Side view.

Tab. I. The comparison of mechanical and electrical control techniques

	Cost	Loss	Efficiency	Complexity	Speed
Electrical control	High	High	Low	High	High
Mechanical control	Low	Low	High	Low	Low

Except for the PIN diode-loaded unit cell, paper C proposes a full-metal unit cell as shown in Fig. 2.13, which can offer a 1-bit reflection phase. By properly optimizing the dimensions of the cuboid notch (l and w), the full-metal unit cell can provide a 1-bit reflection phase for TE and TM incidence waves. Therefore, the full-metal unit cell only needs to rotate 90 degrees to change its reflection phase from 0 to 180° . The rotation of the full-metal unit cell can be mechanically controlled by connecting it with a mini-step motor [83].

The pros and cons of the electrical and mechanical control techniques are compared in Table I. The highlights of the mechanical control method lie in its low cost, low loss, high efficiency, and low complexity, but it suffers from relatively low speed compared to the electrical control method.

2.4 Fabry-Perot antenna

The term “Fabry-Perot” named after two physicists Charles Fabry and Alfred Perot who developed the Fabry-Perot interferometer is originally from optics. The Fabry-Perot interferometer is made from two parallel reflecting surfaces, where optical waves can pass through the optical cavity only when they are in resonance with it [96]. Later, the concept of Fabry-Perot resonance has been extended from optical band to microwave and millimeter-wave bands to design high gain antennas that are usually named Fabry-Perot antenna.

The general schematic diagram of a Fabry-Perot antenna is shown in Fig. 2. 14. It consists of two surfaces: one is the partially reflective surface, and the other is a fully reflective surface. The feed source is typically in the plane of the fully reflective surface but can also be placed between the partially and fully reflective surfaces. The feed source is usually a low-gain antenna such as a dipole antenna, planar patch antenna, etc.

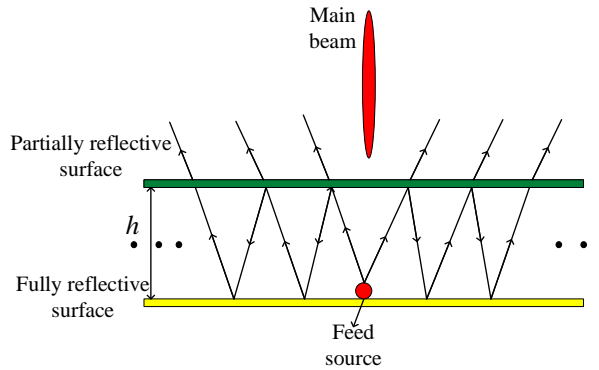


Fig. 2. 14. The general schematic diagram of a Fabry-Perot antenna.

The partially reflective surface is a kind of surface that allows the electromagnetic waves to propagate through it partially. In other words, when incoming electromagnetic waves impinge the partially reflective surface, part of electromagnetic waves can propagate through it, while the remaining electromagnetic waves are reflected by it. The ratio of transmitted and reflected electromagnetic waves is closely associated with the properties of

the partially reflective surface. The fully reflective surface, by its name, is a kind of surface that can reflect electromagnetic waves fully.

As illustrated in Fig. 2.14, the electromagnetic waves emitted from the feed source will hit the partially reflective surface first, where part of the electromagnetic waves can pass through it and then propagate in free space. The remaining electromagnetic waves will be reflected by the fully reflective surface and impinge the partially reflective surface again. The electromagnetic waves usually experience multiple reflections and transmissions between the partially and fully reflective surfaces for a Fabry-Perot antenna. By properly controlling the separation between the partially and fully reflective surfaces, the electric fields on the aperture of the partially reflective surface can be in phase, thereby resulting in a high gain. The separation h is typically calculated as [97]:

$$-\frac{2\pi f}{c} \cdot 2 \cdot h - \varphi_{PRS} - \varphi_{FRS} = 2n\pi, n = 0, 1, 2, \dots \quad (2.15)$$

where φ_{PRS} and φ_{FRS} are reflection phases of the partially and fully reflective surfaces, respectively, c is the light speed in free space, and f is the frequency of interest.

The directivity of a Fabry-Perot antenna is closely related to the ratio of the transmitted and reflected electromagnetic waves of the partially reflective surface. The directivity of a Fabry-Perot can be evaluated using the following equation [97]:

$$D = 10 \log \frac{1+R}{1-R} \quad (2.16)$$

where R is the reflection amplitude of the partially reflective surface. A small R will result in a large directivity referring to equation (2.16). This can be explained from the aperture antenna viewpoint, where it is widely acknowledged that a large-size aperture typically contributes to a high gain. A small R indicates that the electromagnetic waves will experience more reflections and transmissions between the partially and fully reflective surfaces, thereby requiring large-size partially and fully reflective surfaces.

A pure dielectric substrate is a kind of natural material to implement a partially reflective surface as the dielectric constant of a dielectric substrate is higher than that of air. When electromagnetic waves impinge the dielectric substrate, part of them will propagate through it and the remaining electromagnetic waves will be reflected. The ratio of the transmitted and

reflected electromagnetic waves can be controlled through the dielectric constant of the dielectric substrate. The transmission and reflection coefficients of a dielectric substrate with different constants from 5 to 15GHz are plotted in Fig. 2.15. A general conclusion can be observed from Fig. 2.15 that the reflection amplitude is small and the transmission amplitude is big when the dielectric constant of the dielectric substrate is small. The partially reflective surface can also be implemented by periodic PCB-based unit cells. By tuning the dimensions of the unit cell (its periodicity and metallic pattern), the ratio of the transmitted and reflected electromagnetic waves can be controlled accordingly. For a pure dielectric-substrate-based partially reflective surface, it needs to find a proper dielectric constant to ensure the desired ratio of transmitted and reflected electromagnetic waves, which, sometimes, is expensive. By contrast, the PCB-based partially reflective surface can be implemented with cheap and available substrates. The dimensions of the metallic patterns can control the reflection and transmission amplitudes. Another issue for the partially reflective surface implemented by the pure dielectric substrate is the remarkable surface wave effects compared to the one constructed with the PCB-based unit cells. The surface wave effects will distort the radiation patterns of the Fabry-Perot antenna.

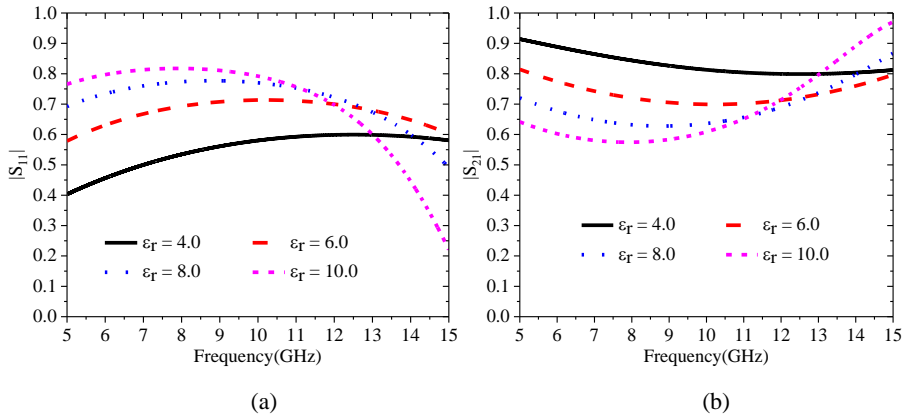


Fig. 2.15. The reflection and transmission coefficients of dielectric substrate with different dielectric constants. (a). Reflection amplitude. (b). Transmission amplitude.

2.5 Folded transmitarray antenna

As stated in the Introduction part, a drawback of a transmitarray antenna is its high profile. Folding technology is an effective technique to reduce the profile of a transmitarray antenna. Fig. 2.16 presents the illustration of a fold

transmitarray antenna. It consists of a metal plate that served as a reflective surface, a feed source, and a phase-shifting surface. The feed source and the phase-shifting surface can be in the same aperture for a compact configuration.

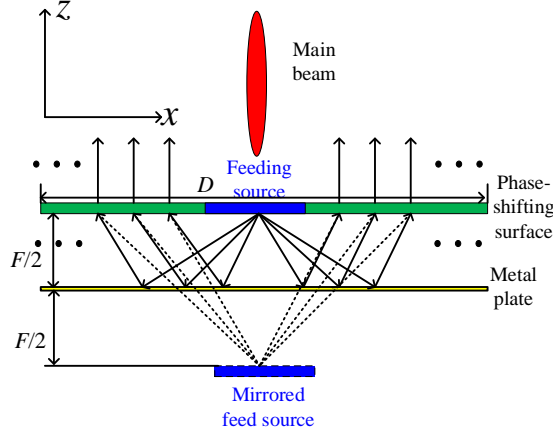


Fig. 2. 16. The schematic diagrams of the folded transmitarray antenna.

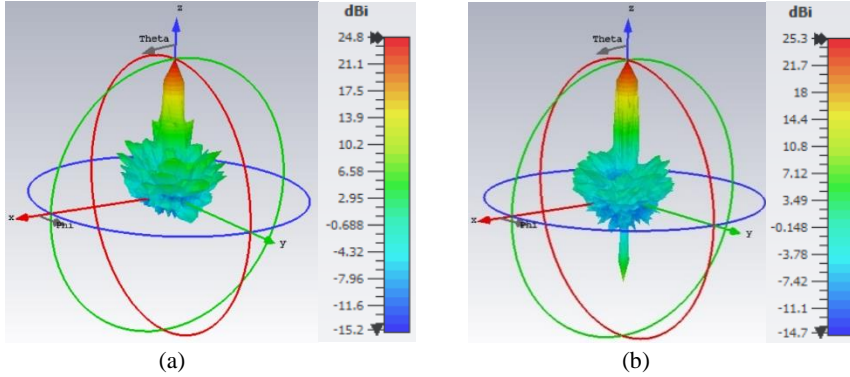


Fig. 2. 17. The simulated directivity of the transmitarray antennas at 28GHz. (a). Fold transmitarray antenna. (b). Conventional transmitarray antenna

In this configuration, the metal plate reflects the electromagnetic waves emitted from the feed source, the reflected electromagnetic waves then propagate through the phase-shifting surface to achieve a pencil beam in the specified direction. Due to the presence of the metal plate, it can be viewed that there is a mirrored feed source located at the other side of the metal plate as the radiation beam of the feed source is $-z$ -direction. The distance between the mirrored feed source and the metal plate is the same as the real feed source with respect to the metal plate. Therefore, the folded transmitarray antenna is,

generally, equivalent to a conventional transmitarray antenna with the mirrored feed source impinging the phase-shifting surfaces. As a result, the profile of a folded transmitarray antenna is reduced to half to a conventional transmitarray antenna.

In order to demonstrate the similar radiation performance of the folded and conventional transmitarray antennas, the author simulates their radiation patterns at 28GHz. The sizes of the phase-shifting surfaces, the feed sources, and the unit cells to implement the phase-shifting surfaces are all kept the same for a fair and reasonable comparison. Fig. 2.17 compares the directivity of the folded and conventional transmitarray antennas at 28GHz, where the directivity of the folded transmitarray antenna very close to that of the conventional transmitarray antenna can be observed. The slight difference in directivity might be attributed to the finite size of the metal plate. According to the simulated directivities of the folded and conventional transmitarray antennas, it is concluded that the fold transmitarray antenna can achieve comparable directivity with a reduced profile compared to the conventional transmitarray antenna.

From Figs. 2.14 and 2.16, the configuration of the Fabry-Perot antenna is very similar to that of the folded transmitarray antenna. As a result, it is possible to combine these two antennas together to form a shared-aperture antenna, where the Fabry-Perot antenna and folded transmitarray antenna are responsible low- and high-frequency bands, respectively. For the shared-aperture antenna, the phase-shifting surfaces are required to offer phase shifting and partially reflective performance for high- and low-frequency bands, respectively. As the Fabry-Perot and folded transmitarray antennas radiate into free space through the same aperture (the phase-shifting surface), the aperture reuse efficiency of the shared-aperture, therefore, is perfect, which is attractive compared to the existing shared-aperture antennas. Another highlight of such a shared-aperture antenna lies in its high gain and easy realization of dual/circular-polarization without using any complicated feeding networks.

2.6 Dual-band reflectarray antenna

A dual-band reflectarray antenna, by its name, indicating that the reflectarray antenna can operate at two different frequency bands, can be implemented with the following two approaches: a). designing a unit cell capable of offering phase shifts at two frequency bands simultaneously [98]-[102]; b). with the

aid of the frequency selective surfaces, designing two kinds of unit cells, each of which is responsible for the phase shift at different frequency bands, [103]-[105]. For the former one, the operating frequency bands are not allowed to be far away from each other. Otherwise, it will be difficult to balance the phase shifts at the two bands simultaneously, and the mutual couplings between the two bands will also be an issue. By contrast, for the latter one, the ratio of the two operating frequencies can be flexibly controlled by properly designing the frequency-selective-surface-backed unit cell. Since the unit cells to provide phase shifts for different frequency bands are not in the same layer, the mutual couplings between the two bands will be weak. Here, the author mainly describes the dual-band reflectarray antenna based on the latter approach.

Fig. 2.18 gives a general diagram of a dual-band reflectarray antenna enabled by frequency selective surfaces. It consists of two feed sources, a frequency selective surface, two phase-shifting surfaces. In this configuration, the frequency selective surfaces are required to be fully reflective and transparent at the high- and low-frequency bands, respectively. The full reflectance can equivalently act as a metal ground at the high-frequency band, where the phase-shifting unit cell for the high frequency can be co-designed with the frequency selective surfaces. As a result, the electromagnetic waves emitted from the feed source for high frequency are directly reflected and focused when they illuminate the frequency selective surfaces. By contrast, the electromagnetic waves emitted from the feed source for low frequency can propagate through the frequency selective surfaces and impinge the phase-shifting surface for low frequency to achieve a focused beam at the low-frequency band.

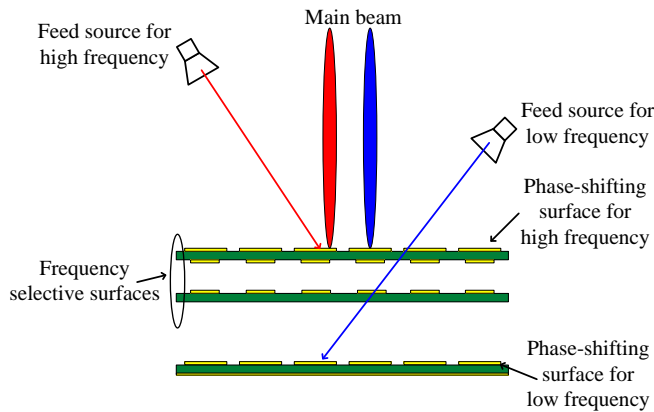


Fig. 2. 18. A general diagram dual-band reflectarray antenna based on frequency selective surfaces.

By tuning the dimensions of the frequency selective surfaces, the dual-band reflectarray antenna can control its operating bands flexibly. The unit cells to implement the phase-shifting surfaces can be designed separately. In addition, the phase shifts of the unit cells for low and high frequencies can also be tuned independently, which facilitates the design of the dual-band reflectarray antenna.

It is also found that the configuration of the dual-band reflectarray antenna shown in Fig. 2.18 is very similar to that of the Fabry-Perot antenna shown in Fig. 2. 14. The phase-shifting surfaces and frequency selective surfaces shown in Fig. 2.18 can be properly designed to offer the required conditions to enable a Fabry-Perot antenna. A feed source can be integrated into the phase-shifting surface for low frequency to form a Fabry-Perot antenna by fully making use of the dual-band reflectarray antenna to implement a triple-band shared-aperture antenna. The dual-band reflectarray antenna is responsible for high- and middle-frequency bands and the Fabry-Perot antenna operates at the low-frequency band. Combining a Fabry-Perot antenna and a dual-band reflectarray antenna offers a solution to design a triple-band shared-aperture antenna with some features of high gain, high aperture reuse efficiency, simple configuration, etc.

3. Contributions

This section presents the main contributions of this thesis together with brief summaries of the motivation, content, and findings of the papers included in Part II.

This Ph.D. project involves the following objectives:

1. Broadband transmitarray antenna with flat gains for 5G millimeter-wave applications.
2. A wideband reflectarray antenna with mechanically reconfigurable polarization for polarization-reconfigurable applications based on 3D printing technology.
3. A low-cost, high-efficiency, and full-metal reflectarray antenna with mechanically 2D beam-steerable capabilities for 5G millimeter-wave applications.
4. A dual-polarized and high-gain shared-aperture antenna with high aperture reuse efficiency, offering an alternative solution to design a dual-polarization, high gain, and high aperture reuse efficiency.

5. A triple-band shared-aperture with high figures of merit, providing a solution to design a triple-band shared-aperture antenna.

The main contributions of this thesis can be listed below, where the corresponding paper(s) are indicated in parentheses.

1. A broadband transmitarray antenna is realized by using two kinds of unit cells with different configurations, where the unit cells can offer the desired 2-bit transmission phase without resizing their dimensions. (Paper A)
2. A wideband polarization-reconfigurable reflectarray antenna is obtained by involving a dielectric-based unit cell. The unit cells are capable of converting a linearly-polarized wave to a circularly-polarized one and phase-shifting ability simultaneously. (Paper B)
3. A low-cost, high-efficiency reflectarray antenna with mechanically 2D beam-steerable capabilities is realized with full-metal unit cells. The unit cell can offer a 1-bit reflection phase by simply rotating its direction for a linearly-polarized wave. (Paper C)
4. Dual-band and triple-band shared-aperture antennas are achieved with high figures of merit such as dual-polarization, high gain, high aperture efficiency, etc., by integrating a Fabry-Perot antenna into transmitarray or reflectarray antennas (Papers D and E)

3.1 Paper A

A Broadband and FSS-Based Transmitarray Antenna for 5G Millimeter-Wave Applications

Peng Mei, Gert Frølund Pedersen, and Shuai Zhang

Published at the *IEEE Antennas and Wireless Propagation Letters*, vol. 20, no. 1, pp. 103-107, Jan. 2021.

Motivation

The propagation loss in free space is significant at the millimeter-wave band. High gain 5G millimeter-wave antennas are desired to compensate for the propagation loss to maintain link budgets for wireless communication systems. Transmitarray antenna is a good candidate to realize high gain due to its simple configuration, low loss, etc. However, the bandwidth of a transmitarray antenna is typically narrow due to the resonant characteristics of the unit cells. Phase quantization has been turned out to be an effective method to broaden the bandwidth of a transmitarray antenna, where a 2-bit transmission phase is

usually adopted to maintain the gain. This contribution aims to propose a distinct method to design two kinds of unit cells to offer the desired 2-bit transmission phase to achieve a broadband transmitarray antenna.

Paper content

It is found that resizing the unit cell to offer the desired transmission phases will shift the passband to a low- or high-frequency band, which suppresses the bandwidth of the corresponding transmitarray antenna. This paper proposes two kinds of unit cells with different configurations. Both of the unit cells are based on polarization-rotating structures due to their wideband properties. By optimizing the patterns of the two kinds of unit cells, they can contribute to a wide passband and a 2-bit transmission phase simultaneously. Using these two kinds of unit cells, a broadband transmitarray antenna can be achieved. The final design has been fabricated and measured to verify the performance.

Main results

The periodicity and thickness of the unit cell are 0.25λ and 0.2λ , respectively. Both of the two kinds of unit cells have low attenuations (less than 1.0dB) from 24 to 38 GHz within which a 2-bit transmission phase is also satisfied. Great agreement between the simulated and measured results has been obtained. The measured 1- and 3-dB gain bandwidths of the proposed transmitarray antenna are 28.0 - 37.5GHz (29%) and 25.1 - 39.1GHz (43.7%), respectively. The measured peak aperture efficiency of the broadband transmitarray antenna is 44.7% at 30GHz with a realized gain of 26.1dBi.

3.2 Paper B

A Wideband 3D Printed Reflectarray Antenna with Mechanically Reconfigurable Polarization

Peng Mei, Shuai Zhang, and Gert Frølund Pedersen

Published at the *IEEE Antennas and Wireless Propagation Letters*, vol. 19, no. 10, pp. 1798-1802, Oct. 2020.

Motivation

The operating polarizations are distinct in different wireless communication systems, for example, it is linear polarization for base stations, while it is circular polarization for satellite communications. An antenna capable of multiple polarizations is preferred as it can communicate with different communication systems. The polarization-reconfigurable antenna is such an

antenna that can offer linear and circular polarizations. The narrow bandwidth of a polarization-reconfigurable antenna enabled by PIN diodes is an issue that potentially limits its application requiring the coverage of wide frequency bands. The dielectric-based reflectarray antenna is a good candidate to achieve wideband as the dielectric-based unit cell works at its non-resonant state. The thesis, therefore, aim at designing a wideband polarization-reconfigurable reflectarray antenna by using dielectric-based unit cells.

Paper content

This paper design four kinds of dielectric-based unit cells. Their dimensions are appropriately optimized to offer a 2-bit reflection phase and 90-degree phase difference for TE and TM incidence waves simultaneously. The mechanisms of the four kinds of dielectric-based unit cells to achieve the 90-degree phase difference are quantitatively formulated. When a 45-degree linearly-polarized incidence wave illuminates the unit cells, the resulting reflected waves can be either right- or left-hand circular polarization. The phase-shifting surface is implemented by these four kinds of dielectric-based unit cells. When a linearly-polarized feed source impinges the phase-shifting surface, the reflectarray antenna can convert its polarization from linear polarization to right(left)-hand circular polarization by simply rotating the phase-shifting surface 45(-45) degrees. Due to the unit cells are made of dielectric material, the phase-shifting surface can be massively produced with 3D printing technology. The final design has been fabricated and measured to verify the performance.

Main results

Four kinds of dielectric-based unit cells have been designed. Each dielectric-based unit cell can offer a 90-degree phase difference for TE and TM incidence waves from 24 to 38 GHz. Moreover, the four kinds of dielectric-based unit cells can offer a 2-bit reflection phase from 24 to 38GHz as well. The measured results are highly consistent with the simulated results. The measured results demonstrate that the polarization-reconfigurable reflectarray antenna can reach a 3dB axial ratio of 43.2% and 37.5% for right-hand and left-hand circular polarization mode, respectively. Furthermore, a 3dB gain bandwidth of 37.5%, 34.4%, and 37.5% is experimentally obtained for right-hand circular polarization, left-hand circular hand polarization, and linear polarization mode.

3.3 Paper C

A Low-Cost, High-Efficiency, and Full-Metal Reflectarray Antenna with Mechanically 2D Beam-Steerable Capabilities for 5G Applications.

Peng Mei, Shuai Zhang, and Gert Frølund Pedersen

Published at the *IEEE Transactions on Antennas and Propagation*, vol. 68, no. 10, pp. 6997-7006, Oct. 2020.

Motivation

In some application scenarios, beam-steerable antennas are necessary to ensure reliable connections with mobile users, especially at the millimeter-wave band. Phased arrays are classical and effective antennas to achieve 2D beam steering, but suffer from high cost, high loss, and bulky volume. The reconfigurable reflectarray antenna is another sort of antenna capable of steerable beams, where each unit cell is loaded with PIN diodes. By switching ON/OFF states of the PIN diodes, the unit cell can offer a 1-bit reflection phase that is critical to enable a beam-steerable reflectarray antenna. However, this solution is high-cost, high-loss, and high-complexity as a DC-biasing network is needed to excite PIN diodes. The layout of the DC-biasing network, sometimes, deteriorates the performance of the entire reconfigurable reflectarray antenna. This thesis is, therefore, dedicated to developing a full-metal unit cell to offer a 1-bit reflection phase by mechanically rotating its direction instead of using any RF components, which makes the beam-steerable reflectarray antenna low-cost and high-efficiency.

Paper content

This paper involves a full-metal unit cell that can offer a 1-bit reflection phase without using any active RF components but by simply rotating it along its axial. A notch etched in a cylinder forms the full-metal unit cell. By tuning the dimension of the notch (width and height), the full-metal unit cell can offer 0° and 180° reflection phase in a wide band for TE and TM incidence waves, respectively. By controlling the rotation of each full-metal unit cell, the corresponding reflectarray antenna can achieve 2D steerable beams. The final design has been fabricated and measured to verify the performance.

Main results

It is found that the width of the notch is related to the bandwidth of the 1-bit reflection phase, where a wider width contributes to a wider bandwidth. The

measured results agree well with the simulations. The measured 1.5dB gain bandwidth is around 20% from 24.7 to 30 GHz. A peak realized gain of 18.9dBi at 26GHz is experimentally obtained. The total efficiency of the proposed reflectarray antenna is higher than 90% from 24 to 30 GHz. The maximum gain drop is 2.0dB when the beam is scanned to 60 degrees off-broadside direction in H-plane. Due to its full-metal structure, the proposed reflectarray antenna is highlighted with low cost, high-efficiency, and high-power handling features, which make it suitable for 5G millimeter-wave communication to offer a fixed or steerable beam.

3.4 Paper D

A Dual-Polarized and High Gain X-/Ka-Band Shared-Aperture Antenna with High Aperture Reuse Efficiency

Peng Mei, Shuai Zhang, and Gert Frølund Pedersen

Published at the *IEEE Transactions on Antennas and Propagation*, vol. 69, no. 3, pp. 1334-1344, Mar. 2020.

Motivation

Shared-aperture antennas are emerging antennas with some features of compact size and high space utilization efficiency. They offer good solutions to integrate the current microwave and millimeter-wave antennas into the same architecture to cope with the wireless communications at the low- and high-frequency bands. The performance of a shared-aperture antenna is usually determined by the specific types of sub-antennas. The current shared-aperture antennas generally suffer from single-polarization, low gain, and low aperture reuse efficiency. Some dual-polarization and high-gain shared-aperture antennas are usually achieved at the expense of complicated feeding networks. The author, therefore, aims at designing a dual-polarized and high gain shared-aperture antenna with high aperture reuse efficiency by finding out two proper types of antennas to combine them efficiently. The proposed methodology provides an alternative solution to design a dual-polarized and high-gain shared-aperture antenna with a simple architecture.

Paper content

This paper introduces a novel methodology that makes full use of a Fabry-Perot antenna and a folded transmitarray antenna to comprise a dual-polarized and high-gain shared-aperture antenna simply and efficiently. The folded

transmitarray works at the high-frequency band and the Fabry-Perot antenna operates at the low-frequency band. The shared aperture needs to offer the phase-shifting ability for the folded transmitarray antenna and partial reflectance/transmission for the Fabry-Perot antenna. A four-layered double-ring structure is proposed as the unit cell to implement the shared aperture. Its frequency responses at the low- and high-frequency bands are completely studied. It is found that the unit cell can provide highly independent frequency responses at the low- and high-frequency bands, which facilitates the design of the proposed shared-aperture antenna. A prototype has been fabricated and measured to validate its performance.

Main results

The unit cell to implement the shared aperture demonstrates a passband from 24 to 34GHz and a partial reflectance/transmission from 8 to 12GHz or 13 to 14GHz. By tuning the radius of the inner ring, the unit cell can offer a full transmission phase-cycle at the high-frequency band while the frequency responses at the low-frequency band are maintained. The partial reflectance/transmission performance can be controlled by varying the radius of the outer ring while the frequency responses at the high-frequency band are still maintained. A dual-polarized and high-gain shared-aperture antenna is implemented by the unit cells. The measured and simulated results are highly consistent. The measured results demonstrate the proposed shared-aperture antenna has -10dB bandwidths of 9.75 to 10.2GHz and 26.7 to 29.4GHz. The realized gain of 14.8dBi at 10GHz and 24.4GHz at 28GHz are both experimentally obtained in two polarizations.

3.5 Paper E

Design of a Triple-Band Shared-Aperture Antenna with High Figures of Merit

Peng Mei, Xian Qi Lin, Gert Frølund Pedersen, and Shuai Zhang

Published at the *IEEE Transactions on Antennas and Propagation*, 2021. DOI: 10.1109/TAP.2021.3090837

Motivation

The number of the operating bands is another consideration for a shared-aperture antenna. In general, a shared-aperture antenna covering as many operating bands as possible is preferred for multiservice applications and to make full of the space. Most of the reported work on shared-aperture antennas

was mainly focused on dual-band since it is challenging to find out three or even more antennas with proper configurations and combine them efficiently. A straightforward method to implement a triple-band shared-aperture antenna is to employ three feeding networks to excite three antenna arrays that are arranged in the same aperture, which is complicated and high loss, especially for large-scale antenna arrays. The goal, here, is to find a simple and efficient architecture to integrate three antennas together to make them radiate through the same aperture, offering a solution to design a triple-band shared-aperture antenna with high figures of merit.

Paper content

This paper integrates a Fabry-Perot antenna into a dual-band reflectarray antenna to constitute a triple-band shared-aperture antenna operating at X/K/Ka-band with features of high aperture reuse efficiency, the possibility for dual- and circular polarizations. The unit cell to form the phase-shifting surface at the high-frequency band is configured with a cross-shaped dipole backed by frequency selective surfaces, which is transparent at the middle-frequency band and partial reflectance/transmission at the low-frequency band. The unit cell to implement the phase-shifting surface is also composed of a cross-shaped dipole, which can offer full reflectance at the low-frequency band. It is also found that the frequency responses of the unit cells are highly independent at different frequency bands (low-, middle-, and high-frequency bands), which simplifies the design of the proposed shared-aperture antenna. The feed source for the Fabry-Perot antenna can be integrated into the phase-shifting surface for middle frequency. A matching layer is utilized to improve the impedance match of the Fabry-Perot antenna. A prototype has been fabricated and measured to verify its performance.

Main results

The frequency selective surfaces can offer a partial reflection/transmission from 5 to 11GHz, a bandpass response from 24 to 38GHz, and a full reflection from 35 to 40GHz. A cross-shaped dipole is printed on the frequency selective surface to serve as a phase-shifting element for the high frequency. A full reflection phase-cycle at 38GHz can be obtained by varying the length of the cross-shaped dipole, where the frequency responses at the middle- and low-frequency bands can still be maintained. The unit cell to form the phase-shifting surface for middle frequency can achieve a 270-degree reflection phase coverage at 26GHz by tuning the length of the cross-shaped dipole, where the full reflection property at the low-frequency band can still be

maintained. The air separation between the phase-shifting surfaces for high frequency and middle frequency is determined according to the operating frequency of the Fabry-Perot antenna. Good agreement between simulations and measurements has been observed. The measured results present the 3dB gain bandwidth of 11.2% from 8.4 to 9.4GHz, 10% from 24 to 26.6GHz, and 13.3% from 35 to 40GHz. The peak gains of 16.8dBi at 9.0GHz, 23.8dBi at 26GHz, and 26.7dBi at 38GHz are experimentally obtained.

4. Conclusion

5G millimeter-wave bands have their unique advantages over microwave bands in wireless communications such as wide absolute bandwidth and high data rate but suffer from significant propagation loss in free space. One of the effective solutions to compensate for the loss is utilizing high-gain antennas to receive and transmit electromagnetic waves. Some other strict requirements are imposed on millimeter-wave antennas with increasingly complex electromagnetic environments and application scenarios. On one hand, antennas with polarization-reconfigurable performance are preferred to communicate with different wireless communication systems such as base stations and satellites as the base station and satellite usually work at linearly- and circularly-polarized modes, respectively. On the other hand, antennas are also required to offer steerable beams to communicate with mobile users efficiently. This thesis mainly focuses on developing broadband, polarization-reconfigurable, and beam-steerable antennas with high gains at the millimeter-wave bands based on the forms of transmitarray/reflectarray antennas.

The bandwidth of a transmitarray/reflectarray antenna is usually narrow, mainly attributed to the resonant characteristics of the unit cells. A broadband transmitarray antenna is implemented by using a 2-bit phase quantization. Two kinds of unit cells with different configurations are properly designed to offer a 2-bit transmission phase in a wide band. The 2-bit transmission phase is obtained without resizing the unit cells. A wideband 3D printed reflectarray antenna with mechanically reconfigurable polarization has been described for polarization diversity applications. The author designs four dielectric-based unit cells with different dimensions to implement the phase-shifting surface. The four dielectric-based unit cells can offer simultaneous 90-degree phase differences for TE and TM incidence waves and a 2-bit reflection phase. Considering the high cost and loss of PIN diodes enabling beam-steerable reflectarray antennas, the author develops a full-metal unit cell to offer a 1-bit

reflection phase by mechanically rotating its direction to perform a 2D beam-steerable reflectarray antenna with features of low cost, high efficiency, and high-power handling.

To take care of microwave and millimeter-wave antennas in the same architecture, shared-aperture antennas are good candidates that can combine multiple antennas operating at different frequency bands efficiently, where these antennas radiate to free space through the same aperture to make full use of the space. The current challenges of a shared-aperture antenna lie in its difficulties in the realizations of dual-polarization and triple-band simply and efficiently. The author, for the first time, integrates a Fabry-Perot antenna into a fold transmitarray antenna to form a shared-aperture antenna. As it is easy for a Fabry-Perot antenna and fold transmitarray antenna to achieve dual-polarization and both the Fabry-Perot and fold transmitarray antennas radiate to free space through the physically same aperture, the resulting shared-aperture antenna features dual-polarization, high gain, and perfect aperture reuse efficiency. What's more, a triple-band shared-aperture is also developed by integrating a Fabry-Perot antenna into a dual-band reflectarray antenna. The proposed two shared-aperture antennas offer solutions to implement a dual-polarized, high-gain, high aperture reuse efficiency, and triple-band shared aperture antenna.

The wideband transmitarray antenna presented in this thesis can only work in a single polarization mainly attributed to the single polarization properties of the polarization-rotating element itself. The dual-polarized polarization-rotating element can be investigated in the future to facilitate the dual-polarized wideband transmitarray antenna. On the other hand, reconfigurable intelligent surfaces (RISs) are emerging technologies, serving as promising solutions for improving the connectivity of the evolved 5G and upcoming 6G wireless communications, which have been widely discussed in the communication community. The reflectarray antenna is generally regarded as the basic configuration of a RIS. With some basic knowledge presented in this thesis, the future work will be focused on designing RISs for near-field and far-field wireless communications.

References

- [1] W. L. Barrow, and L. J. Chu, "Theory of the electromagnetic horn," *Proceedings of the I. R. E.*, pp. 51-64, Jan 1939.
- [2] A. Mavaddat, S. Hossein Mohseni Armaki, and A. Reza Erfanian, "Millimeter-wave energy harvesting using 4×4 microstrip patch antenna array," *IEEE Antennas and Wireless Propagation Letters*, vol. 14, pp. 515-518, 2015.
- [3] N. Ghassemi, and K. Wu, "High-efficient patch antenna array for E-band gigabyte point-to-point wireless services," *IEEE Antennas and Wireless Propagation Letters*, vol. 11, pp. 1261-1264, 2012.
- [4] A. Borji, D. Nusuioc, and S. Safavi-Naeini, "Efficient, low-cost integrated waveguide-fed planar antenna array for Ku-band applications," *IEEE Antennas and Wireless Propagation Letters*, vol. 8, pp. 336-339, 2008.
- [5] M. Shahabadi, D. Busuioc, A. Borji, and S. Safavi-Naeini, "Low-cost, high-efficiency quasi-planar array of waveguide-fed circularly polarized microstrip antennas," *IEEE Transactions on Antennas and Propagation*, vol. 53, no. 6, pp. 2036-2043, June 2005.
- [6] M. H. Awida, and A. E.Fathy, "Substrate-integrated waveguide Ku-band cavity-backed 2×2 microstrip patch array antenna," *IEEE Antennas and Wireless Propagation Letters*, vol. 8, pp. 1054-1056, 2009.
- [7] J. Wei, Z. Chen, X. Qing, J. Shi, and J. Xu, "Compact substrate integrated waveguide slot antenna array with low back lobe," *IEEE Antennas and Wireless Propagation Letters*, vol. 12, pp. 999-1002, 2013.
- [8] L. Yan, W. Hong, G. Hua, J. Chen, K. Wu, and T. Cui, "Simulation and experiment on SIW slot array antennas," *IEEE Microwave and Wireless Component Letters*, vol. 14, no. 9, pp. 446-448, Sept 2004.
- [9] J. Xu, Z. Chen, and X. Qing, "CPW center-fed single-layer SIW slot antenna array for automotive radars," *IEEE Transactions on Antennas and Propagation*, vol. 62, no. 9, pp. 4528-4536, Sept 2014.

- [10] Y. Cheng, Y. Guo, and Z. Liu, "W-band large-scale high-gain planar integrated antenna array," *IEEE Transactions on Antennas and Propagation*, vol. 62, no. 6, pp. 3370-3373, June 2010.
- [11] Y. Cheng, H. Xu, D. Ma, J. Wu, L. Wang, and Y. Fan, "Millimeter-wave shaped-beam substrate integrated conformal array antenna," *IEEE Transactions on Antennas and Propagation*, vol. 61, no. 9, pp. 4558-4566, Sept 2010.
- [12] X. Chen, K. Wu, L. Han, and F. He, "Low-cost high gain planar antenna array for 60-GHz band applications," *IEEE Transactions on Antennas and Propagation*, vol. 58, no. 6, pp. 2126-2129, June 2010.
- [13] S. Gao, L. Li, M. Leong, and T. Yao, "A broad-band dual-polarized microstrip patch antenna with aperture coupling," *IEEE Transactions on Antennas and Propagation*, vol. 51, no. 4, pp. 898-900, April 2003.
- [14] K. Lau, and K. Luk, "A novel wide-band circularly polarized patch antenna based on L-probe and aperture-coupling techniques," *IEEE Transactions on Antennas and Propagation*, vol. 53, no. 1, pp. 577-580, Jan 2005.
- [15] M. Bilgic, and K. Yegin, "Wideband offset slot-coupled patch antenna array for X/Ku-band multimode radars," *IEEE Antennas and Wireless Propagation Letters*, vol. 13, pp. 157-160, 2014.
- [16] D. Zarifi, A. Farahbakhsh, and A. Zaman, "A gap waveguide-fed wideband patch antenna array for 60-GHz applications," *IEEE Transactions on Antennas and Propagation*, vol. 65, no. 9, pp. 4875-4879, Sept 2017.
- [17] A. Vosoogh, and P. S. Kildal, "Corporate-fed planar 60-GHz slot array made of three unconnected metal layers using AMC pin surface for the gap waveguide," *IEEE Antennas and Wireless Propagation Letters*, vol. 15, pp. 1935-1938, 2016.
- [18] A. Zaman, and P. S. Kildal, "Wide-band slot antenna arrays with single-layer corporate-feed network in ridge gap waveguide technology," *IEEE Transactions on Antennas and Propagation*, vol. 62, no. 6, pp. 2992-3001, June 2014.
- [19] L. Ge, and K. Luk, "A wideband magneto-electric dipole antenna," *IEEE Transactions on Antennas and Propagation*, vol. 60, no. 11, pp. 4987-4991, Nov 2012.

- [20] M. Li, and K. Luk, "Wideband magneto-electric dipole antenna for 60-GHz millimeter-wave communications," *IEEE Transactions on Antennas and Propagation*, vol. 63, no. 7, pp. 3276-3279, July 2015.
- [21] Y. Li, C. Wang, and Y. Guo, "A Ka-band wideband dual-polarized magnetoelectric dipole antenna array on LTCC," *IEEE Transactions on Antennas and Propagation*, vol. 68, no. 6, pp. 4985-4990, June 2020.
- [22] Y. Li, L. Ge, J. Wang, B. Ai, M. Chen, Z. Zhang, and Z. Li, "A Ka-band 3-D-Printed wideband stepped waveguide-fed magnetoelectric dipole antenna array," *IEEE Transactions on Antennas and Propagation*, vol. 68, no. 4, pp. 2724-2735, April 2020.
- [23] Z. Hao, Q. Yuan, B. Li, and G. Luo, "Wideband W-band substrate-integrated waveguide magnetoelectric (ME) dipole array antenna," *IEEE Transactions on Antennas and Propagation*, vol. 66, no. 6, pp. 3195-3200, June 2018.
- [24] F. Hasselmann, and L. Felsen, "Asymptotic analysis of parabolic reflector antennas," *IEEE Transactions on Antennas and Propagation*, vol. AP-30, no. 4, pp. 677-685, July 1982.
- [25] C. Cutler, "Parabolic-antenna design for microwave," *Proceedings of the IRE*, pp. 1284-1293, Nov. 1947.
- [26] L. J. Anderson, and L. H. Groth, "Reflector surface deviations in large parabolic antennas," *IEEE Transactions on Antennas and Propagation*, pp. 148-152, March 1963.
- [27] J. Huang, and J. A. Encinar, *Reflectarray Antennas*. Hoboken, NJ, USA: Wiley, 2008.
- [28] D. M. Pozar, "Bandwidth of reflectarrays," *Electronics Letters*, vol. 39, no. 21, Oct. 2003.
- [29] D. M. Pozar, and T. A. Metzler, "Analysis of a reflectarray antenna using microstrip patches of variable size," *Electronics Letters*, vol. 29, no. 8, pp. 657-658, April 1993.
- [30] J. Huang, and R. J. Pogorzelski, "A Ka-band microstrip reflectarray with elements having variable rotation angles," *IEEE Transactions on Antennas and Propagation*, vol. 46, no. 5, pp. 650-656, May 1998.

- [31] D. M. Pozar, S. D. Targonski, and R. Pokuls, "A shaped-beam microstrip patch reflectarray," *IEEE Transactions on Antennas and Propagation*, vol. 47, no. 7, pp. 1167-1173, July 1999.
- [32] J. A. Encinar, "Design of two-layer printed reflectarrays using patches of variable size," *IEEE Transactions on Antennas and Propagation*, vol. 49, no. 10, pp. 1403-1410, Oct 2001.
- [33] J. A. Encinar, and J. Agustin Zornoza, "Broadband design of three-layer printed reflectarrays," *IEEE Transactions on Antennas and Propagation*, vol. 51, no. 7, pp. 1662-1664, July 2003.
- [34] F. Tsai, and M. Bialkowski, "Designing a 161-element Ku-band microstrip reflectarray of variable size patches using an equivalent unit cell waveguide approach," *IEEE Transactions on Antennas and Propagation*, vol. 51, no. 10, pp. 2953-2962, Oct 2001.
- [35] P. Nayeri, F. Yang, and A. Elsherbeni, "Broadband reflectarray antennas using double-layer subwavelength patch elements," *IEEE Antennas and Wireless Propagation Letters*, vol. 9, pp. 1139-1142, 2010.
- [36] H. Hasani, M. Kamyab, and A. Mirkamali, "Broadband reflectarray antenna incorporating disk elements with attached phase-delay lines," *IEEE Antennas and Wireless Propagation Letters*, vol. 9, pp. 156-159, 2010.
- [37] I. Derafshi, N. Komjani, and M. Mohammadirad, "A single-layer broadband reflectarray antenna by using quasi-spiral phase delay line," *IEEE Antennas and Wireless Propagation Letters*, vol. 14, pp. 84-87, 2015.
- [38] R. Malfajani, and Z. Atlasbaf, "Design and implementation of a broadband single-layer reflectarray antenna with large-range linear phase elements," *IEEE Antennas and Wireless Propagation Letters*, vol. 11, pp. 1442-1445, 2012.
- [39] P. Qin, Y. Guo, and A. Weily, "Broadband reflectarray antenna using subwavelength elements based on double square meander-line rings," *IEEE Transactions on Antennas and Propagation*, vol. 64, no. 1, pp. 378-383, Jan 2016.
- [40] Q. Li, Y. Jiao, and G. Zhao, "A novel microstrip rectangular-patch/ring-combination reflectarray element and its application,"

- IEEE Antennas and Wireless Propagation Letters*, vol. 8, pp. 1119-1122, 2009.
- [41] M. Chaharmir, J. Shaker, and H. Legay, "Broadband design of a single layer large reflectarray using multi cross loop elements," *IEEE Transactions on Antennas and Propagation*, vol. 57, no. 10, pp. 3363-3366, Oct 2009.
 - [42] X. Xia, Q. Wu, H. Wang, C. Yu, and W. Hong, "Wideband millimeter-wave microstrip reflectarray using double-resonance unit cells," *IEEE Antennas and Wireless Propagation Letters*, vol. 16, pp. 4-7, 2017.
 - [43] P. Nayeri, M. Liang, R. Sabory-Garcia, M. Tuo, F. Yang, M. Gehm, H. Xin, and A. Elsherbeni, "3D printed dielectric reflectarrays: low-cost, high-gain antennas at sub-millimeter waves," *IEEE Transactions on Antennas and Propagation*, vol. 62, no. 4, pp. 2000-2008, April 2014.
 - [44] M. Wu, B. Li, Y. Zhou, D. Guo, Y. Liu, F. Wei, and X. Lv, "Design and measurement of a 220 GHz wideband 3-D printed dielectric reflectarray," *IEEE Antennas and Wireless Propagation Letters*, vol. 17, no. 11, pp. 2094-2098, Nov 2018.
 - [45] B. Li, C. Mei, Y. Zhou, and X. Lv, "A 3-D-printed wideband circularly polarized dielectric reflectarray of cross-shaped element," *IEEE Antennas and Wireless Propagation Letters*, vol. 19, no. 10, pp. 1734-1738, Oct 2020.
 - [46] A. H. Abdelrahman, A. Z. Elsherbeni, and F. Yang, "Transmission phase limit of multilayer frequency-selective surfaces for transmitarray designs," *IEEE Transactions on Antennas and Propagation*, vol. 62, no. 2, pp. 690-697, Feb 2014.
 - [47] X. Yi, T. Su, X. Li, B. Wu, and L. Yang, "A double-layer wideband transmitarray antenna using two degrees of freedom elements around 20 GHz," *IEEE Transactions on Antennas and Propagation*, vol. 67, no. 4, pp. 2798-2802, April 2019.
 - [48] C. Tian, Y. Jiao, G. Zhao, and H. Wang, "A wideband transmitarray using triple-layer elements combined with cross slots and double square rings," *IEEE Antennas and Wireless Propagation Letters*, vol. 16, pp. 1561-1564, 2017.

- [49] K. Pham, T. Nguten, A. Clemente, L. Palma, L. Cop, L. Dussopt, and R. Sauleau, "Design of wideband dual linearly polarized transmitarray antennas," *IEEE Transactions on Antennas and Propagation*, vol. 64, no. 5, pp. 2022-2026, May 2016.
- [50] A. H. Abdelrahman, P. Nayeri, A. Elsherbeni, and F. Yang, "Bandwidth improvement methods of transmitarray antennas," *IEEE Transactions on Antennas and Propagation*, vol. 63, no. 7, pp. 2946-2954, July 2015.
- [51] Y. Cai, W. Li, K. Li, S. Gao, Y. Yin, L. Zhao, and W. Hu, "A novel ultrawideband transmitarray design using tightly coupled dipole elements," *IEEE Transactions on Antennas and Propagation*, vol. 67, no. 1, pp. 242-250, Jan 2019.
- [52] Y. Ge, C. Lin, and Y. Liu, "Broadband folded transmitarray antenna based on an ultrathin transmission polarizer," *IEEE Transactions on Antennas and Propagation*, vol. 66, no. 11, pp. 5974-5981, Nov 2018.
- [53] K. Marakakis, H. Luyen, J. Booske, and N. Behdad, "Wideband transmitarrays based on polarization-rotating miniaturized-element frequency selective surfaces," *IEEE Transactions on Antennas and Propagation*, vol. 68, no. 3, pp. 2128-2137, Mar 2020.
- [54] C. Jouanlanne, A. Clemente, M. Huchard, J. Keignart, C. Barbier, T. Nadan, and L. Petit, "Wideband linearly polarized transmitarray antenna for 60 GHz backhauling," *IEEE Transactions on Antennas and Propagation*, vol. 65, no. 3, pp. 1440-1445, Mar 2017.
- [55] S. Liu, H. Sato, and Q. Chen, "A wideband, 1-bit transmitarray antenna design with flat gain response," *IEEE Transactions on Antennas and Propagation*, vol. 68, no. 10, pp. 7046-7055, Oct 2020.
- [56] F. Wu, J. Wang, R. Lu, W. Hong, and K. Luk, "Wideband and low cross-polarization transmitarray using 1-bit magnetoelectric dipole elements," *IEEE Transactions on Antennas and Propagation*, vol. 69, no. 5, pp. 2605-2614, May 2021.
- [57] P. Mei, G. F. Pedersen, and S. Zhang, "A broadband and FSS-based transmitarray antenna for 5G millimeter-wave applications," *IEEE Antennas and Wireless Propagation Letters*, vol. 20, no. 1, pp. 103-107, Jan 2021.

- [58] S. Matos, et al., "3-D-Printed transmit-array antenna for broadband backauling 5G links at V-band," *IEEE Antennas and Wireless Propagation Letters*, vol. 19, no. 6, pp. 977-981, June 2020.
- [59] H. Yi, S. Qu, K. Ng, C. H. Chan, and X. Bai, "3-D printed millimeter-wave and terahertz lenses with fixed and frequency scanned beam," *IEEE Transactions on Antennas and Propagation*, vol. 64, no. 2, pp. 442-449, Feb 2016.
- [60] A. Massaccesi, et al., "3D-printable dielectric transmitarray with enhanced bandwidth at millimeter-waves," *IEEE Access*, vol. 6, pp. 46407-46418, 2018.
- [61] T. Sowlati, et al., "A 60-GHz 144-element phased array transceiver for backhaul applications," *IEEE Journal of Solid-State Circuits*, vol. 53, no. 12, pp. 3640-3659, Dec 2018.
- [62] K. Kibaroglu, M. Sayginer, and G. Rebeiz, "A low-cost scalable 32-element 28-GHz phased array transceiver for 5G communication links based on 2 x 2 beamformer flip-chip unit cell," *IEEE Journal of Solid-State Circuits*, vol. 53, no. 5, pp. 1260-1274, May 2018.
- [63] X. Gu, et al., "Development, implementation, and characterization of a 64-element dual-polarized phased-array antenna module for 28-GHz high-speed data communications," *IEEE Transactions on Microwave and Theory Technique*, vol. 67, no. 7, pp. 2975-2984, July 2019.
- [64] Y. Cheng, W. Hong, K. Wu, Z. Kuai, C. Yu, J. Chen, J. Zhao, and H. Tang, "Substrate integrated waveguide (SIW) rotman lens and its ka-band multibeam array antenna applications," *IEEE Transactions on Antennas and Propagation*, vol. 56, no. 8, pp. 2504-2513, Aug 2008.
- [65] J. Lian, Y. Ban, J. Zhu, Y. Liu, and K. Kang, "SIW multibeam antenna based on modified horn beam-forming network," *IEEE Antennas and Wireless Propagation Letters*, vol. 17, no. 10, pp. 1866-1870, Oct 2018.
- [66] P. Chen, W. Hong, Z. Kuai, J. Xu, H. Wang, J. Chen, H. Tang, J. Zhou, and K. Wu, "A multibeam antenna based on substrate integrated waveguide technology for MIMO wireless communications," *IEEE Transactions on Antennas and Propagation*, vol. 57, no. 6, pp. 1813-1821, June 2009.

- [67] J. Lian, Y. Ban, Q. Yang, B. Fu, Z. Yu, and L. Sun, "Planar millimeter-wave 2-D beam-scanning multibeam array antenna fed by compact SIW beam-forming network," *IEEE Transactions on Antennas and Propagation*, vol. 66, no. 3, pp. 1299-1310, March 2018.
- [68] J. Lian, Y. Ban, J. Zhu, K. Kang, and Z. Nie, "Compact 2-D scanning multibeam array utilizing the SIW three-way couplers at 28 GHz," *IEEE Antennas and Wireless Propagation Letters*, vol. 17, no. 10, pp. 1915-1919, Oct 2018.
- [69] Y. Li, L. Gei, M. Chen, Z. Zhang, Z. Li, and J. Wang, "Multibeam 3-D-printed Luneburg Lens fed by magnetoelectric dipole antennas for millimeter-wave MIMO applications," *IEEE Transactions on Antennas and Propagation*, vol. 67, no. 5, pp. 2923-2933, May 2019.
- [70] Q. Liao, N. Fonseca, and O. Quevedo-teruel, "Compact multibeam fully metallic geodesic Luneburg lens antenna based on non-euclidean transformation optics," *IEEE Transactions on Antennas and Propagation*, vol. 66, no. 12, pp. 7383-7388, Dec 2018.
- [71] H. Chou, and Z. Yan, "Parallel-plate Luneburg lens antenna for broadband multibeam radiation at millimeter-wave frequencies with design optimization," *IEEE Transactions on Antennas and Propagation*, vol. 66, no. 11, pp. 5794-5804, Nov 2018.
- [72] G. Wu, S. Qu, and S. Yang, "Wide-angle beam-scanning reflectarray with mechanical steering," *IEEE Transactions on Antennas and Propagation*, vol. 66, no. 1, pp. 172-181, Jan 2018.
- [73] M. Jiang, Z. Chen, Y. Zhang, W. Hong, and X. Xuan, "Metamaterial-based thin planar lens antenna for spatial beamforming and multibeam massive MIMO," *IEEE Transactions on Antennas and Propagation*, vol. 65, no. 2, pp. 464-472, Feb 2017.
- [74] Y. Hu, W. Hong, and Z. Jiang, "A multibeam folded reflectarray antenna with wide coverage and integrated primary sources for millimeter-wave massive applications," *IEEE Transactions on Antennas and Propagation*, vol. 66, no. 12, pp. 6875-6882, Dec 2018.
- [75] J. Yang, Y. Shen, L. Wang, H. Meng, W. Dou, and S. Hu, "2-D scannable 40-GHz folded reflectarray fed by SIW slot antenna in a single-layered PCB," *IEEE Transactions on Microwave and Theory Technique*, vol. 66, no. 6, pp. 3129-3135, June 2018.

- [76] Y. Hu, W. Hong, C. Yu, Y. Yu, H. Zhang, Z. Yu, and N. Zhang, "A digital multibeam array with wide scanning angle and enhanced beam gain for millimeter-wave massive MIMO applications," *IEEE Transactions on Antennas and Propagation*, vol. 66, no. 11, pp. 5827-5837, Nov 2018.
- [77] H. Kamoda, T. Iwasaki, J. Tsumochi, T. Kuki, and O. Hashimoto, "60-GHz electronically reconfigurable large reflectarray using single-bit phase shifter," *IEEE Transactions on Antennas and Propagation*, vol. 59, no. 7, pp. 2524-2531, July 2011.
- [78] H. Yang, F. Yang, S. Xu, Y. Mao, M. Li, X. Cao, and J. Gao, "A 1-bit 10 x 10 reconfigurable reflectarray antenna: design, optimization, and experiment," *IEEE Transactions on Antennas and Propagation*, vol. 64, no. 6, pp. 2246-2254, June 2016.
- [79] E. Carrasco, M. Barba, and J. Encinar, "X-band reflectarray antenna with switching-beam using PIN diodes and gathered elements," *IEEE Transactions on Antennas and Propagation*, vol. 64, no. 6, pp. 2246-2254, June 2016.
- [80] M. Zhang, et al., "Design of novel reconfigurable reflectarrays with single-bit phase resolution for Ku-band satellite antenna applications," *IEEE Transactions on Antennas and Propagation*, vol. 64, no. 5, pp. 1634-1641, Nov 2016.
- [81] H. Zhang, X. Chen, Z. Wang, Y. Ge, and J. Pu, "A 1-bit electronically reconfigurable reflectarray antenna in X-band," *IEEE Access*, vol. 7, pp. 66567-66576, 2019.
- [82] J. Han, L. Li, G. Liu, Z. Wu, and Y. Shi, "A wideband 1 bit 12 x 12 reconfigurable beam-scanning reflectarray: design, fabrication, and measurement," *IEEE Antennas and Wireless Propagation Letters*, vol. 18, no. 6, pp. 1268-1272, June 2019.
- [83] X. Yang, S. Xu, F. Yang, M. Li, Y. Hou, S. Jiang, and L. Liu, "A broadband high-efficiency reconfigurable antenna using mechanically rotational elements," *IEEE Transactions on Antennas and Propagation*, vol. 65, no. 8, pp. 3959-3966, Aug 2017.
- [84] T. Li, and Z. N. Chen, "Metasurface-based shared-aperture 5G S-/K-band antenna using characteristic mode analysis," *IEEE Transactions on Antennas and Propagation*, vol. 66, no. 12, pp. 6742-6750, Dec 2018.

- [85] T. Li, and Z. N. Chen, "Shared-surface dual-band antenna for 5G applications," *IEEE Transactions on Antennas and Propagation*, vol. 68, no. 2, pp. 1128-1133, Feb 2018.
- [86] Y. Chen, and R. G. Vaughan, "Dual-polarized L-band and single-polarized X-band shared-aperture antenna SAR array," *IEEE Transactions on Antennas and Propagation*, vol. 66, no. 7, pp. 3391-3400, Jul 2018.
- [87] J. F. Zhang, Y. J. Cheng, Y. R. Ding, and C. X. Bai, "A dual-band shared-aperture antenna with large frequency ratio, high aperture reuse efficiency, and high channel isolation," *IEEE Transactions on Antennas and Propagation*, vol. 67, no. 2, pp. 853-860, Feb 2019.
- [88] F. Qin, et al., "A simple low-cost shared-aperture dual-band dual-polarized high gain antenna for synthetic aperture radars," *IEEE Transactions on Antennas and Propagation*, vol. 64, no. 7, pp. 2914-2922, Jul 2016.
- [89] D. M. Pozar, and S. D. Targonski, "A shared-aperture dual-band dual-polarized microstrip array," *IEEE Transactions on Antennas and Propagation*, vol. 49, no. 2, pp. 150-157, Feb 2001.
- [90] L. Kong, and X. Xu, "A compact dual-band dual-polarized microstrip antenna array for MIMO-SAR applications," *IEEE Transactions on Antennas and Propagation*, vol. 66, no. 5, pp. 2374-2381, May 2018.
- [91] C. X. Mao, S. Gao, Q. Luo, T. Rommel, and Q. X. Chu, "Low-cost X/Ku/Ka-band dual-polarized array with shared aperture," *IEEE Transactions on Antennas and Propagation*, vol. 65, no. 7, pp. 3520-3527, July 2017.
- [92] Y. Chen, J. Zhao, and S. Yang, "A novel stacked antenna configuration and its applications in dual-band shared-aperture base station antenna array designs," *IEEE Transactions on Antennas and Propagation*, vol. 67, no. 12, pp. 7234-7241, Dec 2019.
- [93] X. Huang, H. Yang, D. Zhang, and Y. Luo, "Ultrathin dual-band metasurface polarization converter," *IEEE Transactions on Antennas and Propagation*, vol. 67, no. 7, pp. 4636-4641, July 2019.
- [94] X. Gao, X. Han, W. Cao, H. Li, H. Ma, and T. Cui, "Ultrawideband and high-efficiency linear polarization converter based on double V-

- shaped metasurface," *IEEE Transactions on Antennas and Propagation*, vol. 63, no. 8, pp. 3522-3530, Aug 2019.
- [95] C. A. Balanis, *Antenna Theory: Analysis and Design*, 4th ed, John Wiley & Sons, Inc., Hoboken, New Jersey, 2016.
 - [96] https://en.wikipedia.org/wiki/Fabry%E2%80%93Perot_interferometer
 - [97] F. Qin, S. Gao, G. Wei, Q. Luo, C. Mao, C. Gu, J. Xu, and J. Li, "Wideband circularly polarized Fabry-Perot antenna [Antenna Applications Corner]," *IEEE Antennas and Propagation Magazine*, vol. 57, no. 5, pp.127-135, Oct. 2015.
 - [98] T. Su, X. Yi, and B. Wu, "X/Ku dual-band single layer reflectarray antenna," *IEEE Antennas and Wireless Propagation Letters*, vol. 18, no. 2, pp. 338-342, Feb 2019.
 - [99] Z. Hamzavi-Zarghani, and Z. Atlashbaf, "A new broadband single-layer dual-band reflectarray antenna in X- and Ku-bands," *IEEE Antennas and Wireless Propagation Letters*, vol. 14, pp. 602-605, 2015.
 - [100] J. Zhao, T. Li, X. Cui, X. Zhao, H. Li, B. Hu, H. Wang, Y. Zhou, and Q. Liu, "A low-mutual coupling dual-band dual-reflectarray antenna with the potentiality of arbitrary polarizations," *IEEE Antennas and Wireless Propagation Letters*, vol. 16, pp. 3224-3227, 2017.
 - [101] R. Deng, Y. Mao, S. Xu, and F. Yang, "A single-layer dual-band circularly-polarized reflectarray with high aperture efficiency," *IEEE Transactions on Antennas and Propagation*, vol. 63, no. 7, pp. 3317-3320, July 2015.
 - [102] T. Smith, U. Gothelf, O. S. Kim, and O. Breinbjerg, "Design, manufacturing, and testing of a 20/30-GHz dual-band circularly polarized reflectarray antenna," *IEEE Antennas and Wireless Propagation Letters*, vol. 12, pp. 1480-1483, 2013.
 - [103] R. Deng, S. Xu, F. Yang, and M. Li, "An FSS-backed Ku/Ka quad-band reflectarray antenna for satellite communications," *IEEE Transactions on Antennas and Propagation*, vol. 66, no. 8, pp. 4353-4358, Aug 2018.
 - [104] R. Deng, F. Yang, S. Xu, and M. Li, "An FSS-backed 20/30-GHz dual-band circularly polarized reflectarray antenna with suppressed

mutual coupling and enhanced performance,” *IEEE Transactions on Antennas and Propagation*, vol. 65, no. 2, pp. 926-931, Feb. 2017.

- [105] M. R. Chaharmir, and J. Shaker, “Design of a multilayer X-/Ka-band frequency selective surface-backed reflectarray for satellite applications,” *IEEE Transactions on Antennas and Propagation*, vol. 63, no. 4, pp. 1255-1262, Apr 2015.

Part II Papers

Paper A

A Broadband and FSS-Based Transmitarray Antenna for 5G
Millimeter-Wave Applications

Peng Mei, Gert Frølund Pedersen, Shuai Zhang

This paper has been published at the
IEEE Antennas Wireless Propagation Letters, vol. 20, no. 1, pp. 103-107,
Jan 2021.

© 2021 IEEE

The layout has been revised and reprinted with permission.

Abstract

This letter describes the design of a broadband and FSS-based transmitarray (TA) antenna for 5G millimeter-wave applications. Two different elements are proposed to avoid the issues of the geometrical parameter resizing of the elements to obtain a 2-bit transmission phase of $\{-\pi, -\pi/2, 0, \pi/2\}$ to achieve a TA antenna with wideband behaviors. Both of the two proposed elements show low insertion loss of below 1 dB from 24 to 38 GHz. Moreover, the two elements can achieve two sets of discrete transmission phases of $\{-\pi, 0\}$ and $\{-\pi/2, \pi/2\}$ without resizing their dimensions, respectively. A TA prototype based on the proposed two elements is designed and fabricated. The measured results agree very well with the simulated ones. The measured 1- and 3-dB gain bandwidth is 28.0-37.5 GHz (29.0 %) and 25.1-39.1 GHz (43.7%), respectively. A peak aperture efficiency of 44.7% at 30 GHz is experimentally obtained with a realized gain of 26.1 dBi.

I Introduction

High gain and wideband millimeter-wave antennas are potentially good solutions to offer high capacity of 2-7 Gb/s to fulfill the rapid growth of mobile data traffic in point-to-point or backhauling communications [1], [2]. Transmitarray (TA) antennas have attracted many interests due to their unique advantages, such as high gain, low cost, simple feeding technique and so on [3]-[6]. Generally, TA antennas suffer from narrow bandwidths due to the resonant properties of the utilized elements. However, the bandwidth limitations of such resonant elements can be improved by optimizing the element structures as reported in [3], [4], [7], [8]. In [4], the authors proposed an element with five metallic layers to achieve a 1-dB gain bandwidth of 24.27% and a maximum aperture efficiency of 62%. The fabrication and implementation of the TA antenna, however, are complicated.

Recently, several novel methods are introduced to design TA antennas with wideband and low-profile properties [9]-[18]. These methods can generally be divided into two categories. The first one is to use different types of elements to provide the required transmission phases that are either continuous or discrete. Each element is responsible for a certain number of discrete transmission phases [9]-[12] or a very small part of the continuous 2π transmission phase range [13], [14]. Since all transmission phases are not

dependent on a single element, the bandwidth or profile of such TA antenna can be improved. In [9], C. Jouanlanne et al. proposed two different elements based on receiver-transmitter structures to offer a 3-bit transmission phase by resizing the dimensions of the two elements. The 1- and 3-dB gain bandwidth is 15.4% and 20%, respectively, with an aperture efficiency of 42.7% at 61.5 GHz. The other method is to rely on a single element implemented by polarization- rotating (PR) structures to provide either continuous [15] or discrete transmission phases [16], [17]. The element is typically configured with three metal layers and two substrates. The top and bottom layers are all metallic polarizer grids placed orthogonally, and the middle layer is a metallic structure with PR properties [15]-[17]. One PR element can naturally provide two different transmission phases (with a phase difference of π) by simply rotating the middle metal layer $\pi/2$. In [17], the authors presented a PR element with cross-shaped metallic strips tilted $\pi/4$ in the middle layer to achieve a 2-bit transmission phase by varying the dimensions of the cross-shaped metallic strips. The corresponding TA antenna was fabricated and measured, revealing a 3-dB gain bandwidth of 24.1%. It should be noticed that the bandwidth the element would be shrunk when its dimensions are varied to achieve two or more transmission phases [9]-[17], leading to lower performance of the corresponding TA antenna.

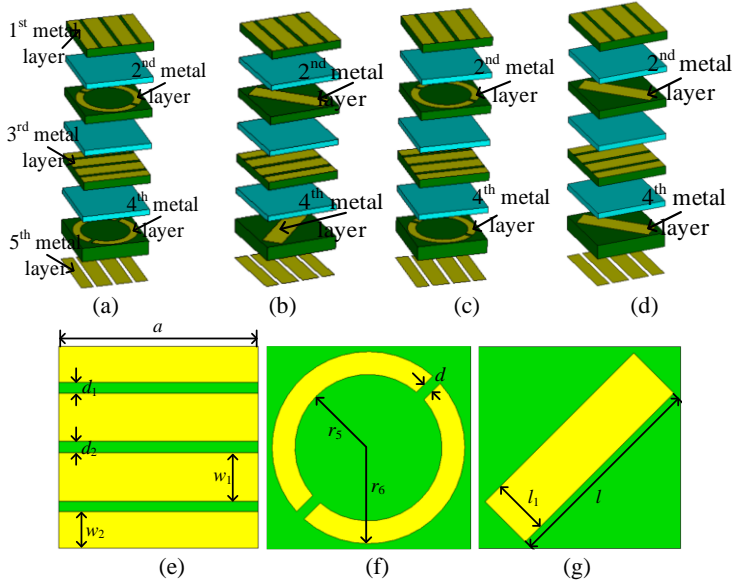


Fig. A. 1. Geometries of the proposed two FSS-based elements with different configurations. Expanded view of (a). Element 1 with a “00” transmission phase, (b). Element 2 with a “01”

transmission phase, (c) Element 1 with a “10” transmission phase, and (d). Element 2 with a “11” transmission phase. Front view of: (e). Polarizer grid of Elements, (f). The 2nd metal layer of Element 1, and (g). The 2nd metal layer of Element 2.

In this letter, we propose a design approach to implement a wideband TA antenna, where two elements with different configurations are proposed to fulfill a 2-bit transmission phase, avoiding resizing the same element. The proposed elements are all based on PR structures with a total thickness of 0.2λ and a unit periodicity of 0.25λ (λ is the wavelength at 30 GHz). Two extra metal layers compared to the PR elements in [15]-[17] are added to make the polarizations of the incident and transmitted waves the same when electromagnetic (EM) wave impinges the element. The proposed two elements are designed to not only provide a 2-bit transmission phase but also maintain low insertion loss in a wide bandwidth. It should be noted that the design approach is also applicable to three-layer elements [e.g. [15]-[17], [19]]. The proposed two elements are described in Section II. The proposed wideband TA antenna is implemented in Section III. Fabrication, measurement, and discussion are carried out in Section IV. Section V concludes the letter finally.

II Element Design

As verified and reported in [9]-[11] and [15]-[17], elements that provide 2- or 3-bit transmission phases are sufficiently feasible to implement TA antennas with fairly good performance. The phase quantization losses for TA or RA antennas have been thoroughly investigated in [20]-[22]. In this section, we focus on designing two different elements capable of providing both a 2-bit transmission phase and low insertion loss in a wide bandwidth, without resizing their dimensions.

Fig. A. 1 presents the geometries of the proposed two elements. Each element consists of five metal layers and four substrate layers. The 1st, 3rd, and 5th metal layers are identical polarizer grids, where the 3rd metal layer is orthogonal to the 1st and 5th metal layers. The 2nd and 4th metal layers are identical polarization-rotating type metallic strips. The supporting substrates (see the green layers in Fig. A. 1) are Rogers 4003C with a dielectric constant of 3.55 and a loss tangent of 0.0027. The supporting substrate of the 4th metal layer is 0.508 mm thick, while the supporting substrates of the 1st, 2nd, and 3rd metal layers are 0.305 mm thick. Three bonding films (see the blue layers in Fig. A. 1) are employed to glue different Rogers 4003C substrates tightly together. The bonding films used here are Rogers 4450F with a dielectric

constant of 3.52, a loss tangent of 0.004, and a thickness of 0.202 mm. The total thickness of the element is 0.2λ (λ is the wavelength at 30 GHz). The proposed element has the following features compared to the structure with three metal layers described in [15]-[17]:

a). The polarizations of the incident and transmitted waves are the same for the proposed TA antenna by adding the two extra metal layers, while it is orthogonal for the one implemented by three metal layers structure in [15]-[17];

b). The transmission phase of the proposed element is doubled when the EM wave propagates through it since there are two identical polarization-rotating type layers (2nd and 4th metal layer). So, it is much easier to obtain to the required phase than those in [15]-[17], which also helps further broaden the bandwidth.

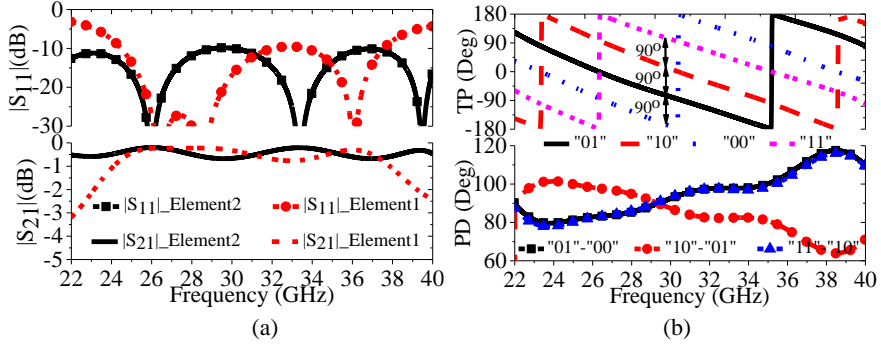


Fig. A. 2. S-parameters of the proposed two FSS-based elements. (a). Reflection and transmission amplitudes of S_{11} and S_{21} . (b) Transmission phases and phase differences of the two FSS-based elements (TP: transmission phase; PD: phase difference).

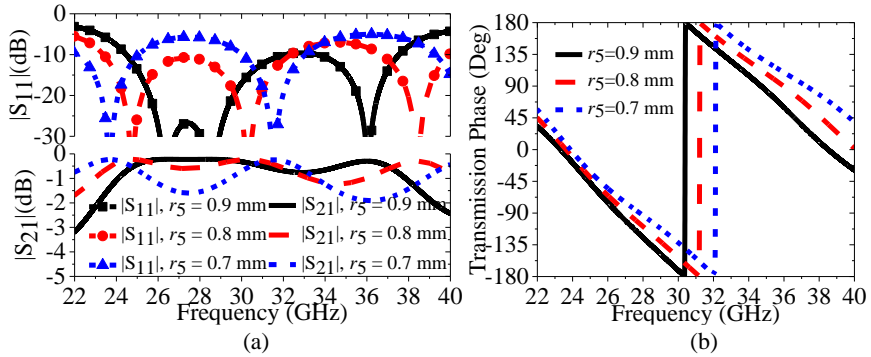


Fig. A. 3. S-parameters of element 1 with a different value of r_5 . (a). Amplitudes of the S-parameters. (b). Transmission phase.

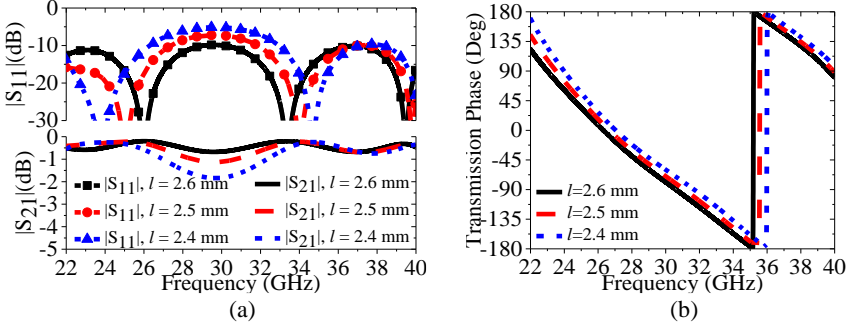


Fig. A. 4. S-parameters of element 2 with a different value of l . (a). Amplitudes of the S-parameters. (b). Transmission phase.

The expanded views of the proposed two elements are shown in Figs. A. 1 (a) - (d), where the split circular ring and rectangular metallic strip tilted $\pi/4$ are selected as the 2nd and 4th metal layers. The dimensions of the two elements are determined to make them operating in the 5G millimeter-wave bands and given as follows: $a = 2.5$ mm, $d_1 = 0.13$ mm, $d_2 = 0.14$ mm, $w_1 = 0.6$ mm, $w_2 = 0.45$ mm, $d = 0.13$ mm, $l = 2.6$ mm, $l_1 = 0.7$ mm, $r_5 = 0.9$ mm, $r_6 = 1.18$ mm.

The proposed two elements are polarization-rotating type structures. Each element can naturally provide two transmission phases with a π phase difference by rotating one polarization- rotating metal layer by 90 deg (either 2nd or 4th metal layer in Fig. A. 1) with all the other dimensions fixed, while still maintaining the amplitudes of its S-parameters [23],[24]. Here, we fix the 2nd metal layer but rotate the 4th metal layer as shown in Figs. A. 1(c) and (d). A 2-bit digital code can be used to characterize the transmission phases of the two elements as seen in Fig. A. 1, where the element 1 provides the transmission phases of $-\pi$ and 0, and the element 2 is responsible for the transmission phases of $-\pi/2$ and $\pi/2$. The S-parameters are carried out with the CST Microwave Studio software. As seen in Fig. A. 2(a), the two elements have low insertion loss from 22 to 40 GHz. In particular, the insertion loss is less than 1dB from 24 to 38 GHz for both two elements. The transmission phases of the elements with different codes are given in Fig. A. 2(b), where a $\pi/2$ transmission phase gradient is achieved from 22 to 40 GHz. The simulated results in Fig. A. 2(a) show that the fractional bandwidth with the insertion loss of below 1dB is up to 45.2%, which is much wider than that reported in [9]-[12], [15]-[17]. It indicates that the bandwidth with low insertion loss can be significantly broadened by applying two different elements to provide a 2-

bit transmission phase without resizing their dimensions.

Parametric studies are carried out to give some guidelines to control the frequency responses of the two elements. Since the proposed two elements are both the polarization-rotating type structures, the dimensions of the 2nd and 4th metal layers are relatively more sensitive to the frequency responses of the proposed two elements. As seen in Fig. A. 3(a), the S-parameter amplitudes of the element 1 vary with r_5 (in Fig. A. 1(f)). A bigger r_5 can provide a larger transmission phase delay as shown in Fig. A. 3(b). For the element 2, it is observed that in Fig. A. 4, a bigger l yields better impedance match, smaller attenuation, and a larger transmission phase delay. The desired transmission phases of the proposed two elements can be obtained by optimizing the values of r_5 and l . Besides, the frequency responses of element 1 and 2 can also be manipulated by tuning the values of d and l_1 , respectively.

The frequency responses of the proposed two elements under transverse electric (TE) and transverse magnetic (TM) oblique incidence waves are also investigated. Since the unit periodicity of the element is only $0.25\lambda * 0.25\lambda$ (λ is the wavelength at 30 GHz) that can be served as a miniaturized structure, the frequency responses under oblique incidence waves are relatively stable (up to at least $\pi/6$), which has been verified by simulations.

III Widband transmitarray antenna design

In this section, the proposed two elements with a 2-bit transmission phase are fully employed to construct a TA antenna. A schematic diagram of the TA antenna is shown in Fig. A. 5(a). The ratio of F/D is closely associated with the beamwidth of the feeding source and is critical for a TA antenna to achieve a good aperture efficiency. F is the distance from the phase center of the feeding source to the transmit-panel, and D is the size of the transmitarray panel. A linearly polarized horn antenna with a type of “PASTERNAK PE9851/2F-10 is adopted as the feeding source. The dimensions and the radiation patterns of the horn antenna can be found from its datasheet in [25], where the operating frequency ranges from 22 to 33 GHz with a nominal gain of 10.0 dBi. It is feasible to extend its operating frequency up to 40 GHz after comparing the simulated and measured radiation patterns of the horn antenna from 33 to 40 GHz. The polarization of the feeding source is y-polarized as illustrated in Fig. A. 5(a). Since the proposed TA antenna features with wide bandwidth, the spillover and illumination efficiencies should be considered at different frequencies. After extensive simulations and optimizations, F and D

are selected as 70 mm and 85 mm, respectively, leading to an F/D ratio of 0.823. The transmit-panel with the size of 85 mm×85 mm is constructed by 34×34 proposed elements in x - and y -directions.

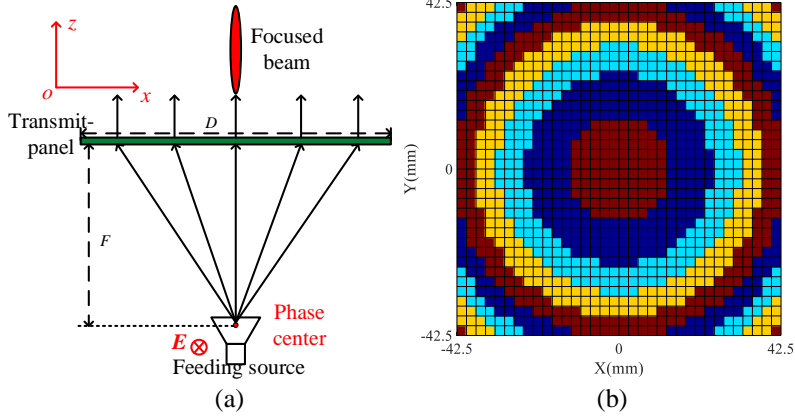


Fig. A. 5. (a). Schematic diagram of a TA antenna. (b). Phase distributions on the plane of the transmit-panel at 28 GHz. (■: $\pi/2$, ■: 0, ■: $-\pi/2$, ■: $-\pi$.)

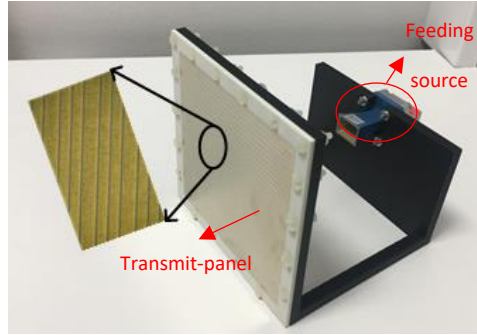


Fig. A. 6. Photograph of the proposed TA antenna.

Once F and D are determined, the phase distributions on the plane of the transmit-panel are obtained accordingly from the simulations at the frequency of interest, which typically ranges from $-\pi$ to $+\pi$. Since the proposed two elements can only offer four different transmission phases, some approximations should be adopted to make the two elements suitable for a TA antenna design [17]. Using the approximations, the final phase distributions on the plane of the transmit-panel are obtained and plotted in Fig. A. 5(b). Based on the phase distributions, the transmit-panel is configured with the

proposed two elements accordingly, and the full TA antenna is simulated with the CST Microwave Studio. The loss budget of the proposed TA antenna consists of spillover loss, illumination loss, and phase quantization loss, where the spillover and illumination efficiencies are explicitly described in [26].

IV Fabrication, Measurement, and Discussion

In this section, the proposed TA antenna has been fabricated and measured. The transmitarray panel was produced with a printed circuit board (PCB) technology [27]. Fig. A. 6 presents a photograph of the proposed TA antenna. There are 18 air holes with the diameters of 3 mm uniformly distributed at the edge of the fabricated transmit-panel and the 3D printing fixture for assembling them with plastic screws.

A. Reflection Coefficient

The reflection coefficient of the proposed TA antenna is measured. As seen in Fig. A. 7(a), the measured -10 dB bandwidth is from 22 to 40 GHz, which aligns with the simulated one. The reflection coefficient at 39 GHz is slightly higher than -10 dB, which is mainly attributed to effects of the coaxial to waveguide transition. In simulation, the coaxial to waveguide transition is not modelled and considered since its specific dimensions are not available from its datasheet.

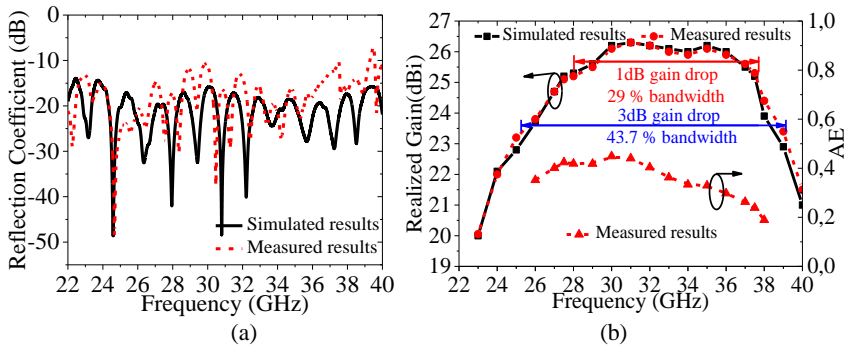


Fig. A. 7. (a). Measured and simulated reflection coefficients of the proposed TA antenna. (b). Measured and simulated realized gain of the proposed TA antenna and the measured aperture efficiency (AE).

B. Realized gain and radiation patterns

The realized gain of the proposed TA antenna is measured and presented in Fig. A. 7(b), where the simulated counterpart is also plotted for comparison. It is observed that the measured results agree very well with the simulated

ones. The measured realized gains are slightly higher than the simulated counterparts at some frequencies, which are common in wideband transmitarray antennas [9], [11], [15], [16]. Based on the measured realized gain, the 1- and 3-dB gain bandwidths are calculated, revealing a fractional bandwidth of 29% and 43.7%, respectively. The aperture efficiency is also calculated with the measured realized gain. As seen in Fig. A. 7(b), the proposed TA antenna can reach a peak aperture efficiency of 44.7% at 30 GHz with the realized gain of 26.1 dBi. The aperture efficiency is above 40.0% from 27 to 32 GHz with a fractional bandwidth of 16.9%.

The radiation patterns of the proposed TA antenna are measured. The normalized radiation patterns at 27.5 and 37.5 GHz are presented in Fig. A. 8, where the simulated results are also plotted. It is observed that the measured radiation patterns of co-polarization (co-pol) agree with the simulated counterparts. The main beams, first radiation nulls, and sidelobes are consistent between the measured and simulated results as observed from the insets in Fig. A. 8. Both of the measured sidelobes in E- ($yo\bar{z}$) and H-plane ($xo\bar{z}$) at 27.5 and 37.5 GHz are below -18 dB. The measured normalized cross-polarizations (cro-pol) of the proposed TA antenna are below -30 dB in E- ($yo\bar{z}$) and H-plane ($xo\bar{z}$) at 27.5 and 37.5 GHz.

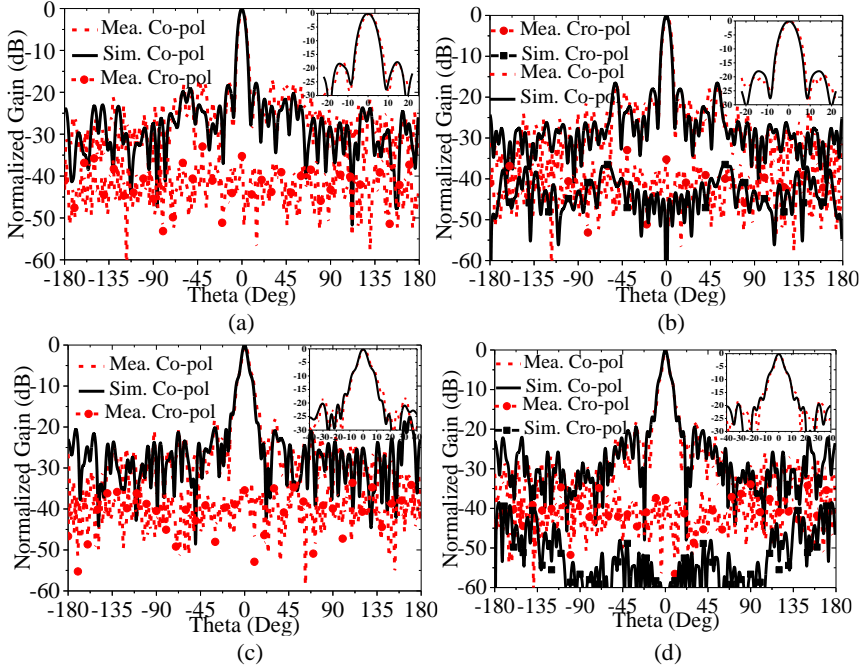


Fig. A. 8. Measured and simulated normalized radiation patterns of the proposed TA antenna at different frequencies. E-plane ($yo\bar{z}$) at: (a) 27.5 GHz, (c) 37.5 GHz; H-plane ($xo\bar{z}$) at: (b) 27.5 GHz, (d) 37.5 GHz.

Tab. A. I. Performance comparison of the proposed TA antenna with other similar TA antennas.

Ref.	f_0 /RG (GHz)/ (dBi)	PS /Layers	Thick ness	F/D Ratio	AE (%)	1/3-dB BW (%)	SG (dBi)
Pro.	30/ 26.1	4/5	0.2λ	0.823	44.7	29/43.7	11.0
[16]	29/ 25.2	4/3	0.1 λ	0.88	45.2	7*/26.6	14.0
[17]	10/ 27.2	4/3	0.05 λ	1	40.7	16*/24. 1	N. A
[9]	61.5/ 32.5	8/3	0.22 λ	0.67	42.7	15.4/20 *	14.1

Pro.: Proposed; RG: realized gain; PS: phase states; AE: aperture efficiency; SG: source gain; *: calculated from the measured results; BW: bandwidth.

Comprehensive comparisons are made to compare the proposed TA antenna with state-of-the-art TA antennas as summarized and illustrated in Tab. A. I. It is observed that the proposed TA antenna achieves a wider 1- and 3-dB gain bandwidth and a comparable aperture efficiency by using a 2-bit transmission phase quantization. The thickness of our proposed element is larger than that in [16] and [17] since two extra layers are added to ensure the polarization identical between the feeding source and the entire TA antenna.

V Conclusion

This letter has developed a wideband transmitarray antenna based on FSS-based elements. Two different elements have been utilized to achieve wideband behaviors and avoid the issues of geometrical parameter resizing of the elements to obtain a 2-bit transmission phase. A TA antenna prototype based on the proposed two elements has been fabricated and measured. The measured results agree very well with the simulated ones, revealing a 1- and 3-dB gain bandwidth of 29% and 43.7%, respectively. The prototype reaches a peak aperture efficiency of 44.7% at 30 GHz with a realized gain of 26.1 dBi. The proposed TA antenna is a good candidate for 5G millimeter-wave applications due to its wide bandwidth and stable radiation performance.

Reference

- [1] T. S. Rappaport et al., "Millimeter-wave mobile communications for 5G cellular: it will work!" *IEEE Access*, vol. 1, pp. 335-349, May 2013.
- [2] C. Dehos, J. L. Gonzslez, A. De Domenico, D. Ktenas, and L. Dussopt, "Millimeter-wave access and backhauling: The solution to the exponential data traffic increase in 5G mobile communications systems?" *IEEE Communication Magazine*, vol. 52, no. 9, pp. 88-95, sep. 2014.
- [3] H. Abdelrahman, A. Z. Elsherbeni, and F. Yang, "High-gain and broadband transmitarray antenna using triple-layer spiral dipole elements," *IEEE Antennas and Wireless Propagation Letters*, vol. 13, pp. 1288-1291, 2014.
- [4] S. Tuloti, P. Rezaei, and F. Hamedani, "High-efficient wideband transmitarray antenna," *IEEE Antennas and Wireless Propagation Letters*, vol. 17, no. 5, pp. 817-820, May. 2018.
- [5] Liu, H. Wang, J. Jiang, F. Xue, and M. Yi, "A high-efficiency transmitarray antenna using double split ring slot elements," *IEEE Antennas and Wireless Propagation Letters*, vol. 14, pp. 1415-1418, 2015.
- [6] P. Mei, S. Zhang, X. Q. Lin, and G. F. Pedersen, "A millimeter-wave gain-filtering transmitarray antenna design using a hybrid lens," *IEEE Antennas and Wireless Propagation Letters*, vol. 18, no. 7, pp. 1362-1365, July 2019.
- [7] Y. Cai, W. Li, K. Li, S. Gao, Y. Yin, L. Zhao, and W. Hu, "A novel ultrawideband transmitarray design using tightly coupled dipole elements," *IEEE Transactions on Antennas and Propagation*, vol. 67, no. 1, pp. 242-250, Jan. 2019.
- [8] Abdelrahman, P. Nayeri, A. Elsherbeni, and F. Yang, "Bandwidth improvement methods of transmitarray antennas," *IEEE Transactions on Antennas and Propagation*, vol. 63, no. 7, pp. 2946-2954, Jul. 2015.
- [9] Jouanlanne, A. Clemente, M. Huchard, J. Keignart, C. Barbier, T. Nadan, and L. Petit, "Wideband linearly polarized transmitarray antenna for 60 GHz backhauling," *IEEE Transactions on Antennas and Propagation*, vol. 65, no. 3, pp. 1440-1445, Mar. 2017.

- [10] Moknache, et al., "A switched-beam linearly-polarized transmitarray antenna for V-band backhaul applications," the *10th European Conference on Antennas and Propagation (EuCAP)*, 2011.
- [11] Manzillo, A. Clemente, and J. Gonzalez-Jimenez, "High-gain D-band transmitarrays in standard PCB technology for beyond-5G communications," *IEEE Transactions on Antennas and Propagation*, vol. 68, no. 1, pp. 587-592, Jan. 2020.
- [12] X. Yang, Y. Zhou, L. Xing, and Y. Zhao, "A wideband and low-profile transmitarray antenna using different types of unit-cells" *Microwave and Optical Technology Letters*, vol. 61, pp. 1584-1589, 2019.
- [13] Q. Luo, et al., "A hybrid design method for thin-panel transmitarray antennas," *IEEE Transactions on Antennas and Propagation*, vol. 67, no. 10, pp. 6473-6483, Oct. 2019.
- [14] X. Yi, T. Su, X. Li, B. Wu, and L. Yang, "A double-layer wideband transmitarray antenna using two degrees of freedom elements around 20 GHz," *IEEE Transactions on Antennas and Propagation*, vol. 67, no. 4, pp. 2798-2802, Apr. 2018.
- [15] P. Feng, S. Qu, and S. Yang, "Octave bandwidth transmitarrays with a flat gain," *IEEE Transactions on Antennas and Propagation*, vol. 66, no. 10, pp. 5231-5238, Oct. 2018.
- [16] Y. Ge, C. Lin, and Y. Liu, "Broadband folded transmitarray antenna based on an ultrathin transmission polarizer," *IEEE Transactions on Antennas and Propagation*, vol. 66, no. 11, pp. 5974-5981, Aug. 2018.
- [17] K. Mavrakakis, H. Luyen, J. Booske, and N. Behdad, "Wideband transmitarrays based on polarization-rotating miniaturized-element frequency selective surfaces," *IEEE Transactions on Antennas and Propagation*, vol. 68, no. 3, pp. 2128-2137, Mar 2020.
- [18] N. K. Grady, et al., "Terahertz metamaterials for linear polarization and anomalous refraction," *Science*, vol. 340, no. 6138, pp. 1304-7, Jun 2013.
- [19] L. Marnat, K. Medrar, and L. Dussopt, "Highly integrated high gain substrate-integrated planar lens for wide D-band applications," *14th European Conference on Antennas and Propagation (EuCAP)*, 2020.

- [20] F. Diaby, et al., "Wideband circularly-polarized 3-bit transmitarray antenna in Ka-band," *11th European Conference on Antennas and Propagation (EuCAP)*, 2017.
- [21] Yang, et al., "A study of phase quantization effects for reconfigurable reflectarray antennas," *IEEE Antennas and Wireless Propagation Letters*, vol. 16, pp. 302-305, May. 2016.
- [22] Robert J. Mailloux, *Phased Array Antenna Handbook*, Third Edition, 2018 Artech House, 685 Canton Street Norwood, MA.
- [23] X. Huang H. Yang, D. Zhang, and Y. Luo, "Ultrathin dual-band metasurface polarization converter," *IEEE Transactions on Antennas and Propagation*, vol. 67, no. 7, pp. 4636-4641, Jul. 2019.
- [24] X. Gao, X. Han, W. Cao, H. Li, H. Ma, and T. Cui, "Ultrawideband and high-efficiency linear polarization converter based on double V-shaped metasurface," *IEEE Transactions on Antennas and Propagation*, vol. 63, no. 8, pp. 3522-3530, Aug. 2019.
- [25] <http://everythingrf.com/products/waveguide-horn-antennas/pasternack-enterprises-inc/617-20-pe9851-2f-10>
- [26] Yu, F. Yang, A. Z. Elsherbeni, J. Huang, and Y. Rahmat-Samii, "Aperture efficiency analysis of reflectarray antennas," *Microwave and Optical Technology Letters*, vol. 52, no. 2, pp. 364-372, Feb 2010.
- [27] <http://pcbastore.com>

Paper B

A Wideband 3D Printed Reflectarray Antenna with
Mechanically Reconfigurable Polarization

Peng Mei, Shuai Zhang, Gert Frølund Pedersen

This paper has been published at the
IEEE Antennas Wireless Propagation Letters, vol. 19, no. 10, pp. 1798-1802,
Oct 2020.

© 2020 IEEE

The layout has been revised and reprinted with permission.

Abstract

This letter describes a wideband and polarization- reconfigurable reflectarray (RA) antenna using 3D printed technology for 5G millimeter-wave applications. An air-perforated dielectric stub is proposed as a unit cell (UC) to provide simultaneous polarization-rotation and phase-shifting capabilities. By optimizing the dimensions of the UC, four UCs are found to offer a 90-degree out of phase for transverse electric (TE) and transverse magnetic (TM) incidence waves and a 2-bit reflection phase of $\{-\pi, -\pi/2, 0, \pi/2\}$, which are employed to implement the reflective panel. By rotating the reflective panel mechanically, the proposed RA antenna can achieve linear polarization (LP), left-hand circular polarization (LHCP), and right-hand circular polarization (RHCP) modes. The measured results are highly consistent with the simulated counterparts, indicating that the proposed RA antenna can reach a 3-dB axial ratio (AR) bandwidth of 43.2 %, and 37.5 % for RHCP and LHCP modes, respectively. Besides, a 3-dB gain bandwidth of 37.5 %, 34.4 %, and 37.5 % is experimentally obtained for RHCP, LHCP, and LP modes of the proposed RA antenna, respectively.

I Introduction

Polarization-reconfigurable antennas play important roles in wireless communication systems [1]-[3]. Lots of efforts have been dedicated to improving the performance of such antennas [4]-[16]. One of the popular techniques to achieve polarization agility is to design a radiator loading with PIN diodes [4]-[8], where the radiator can work in a linearly or circularly-polarized manner by controlling the bias voltages. In [6], the authors proposed a reconfigurable corner-truncated patch loading with four PIN diodes to achieve linear polarization (LP), left-hand circular polarization (LHCP), and right-hand circular polarization (RHCP), resulting in a 3-dB axial ratio (AR) bandwidth of 1.5 % for LHCP and RHCP modes. Another widely-used one is to use reconfigurable feeding networks [9]-[14]. The authors in [13] designed a microstrip-slot line- coplanar waveguide feed network loading with three PIN diodes to generate LP, LHCP, and RHCP modes by manipulating the bias voltages, where a 3-dB AR bandwidth of 14.5 % and 15.0 % is obtained for LHCP and RHCP modes, respectively. The polarization agility of reconfigurable antenna can also be obtained by mechanically rotating the metasurface or superstrate above a slot planar antenna [15] or a L-probe feed [16]. The mechanical control has its unique superiorities of low loss and

simple structures.

In this paper, a wideband and polarization-reconfigurable reflectarray antenna based on 3D printed technology is proposed for 5G millimeter-wave wireless communications. On one hand, reflectarray antennas can offer high gains without using complicated feeding networks, and are found to achieve reconfigurable beams by controlling the reflection phases of unit cells of the reflectarray [17]-[19]. On the other hand, 3D printed technologies have attracted much attention due to their feasibilities and advantages in antenna manufacturings. Lots of 3D printed antennas have been reported to demonstrate high-gain, low-cost, wideband, and other attractive properties in the millimeter-wave and terahertz frequency bands [20]-[23]. To construct the proposed RA antenna, a dielectric stub with a cuboid-shaped air void is proposed as a unit cell (UC) for the reflective panel implementation. To simplify the proposed RA antenna design, four UCs are optimized to provide a 2-bit reflection phase of $\{-\pi, -\pi/2, 0, \pi/2\}$ and a 90-degree out of phase for TE and TM incidence waves. The proposed RA antenna can achieve LP, RHCP, and LHCP modes by simply rotating the reflective panel mechanically, maintaining high gain, wide 3-dB AR, and 3-dB gain bandwidths.

II Unit Cell

The geometries of the proposed UC are shown in Fig. B. 1, where it consists of an air-perforated dielectric stub and a metal plate. The electromagnetic properties of the dielectric stub are with a dielectric constant of 2.65 and a loss tangent of 0.01 in the Ka-band. Since one end of the proposed UC is shorted with a metal plate, most of the electromagnetic waves will be reflected for TE and TM incidence waves, resulting in approximate full reflectance. However, the reflection phases at the interface of the air-perforated dielectric stub and air space are discriminated against for TE and TM incidence waves due to the structural asymmetry of the UC. To analyze the reflection phase of the proposed UC, equivalent dielectric constants ϵ_x and ϵ_y are introduced, where ϵ_x and ϵ_y represent the dielectric constant of the proposed UC in x - and y -direction, respectively. The values of ϵ_x and ϵ_y are closely related to the dimensions of the cuboid air void which is characterized by a length of l , a width of w , and a height of h .

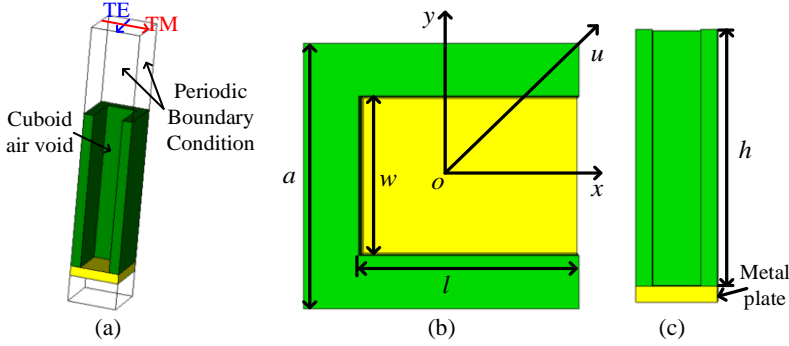


Fig. B. 1. The geometries of the proposed UC. (a). Perspective view. (b). Front view. (c). Side view. ($a = 5.0$ mm, $h = 16.0$ mm.)

Tab. B. I. A 2-bit reflection phase of the proposed UC at 30 GHz under different dimensions ($h = 16$ mm)

	l (mm)	w (mm)	Reflection phase
UC#1	4.3	1.55	-180 deg
UC#2	4.3	2.3	-90 deg
UC#3	4.3	3.0	0 deg
UC#4	4.5	3.5	90 deg

For the proposed UC, it can be equivalent to a transmission line to analyze its reflection phase. For a TE or TM normal incidence wave whose electric field is parallel with the x or y -axis, the reflection phases at the interface of the air-perforated dielectric stub and air space can be calculated as:

$$\theta_x = -\frac{4\pi hf}{c} \sqrt{\varepsilon_x(w, l)} + \varphi_x \quad (1a)$$

$$\theta_y = -\frac{4\pi hf}{c} \sqrt{\varepsilon_y(w, l)} + \varphi_y \quad (1b)$$

where f is the frequency of interest, h is the height of the air-perforated dielectric stub, c is the light speed, φ_x and φ_y are the reflection phases at the interface of the air-perforated dielectric stub and metal plate for TE and TM incidence waves, respectively.

With a specific set of w and l , the reflection phase difference for TE and TM incidence waves is given as:

$$\Delta\theta = \frac{4\pi hf}{c} \left(\sqrt{\varepsilon_y(w, l)} - \sqrt{\varepsilon_x(w, l)} \right) + (\varphi_x - \varphi_y) \quad (2)$$

The reflection phase difference for a TE or TM incidence wave with different sets of w and l can be calculated as:

$$\Delta\theta_x = \frac{4\pi hf}{c} \left(\sqrt{\varepsilon_x(w_1, l_1)} - \sqrt{\varepsilon_x(w, l)} \right) \quad (3a)$$

$$\Delta\theta_y = \frac{4\pi hf}{c} \left(\sqrt{\varepsilon_y(w_1, l_1)} - \sqrt{\varepsilon_y(w, l)} \right) \quad (3b)$$

Eqs. (3) and (4) reveal that it is possible to find out: a). a specific set of w and l to make $\Delta\theta$ equal to 90 degrees; b). some different sets of w and l to make $\Delta\theta_x$ and $\Delta\theta_y$ equal to 90 degrees. When $\Delta\theta$ equals to 90 degrees, the reflection phases in x - and y -direction would be 90-degree out of phase for a u -directed incidence wave, which is essential to generate circular polarization.

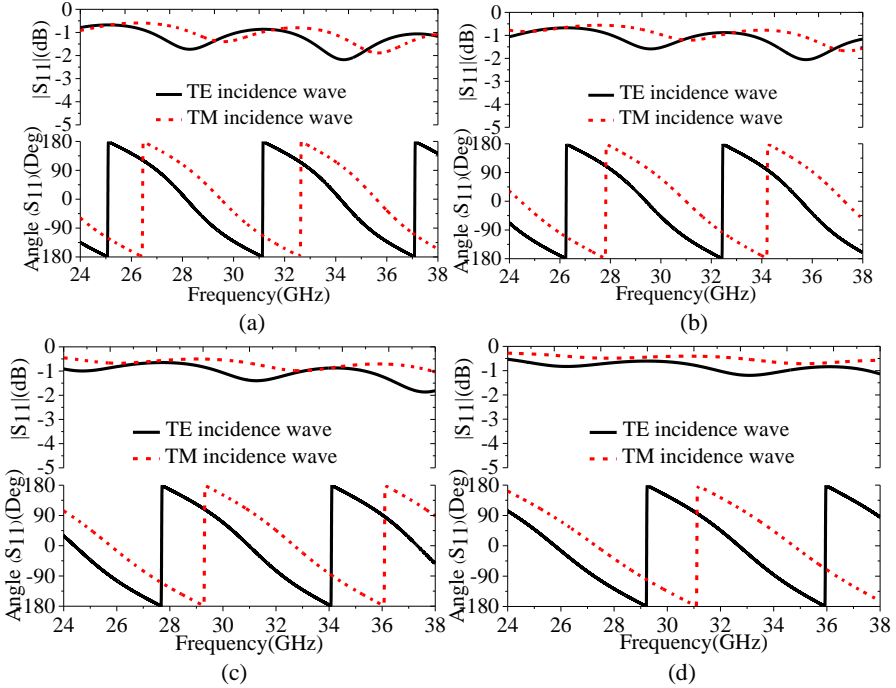


Fig. B. 2. The reflection amplitude and phase of the formed four UCs with TE and TM incidence waves from 24 to 38 GHz. (a). UC#1. (b). UC#2. (c). UC#3. (d). UC#4.

To simplify the implementation of the proposed RA antenna, we mainly focus on finding four sets of w and l to form four UCs, where the four UCs are required to a simultaneous 2-bit reflection phase and 90-degree out of

phase for TE and TM incidence waves. Simulations and optimizations are carried out with CST Microwave Studio Software to find the desired sets of w and l , where the periodic boundary conditions (PBCs) are imposed on the UC to simulate an infinite surface. The values of w , l , and h should also follow the printing accuracy of our available 3D printing technology. Tab. B. I lists a kind of combination of w , l , and h .

The use of dielectric material to construct the proposed UC is attributed to its wideband and minor dispersion properties. To check the wideband performance of the formed four UCs (UC#1, UC#2, UC#3, and UC#4), their reflection amplitudes and phases are simulated with TE and TM incidence waves from 24 to 38 GHz. As seen in Fig. B. 2, the imbalances of reflection amplitudes for all of the four UCs are less than 1 dB from 24 to 38 GHz. Besides, the phase differences for TE and TM incidence waves are around 90 deg, the imbalances of 90-degree out of phase are ± 15 degrees.

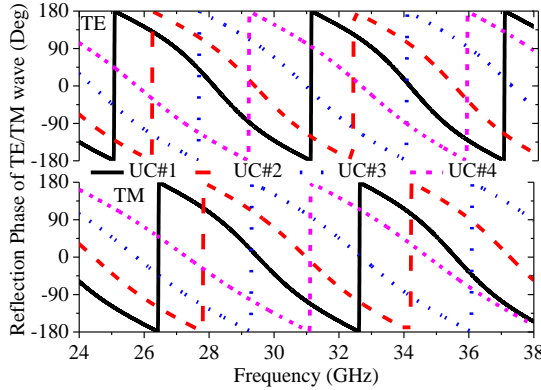


Fig. B. 3. The reflection phases of the formed four UCs with TE or TM normal incidence wave.

A 2-bit reflection phase of $\{-\pi, -\pi/2, 0, \pi/2\}$ provided by the formed four UCs are also examined for TE and TM incidence waves. Fig. B. 3 presents the reflection phases of the formed four UCs, where it is observed that the four UCs can offer a 90 degrees phase gradient from 24 to 38 GHz for both TE and TM incidence waves. Even though the phase gradient between the UC#1 and UC#4 is smaller than 90 deg from 35 to 38 GHz for TM incidence wave, the smaller phase gradient would not impact its abilities for circular polarization generation. The reflection amplitudes and phases of the formed four UCs are also examined with TE and TM oblique incidence waves. It has been demonstrated from the simulated results that the reflection amplitudes and phases are still maintained when the oblique incidence angle reaches 40

degrees for both TE and TM oblique incidence waves over the entire frequency band.

III Wideband and Polarization-Reconfigurable Reflectarray Antenna

The proposed RA antenna implemented by the formed four UCs is investigated. A RA antenna consists of a feeding source and a reflective panel with simultaneous full reflectance and phase-compensating properties. The distance between the phase center of the feeding source and reflective panel is specified as F , the diameter of the reflective panel is D . A centrally-fed method is performed to simplify the proposed RA antenna design. A linearly-polarized horn antenna operating from 22 to 40 GHz is served as the feeding source. To decrease the oblique incidence effects on the UCs, a large F/D ratio is preferred. However, a large F/D ratio would inversely lower the spillover efficiency, leading to reducing the aperture efficiency of the proposed RA antenna [24]. Here, the values of F and D are selected as 70 mm and 110 mm, respectively. Then, the reflection phase distribution on the plane of the reflective panel at 28 GHz is simulated, where the phase of every pixel ranges from -180 to 180 degrees. However, the proposed UCs to implement the reflective panel can only offer a 2-bit reflection phase. To this end, some approximations should be taken to make the UCs feasible for the proposed RA antenna design [25]. Using the approximations, the phase distributions on the plane of the reflective panel are obtained and plotted in Fig. B. 4.

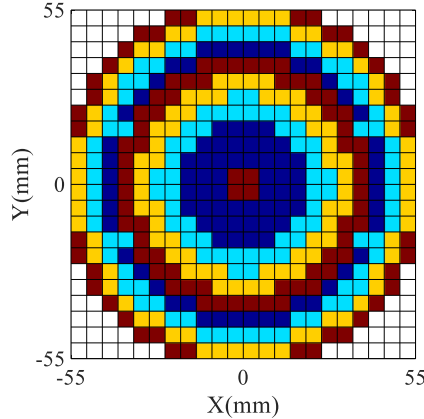


Fig. B. 4. The phase distribution on the plane of the reflective panel at 28 GHz. (■: $\pi/2$, ■: 0, ■: $-\pi/2$, ■: $-\pi$.)

The proposed RA antenna is then configured according to the phase distributions and the formed four UCs. The final model of the proposed RA antenna is presented in Fig. B. 5(a), where the polarization of the feeding source is x-polarized. A 3D printed fixture is used for holding and positioning the feeding source. As introduced in Section. II, the formed four UCs are capable of converting a linearly-polarized wave to a circularly-polarized one. To this end, the proposed RA antenna can achieve different polarizations by simply rotating the 3D-printed dielectric reflective panel with the feeding source fixed, where a RHCP or LHCP mode can be obtained by rotating the reflective panel 45 and 135 degrees anti-clockwise, respectively. The corresponding RA antenna with RHCP and LHCP modes are shown in Figs. B. 5(b) and (c), respectively. It should be mentioned here that the blockage effects of the centrally-fed feeding source can be minimized by using offset-fed techniques as widely reported in [26]-[28].

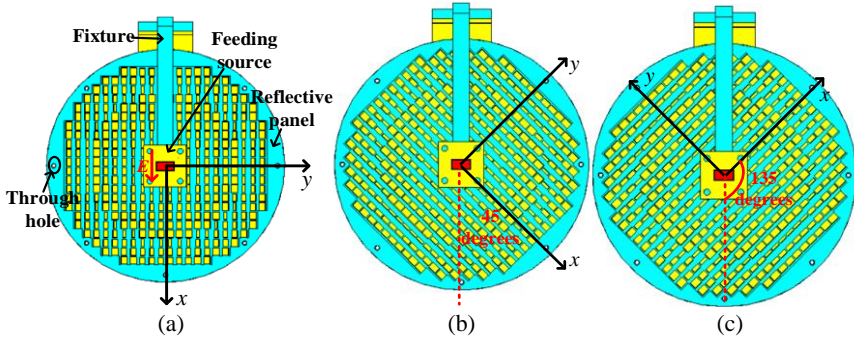


Fig. B. 5. The configuration of the proposed RA antenna. (a). LP mode. (b). RHCP mode. (c). LHCP mode.

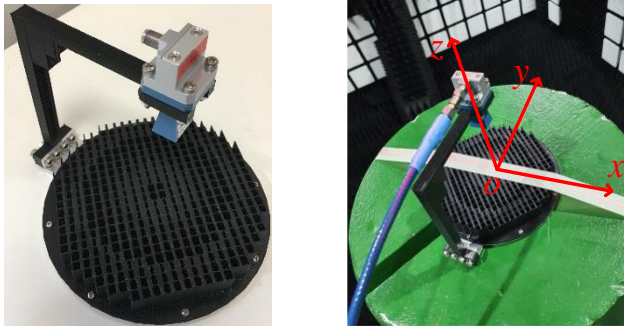


Fig. B. 6. The photographs of the proposed RA antenna and its measurement setup.

IV Experimental Measurement

The proposed RA antenna has been fabricated and measured. The dielectric panel is printed with 3D printed technology and fixed to a metal plate by eight screws. The photograph of the proposed RA antenna is shown in Fig. B. 6.

A. Reflection Coefficient Measurement

The reflection coefficients of the proposed RA antenna with RHCP, LHCP, and LP modes are measured. For brevity, the simulated reflection coefficient with LP mode is presented for comparison. As seen in Fig. B. 7(a), the measured reflection coefficients with RHCP, and LHCP, and LP modes are all below -10 dB from 24 to 38 GHz.

B. Radiation Patterns and Realized Gain Measurements

The realized gains of the proposed TA antenna with RHCP, LHCP, and LP modes are measured and compared with the simulated results. As seen in Figs. B. 7(b)-(d), the measured realized gains agree very well with the simulated counterparts, where 3-dB AR bandwidths of 43.2 % and 37.5 % are obtained for RHCP and LHCP modes, respectively.

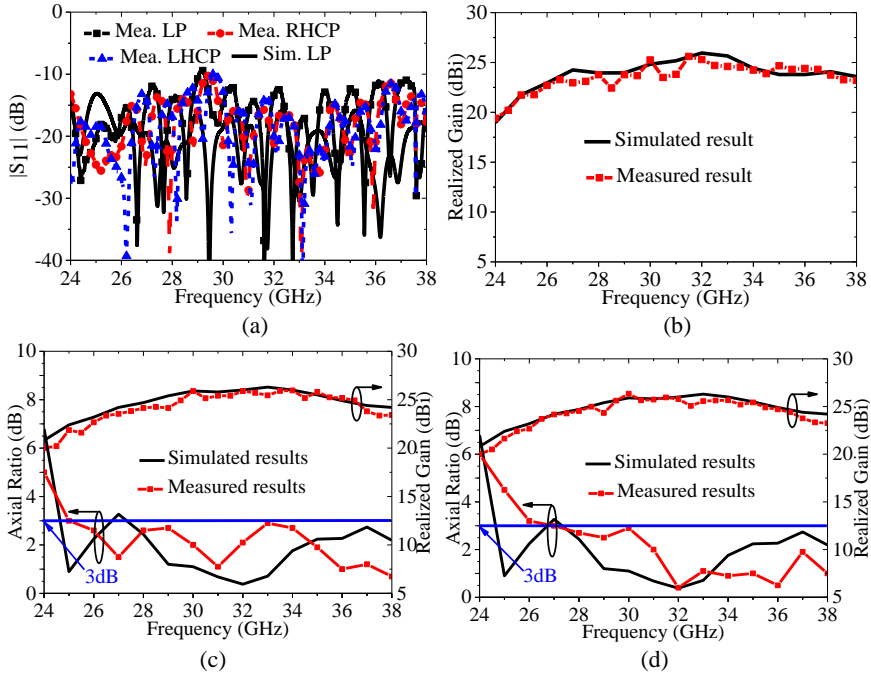


Fig. B. 7. The measured reflection coefficients, realized gains, and axial ratios of the proposed

RA antenna with different polarization modes. (a). $|S_{11}|$. (b). LP mode. (c). RHCP mode. (d). LHCP mode.

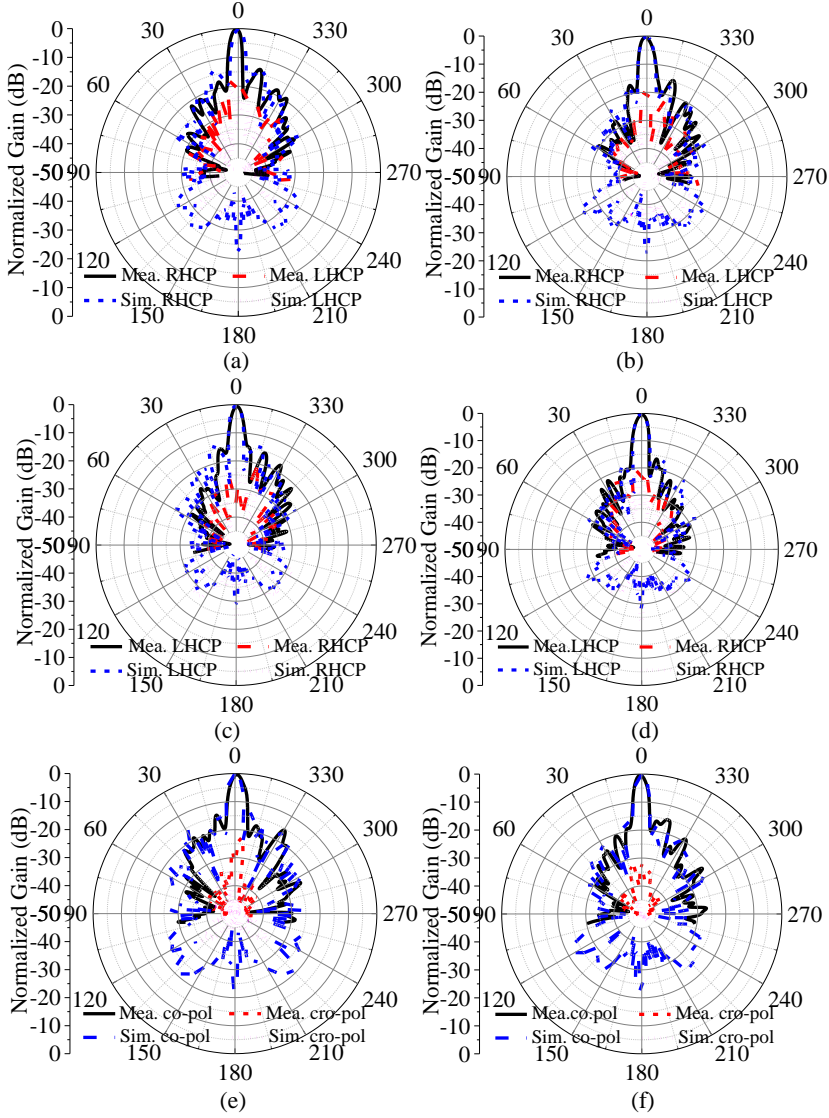


Fig. B. 8. The measured and simulated normalized gain of the proposed RA antenna with RHCP, LHCP, and LP modes at 30 GHz. (a). $\varphi = 0^\circ$, RHCP mode. (b). $\varphi = 90^\circ$, RHCP mode. (c). $\varphi = 0^\circ$, LHCP mode. (d). $\varphi = 90^\circ$, LHCP mode. (e). $\varphi = 0^\circ$, LP mode. (f). $\varphi = 90^\circ$, LP mode.

The measured 3-dB gain bandwidths of 37.5 %, 34.4 %, 37.5 %, and 1-dB gain bandwidths of 18.2 %, 18.6 %, 11.7 % are observed for RHCP, LHCP, and LP modes, respectively. According to the measured realized gains, the

peak aperture efficiencies of the proposed RA antenna at 30 GHz are 32.5 %, 36 %, and 28 %, corresponding to RHCP, LHCP, and LP modes. The aperture efficiency can be further improved by using low-loss material to print the dielectric reflective panel.

The normalized gains of the proposed RA antenna with RHCP, LHCP, and LP modes are measured at 30 GHz in the cut planes of $\varphi = 0^\circ$ and $\varphi = 90^\circ$, where the simulated results are presented for comparison. As seen in Fig. B. 8, the measured results agree well with the simulated ones in terms of main beam, first radiation null, and sidelobe, etc. The sidelobes and cross-polarization levels are all below -15 dB and -20 dB for RHCP, LHCP, and LP modes, respectively. It should be mentioned that the measured radiation patterns of the proposed RA antenna are all broadside and very stable from 24 to 38 GHz for RHCP, LHCP, and LP modes.

Tab. B. II. Comparisons of the proposed RA antenna with other works

Refs	-10dB Bandwidth (%)	AR Bandwidth (%)	3-dB Bandwidth (%)	Peak Gain (dBi)
[4]	8.7 (LP)			10.6(LP)
	16.7(RHCP)	3.2 (RHCP)	N. A	10.2(RHCP)
	18.2(LHCP)	3.7 (LHCP)		9.8(LHCP)
[5]	14.8(LP)			7.0(LP)
	29.6(RHCP)	15.4(RHCP)	N. A	6.2(RHCP)
	29.6(LHCP)	15.4(RHCP)		6.2(LHCP)
[13]	10.8 (LP)		19.2 (LP)	14.7(LP)
	18(RHCP)	15.0 (RHCP)	24 (RHCP)	14.0(RHCP)
	18 (LHCP)	14.5 (LHCP)	23.5(LHCP)	14.2(LHCP)
Proposed	> 37.5	43.2 (RHCP)	37.5 (LP)	25.3(LP)
		37.5 (LHCP)	37.5(RHCP)	26.0(RHCP)
			34.4(LHCP)	25.8(LHCP)

Table. B. II compares the proposed RA antenna with other works. The proposed RA antenna is highlighted by its high gain and wide impedance, 3-dB AR, 3-dB gain bandwidths. Compared to the polarization-reconfigurable antennas enabled by active RF components, the proposed RA antenna has advantages of simple structure and low loss. The effects of RF components on radiation patterns of antennas can be avoided. However, the proposed RA antenna suffers from a slow speed to vary its polarization compared with the ones controlled by DC bias. As a solution, a step motor can be adopted to control the rotations of reflective panel, so that the polarization can also be electrically changed in a high speed.

IV Conclusion

This letter has described a wideband and polarization- reconfigurable millimeter-wave reflectarray (RA) antenna. By simply rotating the reflective panel, the proposed RA antenna can work as a LP, RHCP, or LHCP antenna. The measured 3-dB axial ratio bandwidths for RHCP and LHCP modes are 43.2 % and 37.5 %, respectively. The 3-dB gain bandwidths for RHCP, LHCP, and LP modes are 37.5 %, 34.4 %, and 37.5 %, respectively. Due to the low-cost, high-gain, wideband, and wide 3-dB axial ratio properties, the proposed RA antenna is an attractive candidate for 5G millimeter-wave communication systems.

References

- [1] F. Ferrero, C. Luxey, G. Jacquemod, and R. Staraj, "Dual-band circularly polarized microstrip antenna for satellite," *IEEE Antennas Wireless and Propagation Letters*, vol. 4, pp. 13-15, 2005.
- [2] E. Kaivanto, M. Berg, E. Salonen, and P. Maagt, "Wearable circularly polarized antenna for personal satellite communication," *IEEE Transactions on Antennas and Propagation*, vol. 59, no. 12, pp. 4490-4496, Dec. 2011.
- [3] H. Aissat, L. Cirio, M. Grzeskowiak, J. Laheurte, and O. Picon, "Reconfigurable circularly polarized antenna for short-range communication systems," *IEEE Transaction on Microwave and Theory Technique*, vol. 54, no. 6, pp. 2856-2863, Jun. 2006.
- [4] Q. Chen, J. Li, G. Yang, B. Cao, and Z. Zhang, "A polarization-reconfigurable high-gain microstrip antenna," *IEEE Transactions on*

- Antennas and Propagation*, vol. 67, no. 5, pp. 3461-3466, May. 2019.
- [5] H. Tran, and H. Park, "Wideband reconfigurable antenna with simple biasing circuit and tri-polarization diversity," *IEEE Antennas and Wireless Propagation Letters*, vol. 18, no. 10, pp. 2001- 2005, Oct. 2019.
 - [6] Y. Sung, T. Jang, and Y. Sim, "A reconfigurable microstrip antenna for switchable polarization," *IEEE Microwave and Wireless Component Letters*, vol. 14, no. 11, pp. 534-536, Nov. 2004.
 - [7] A. Khidre, K. Lee, F. Yang, and A. Elsherbeni, "Circular polarization reconfigurable wideband E-shaped patch antenna for wireless applications," *IEEE Transactions on Antennas and Propagation*, vol. 61, no. 2, pp. 960-964, Feb. 2013.
 - [8] B. Kim, B. Pan, S. Nikolaou, Y. Kim, J. Papapolymerou, and M. Tentzeris, "A novel single-feed circular microstrip antenna with reconfigurable polarization capability," *IEEE Transactions on Antennas and Propagation*, vol. 56, no. 3, pp. 630-638, Mar. 2008.
 - [9] D. Seo, J. Kim, M. Tentzeris, and W. Lee, "A quadruple-polarization reconfigurable feeding network for UAV RF sensing antenna," *IEEE Microwave and Wireless Component Letters*, vol. 29, no. 3, pp. 183-185, Mar. 2019.
 - [10] H. Sun, and S. Sun, "A novel reconfigurable feeding network for quad-polarization-agile antenna design," *IEEE Transactions on Antennas and Propagation*, vol. 64, no. 1, pp. 311-316, Jan. 2016.
 - [11] S. Lee, and Y. Sung, "Simple polarization-reconfigurable antenna with T-shaped feed," *IEEE Antennas and Wireless Propagation Letters*, vol. 15, pp. 114-117, 2016.
 - [12] H. Sun, and Z. Pan, "Design of a quad-polarization-agile antenna using a switchable impedance converter," *IEEE Antennas and Wireless Propagation Letters*, vol. 18, no. 2, pp. 269-273, Feb. 2019.
 - [13] N. Zhu, X. Yang, T. Lou, Q. Cao, and S. Gao, "Broadband polarization-reconfigurable slot antenna and array with compact feed network," *IEEE Antennas and Wireless Propagation Letters*, vol. 18, no. 6, pp. 1293-1297, June. 2019.
 - [14] E. Abbas, N. Nguyen-Trong, A. Mobashsher, and A. Abbosh, "Polarization-reconfigurable antenna array for millimeter-wave 5G,"

IEEE Access, vol. 7, pp.131214-131220, Sep. 2019.

- [15] H. Zhu, S. Cheung, X. Liu, and T. Yuk, "Design of polarization reconfigurable antenna using metasurface," *IEEE Transactions on Antennas and Propagation*, vol. 62, no. 6, pp. 2891-2898, June. 2014.
- [16] I. McMichael, "A mechanically reconfigurable patch antenna with polarization diversity," *IEEE Antennas and Wireless Propagation Letters*, vol. 17, no. 7, pp. 1186-1189, July. 2018.
- [17] P. Mei, S. Zhang, and G. Pedersen, "A low-cost, high-efficiency and full-metal reflectarray antenna with mechanically 2-D beam-steerable capabilities for 5G application," *IEEE Transactions on Antennas and Propagation*, vol. 68, no.10, pp. 6997-7006, Oct. 2020.
- [18] T. Debogovic, and J. Perruisseau-Carrier, "Low loss MEMS-reconfigurable 1-bit reflectarray cell with dual-linear polarization," *IEEE Transactions on Antennas and Propagation*, vol. 62, no.10, pp. 5055-5060, Oct. 2014.
- [19] S. Hum, and J. Perruisseau-Carrier, "Reconfigurable reflectarrays and array lens for dynamic antenna beam control: A review," *IEEE Transactions on Antennas and Propagation*, vol. 62, no.1, pp. 183-198, Jan. 2014.
- [20] H. Yi, S. Qu, K. Ng, C. Chan, and X. Bai, "3-D printed millimeter-wave and terahertz lenses with fixed and frequency scanned beam," *IEEE Transactions on Antennas and Propagation*, vol. 64, no.2, pp. 442-449, Feb. 2016.
- [21] P. Mei, S. Zhang, X. Lin, and G. Pedersen, "A millimeter-wave gain-filtering transmitarray antenna design using a hybrid lens," *IEEE Antennas and Wireless Propagation Letters*, vol. 18, no. 7, pp. 1362-1366, July. 2019.
- [22] P. Nayeri, M. Liang, R. A. Sabory-Garcia, M. Tuo, F. Yang, H. Xin, and A. Elsherbeni, "3D printed dielectric reflectarrays: low-cost high gain antennas at sub-millimeter waves," *IEEE Transactions on Antennas and Propagation*, vol. 62, no. 4, pp. 2000-2008, Apr 2014.
- [23] K. Wang, and H. Wong, "A wideband millimeter-wave circularly polarized antenna with 3-D printed polarizer," *IEEE Transactions on Antennas and Propagation*, vol. 65, no. 3, pp. 1038-1046, Mar. 2017.
- [24] A. Yu, F. Yang, A. Elsherbeni, J. Huang, and Y. Rahamt-Samii,

- “Aperture efficiency analysis of reflectarray antennas,” *Microwave and Optical Technology Letters*, vol. 52, no. 3, pp. 771-779, Mar. 2004.
- [25] Y. Ge, C. Lin, and Y. Liu, “Broadband folded transmitarray antenna based on an ultrathin transmission polarizer,” *IEEE Transactions on Antennas and Propagation*, vol. 66, no. 11, pp. 5974-5981, Aug. 2018.
- [26] P. Mei, S. Zhang, Y. Cai, X. Q. Lin, and G. F. Pedersen, “A reflectarray antenna designed with gain filtering and low-RCS properties,” *IEEE Transactions on Antennas and Propagation*, vol. 67, no. 8, pp. 5362-5371, Aug 2019.
- [27] P. Nayeri, M. Liang, R. A. Sabory-Garcia, M. Tuo, F. Yang, H. Xin, and A. Elsherbeni, “3D printed dielectric reflectarrays: low-cost high gain antennas at sub-millimeter waves,” *IEEE Transactions on Antennas and Propagation*, vol. 62, no. 4, pp. 2000-2008, Apr 2014.
- [28] R. Deng, Y. Mao, S. Xu, and F. Yang, “A single-layer dual-band circularly polarized reflectarray with high aperture efficiency,” *IEEE Transactions on Antennas and Propagation*, vol. 63, no. 7, pp. 3317-3320, July 2015.

Paper C

A Low-Cost, High-Efficiency and Full-Metal Reflectarray
Antenna with Mechanically 2D Beam-Steerable Capabilities
for 5G Applications

Peng Mei, Shuai Zhang, Gert Frølund Pedersen

This paper has been published at the
IEEE Transactions on Antennas and Propagation, vol. 68, no. 10, pp. 6997-
7006, Oct 2020.

© 2020 IEEE

The layout has been revised and reprinted with permission.

Abstract

This paper presents a low-cost, high-efficiency, and full-metal reflectarray (RA) antenna with mechanical beam-steerable capabilities. A unit cell (UC) implemented by a metal cylinder with a cuboid-shaped notch is proposed to achieve a 1-bit reflection phase (0 and π) for the transverse electric (TE) and transverse magnetic (TM) normal incidence waves. The proposed UCs can be employed to construct a RA antenna with 2-D beam-steerable abilities. For demonstration, the RA antennas with six different beam directions are presented as examples, by simply adjusting the rotations of the UCs. The impedance matches of the RA antenna are all below -10 dB from 22 to 33 GHz, and the measured radiation patterns of the RA antenna are all highly consistent with the simulated counterparts for the six different beam direction scenarios. A 1.5 dB gain drop bandwidth of approximately 20 % from 24.7 to 30 GHz and a peak realized gain of 18.9 dBi at 26 GHz are experimentally obtained for the RA antenna with radiation patterns at broadside. Compared to the substrate-based UCs loaded with PIN diodes, the proposed UCs have full-metal structures without using any active RF components and dielectric substrates, leading to the high total efficiency of the proposed RA antenna. Due to the low-cost, high-efficiency, and high-power handling properties, the proposed RA antenna can provide a fixed or scanning beam and is a good candidate for 5G millimeter-wave communication applications.

I Introduction

Antennas with beam-steerable capabilities have attracted lots of attention and interests since they can achieve versatile radiation performance. The classical and representative antennas to achieve beam-steerable capacities are phased arrays that every antenna element connects to a phase shifter [1]-[6]. By manipulating the phase shifting of every phase shifter, the phased array is able to realize a 2-D beam steering. Since phase shifters are either bulky or lossy, the phased arrays are not good solutions for lightweight, high-flexibility, and high-efficiency applications. The beamforming network is another effective technique to achieve 2-D scanning beams for a planar array [7]-[13]. However, the beamforming network would be very complicated and extremely lossy for large-scale arrays [10]-[13].

Recently, H. Kamoda *et al.*, [14] proposed a 60-GHz electronically reconfigurable large reflectarray antenna to achieve steerable beams, where the authors designed a unit cell (UC) loaded with a PIN diode. By controlling

the forward and reverse voltages of the PIN diode, the UC can provide two reflection phases with a 180 deg phase difference (e.g., 0 and π). Some approximations are made to replace the actual phase of every unit pixel (that usually ranges from $-\pi$ to π) of a RA antenna with the 1-bit reflection phase provided by the UC. The measured results validated the effectiveness of their design. Afterward, many investigations based on the UC loaded with RF active components were widely carried out [15]-[20]. It should be noted that the usages of many PIN diodes would introduce extra losses to significantly decrease the total efficiencies of such antennas. And the reliability of applying so many PIN diodes simultaneously at millimeter-wave is also a severe issue that constrains the practical applications of such reconfigurable RA antennas. To avoid using PIN diodes, some other techniques were proposed to achieve steerable beams by mechanically rotating the substrate-based UCs as reported in [21]-[23], which can efficiently alleviate the losses caused by PIN diodes to increase the entire efficiency at some extent. In [24], the authors achieved a beam-scanning Fabry-Perot antenna at 11 GHz by mechanically rotating the metasurfaces with phase compensation performance located in the near field, which suffers from a narrow bandwidth and limited beam numbers once the configurations of the metasurfaces were fixed. It is worthwhile to point out, here, even though it has been widely acknowledged, that the losses and prices of active RF components and substrates would all significantly increase with the increment of the operating frequencies.

On the other hand, 5G millimeter-wave bands will be widely used in the near future due to the large available spectrum resources [25], [26]. Millimeter-wave antennas with 2-D beam-steerable capabilities with low-cost and high-efficiency are highly demanded in millimeter-wave communications. In this paper, a low-cost, high-efficiency, and full-metal RA antenna with 2D beam-steerable capacities is proposed for 5G millimeter-wave applications, avoiding usages of any active RF components and dielectric substrates. A UC implemented by a metal cylinder with a cuboid-shaped notch is proposed to construct the proposed RA antenna. It is found that the proposed UC can provide a 1-bit reflection phase (0 and π) for the TE and TM normal incidence waves. Inspired by previously-reported reconfigurable RA antennas implemented by UCs loaded with PIN diodes [14]-[20], a RA antenna with 2-D beam-steerable capabilities can be readily achieved with the proposed UCs by controlling the reflection phases of the UCs. For demonstration, A RA antenna capable of six different main beam directions (e.g. broadside direction, 30 deg and 60 deg off-broadside in E-plane, 30 deg and 60 deg off-broadside in H-plane, and $\theta = 45$ deg, $\phi = 45$

deg) are presented by adjusting the rotation of every UC. Since the proposed UCs are composed of full-metal structures, it is sufficiently predicted that the total efficiency defined by “realized gain/directivity” of the proposed RA antenna would be very high. The simulated total efficiencies of the RA antenna with six different main beam directions are all over 95 %. In addition, it is found that the proposed RA antenna is dual-polarized and has potential abilities for circular polarization applications from the analysis.

The rest of the paper is organized as follows: Section II presents and describes the proposed UC with a full-metal structure, its reflection phases are investigated in detail. Section III introduces the implementations of the RA antenna with six different main beam directions by using the proposed UCs. Fabrications, measurements, and discussions are carried out in Section IV. Finally, some remarkable conclusions are drawn in Section V.

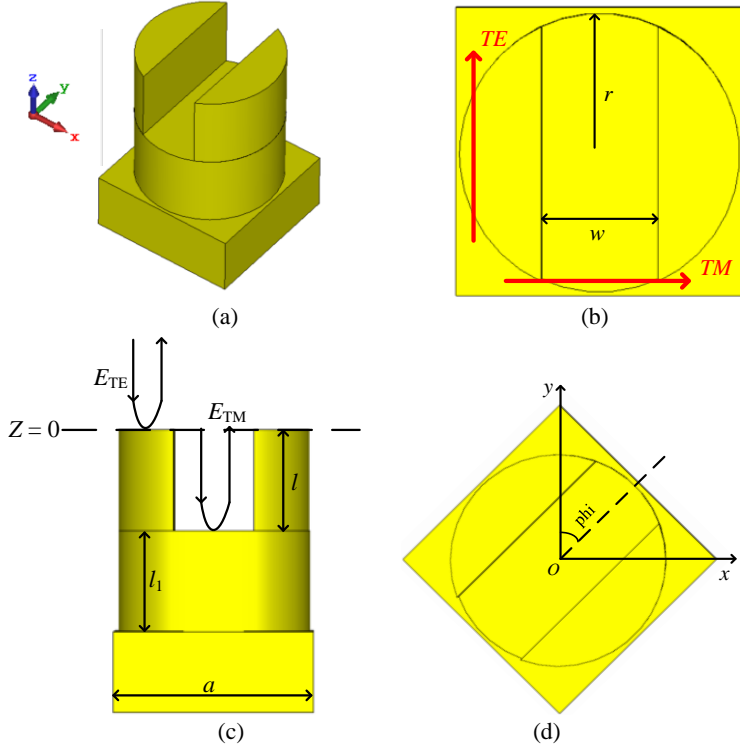


Fig. C. 1. Geometries of the proposed UC with a 1-bit reflection phase property. (a). Perspective view. (b). Top view. (c). Side view. (d). Top view with a ϕ angle offset. ($a=5\text{mm}$, $l_1=2.5\text{mm}$, $l=2.5\text{mm}$, $r=2.45\text{mm}$, $w=2\text{mm}$.)

II Unit Cell Design and Analysis

Fig.C. 1 shows the geometries of the proposed UC with a full-metal structure. It consists of two parts: a square base, and a metal cylinder with a cuboid-shaped notch which is characterized by a width of w and a length of l . It should be noted that the proposed UC can produce different frequency responses for different polarizations of incidence waves. Specifically speaking, the proposed UC with a configuration shown in Fig. C. 1(b) is a polarization-invariant structure for the x- and y-polarized incidence waves, which means the reflected waves are still x- and y-polarized (polarization conversion efficiency is 0), respectively. However, when the proposed UC rotates a ϕ angle with z-axis as shown in Fig. C. 1(d), it would demonstrate polarization rotation abilities with different polarization conversion efficiencies. Particularly, when $\phi = 45^\circ$, the proposed UC provides a perfect polarization rotation performance at a specific frequency (polarization conversion efficiency is 1). That is to say, the reflected wave is y-polarized for x-polarized incidence wave or vice versa. Here, we mainly serve the proposed UC as a polarization-invariant structure. For brevity, we specify that the TE wave is y-polarized while the TM wave is x-polarized. For a TE or TM wave impinging on the UC under normal incidences, the incident electric fields can be written as follows:

$$\vec{E}_{iTE} = \vec{y}E_0e^{jkz}, \quad z \geq 0 \quad (1-a)$$

$$\vec{E}_{iTM} = \vec{x}E_0e^{jkz}, \quad z \geq 0 \quad (1-b)$$

where k is the wavenumber in free space, E_0 is the amplitude of the electric field of incidence wave.

When electromagnetic waves arrive at the plane of $z = 0$ [as marked in Fig. C. 1(c)], some reflections and transmissions for TE and TM incidence waves happen. However, it is found that electromagnetic reflections are dominated for TE incidence wave at the plane of $z = 0$, while electromagnetic transmissions are dominated for TM incidence wave on the same plane. The transmitted TM wave would propagate along with the cuboid-shaped notch and be reflected at the plane of $z = -l$, and then propagate along with the cuboid-shaped notch again. Therefore, the reflected electric fields for TE and TM normal incidence waves are approximately formulated as follows:

$$\vec{E}_{rTE} \approx \vec{y}\Gamma_1 e^{j\varphi_1} \cdot E_0 e^{-jkz}, \quad z \geq 0 \quad (2-a)$$

$$\vec{E}_{rTM} \approx \vec{x}\Gamma_2 e^{j\varphi_2} T^2 e^{j2\phi} E_0 e^{-j(kz-2kl)}, \quad z \geq 0 \quad (2-b)$$

where Γ_1 and φ_1 are reflection amplitude and phase at the plane of $z = 0$ of TE normal incidence wave, respectively. T and ϕ are transmission amplitude and phase at the plane of $z = 0$ of TM normal incidence wave, respectively. Γ_2 and φ_2 are reflection amplitude and phase at the plane of $z = -l$ of TM normal incidence wave, respectively. For the proposed UC, it is found that Γ_i and φ_i ($i=1,2$) are all approaching to 1 and π , respectively. Therefore, we can regard $\Gamma_1 \approx \Gamma_2$ and $\varphi_1 \approx \varphi_2$ approximately.

Based on the reflected electric fields, the phase difference of TE and TM normal incidence waves at the plane of $z = 0$ is calculated and obtained as follows:

$$\Delta\varphi = 2kl + 2\phi \quad (3)$$

If $\Delta\varphi$ is equal to π , Eq. (3) yields to:

$$l = \left(\frac{1}{4} - \frac{\phi}{2\pi}\right)\lambda \quad (4)$$

It should be noted that the transmission phase ϕ is sensitive to the operating frequency f and width of the cuboid-shaped notch w , which is difficult to obtain its exact value. However, based on the Eq. (4), the value of l can be initially given to $\lambda/4$. Then, the desired phase difference (e.g., π) can be obtained by tuning l slightly.

According to the analysis above, some simulations are carried out with CST Microwave Studio to check the performance of the proposed UC, where the periodic boundary conditions (PBCs) are imposed on the UC to simulate an infinite surface to obtain the desired results. The reflection phases and phase differences of TM and TE normal incidence waves with different values of l and other parameters fixed are firstly simulated. As seen in Fig. C. 2 (a), the reflection phases of the proposed UC are more sensitive to the value of l for TM normal incidence wave, which can be explained from Eq. (2-b). From Fig. C. 2(b), the frequency with a phase difference equal to π is shifting toward

a higher frequency with the decrement of l as can be deduced from Eq. (3). When $l = 2.5$ mm, a 180 deg phase difference is obtained at the frequency of 25 GHz. Note that, the quarter-wavelength at 25 GHz is 3.0 mm that is bigger than 2.5 mm. The result is highly consistent with Eq. (4) that the transmission phase ϕ has effects on the value of l .

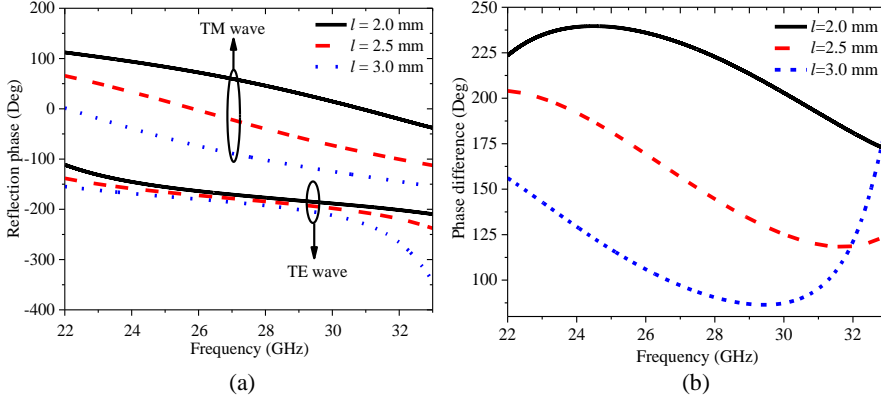


Fig. C. 2. The reflection phase properties of the proposed UC under TE and TM normal incident waves. (a). The reflection phase under TE and TM waves with different values of l . (b). The phase difference with different values of l . ($a=5$ mm, $l_1=2.5$ mm, $r=2.45$ mm, $w=2$ mm.)

From the simulated results, it is concluded that the proposed UC can provide two-phase states with a 180 deg phase difference for a proper value of l . Therefore, a 1-bit digital code is used to characterize the reflection phase of the proposed UC as listed in Tab. C. I.

Tab. C. I. Reflection phase characterization with a 1-bit digital code for the proposed UC

State	Code	Phase
	"0"	0
	"1"	π

As stated and concluded before, the transmission phase ϕ would affect the final reflection phase for TM normal incidence wave, and ϕ is closely associated with the width of the cuboid-shaped notch w and operating frequency f . Tuning w could be an effective technique to control the bandwidth on the reflection phase difference of the proposed UC. Here, simulations are carried out with different values of w to check the phase differences of TE and TM normal incidence waves. As seen in Fig. C. 3, the

slope of the phase differences is becoming smoother with the increment of w . It is concluded that a wider bandwidth on phase difference can be achieved with a bigger value of w to some extent. Considering the mechanical milling precision and preventing the cuboid-shaped notch from deformation, the value of w is chosen as 2.0 mm.

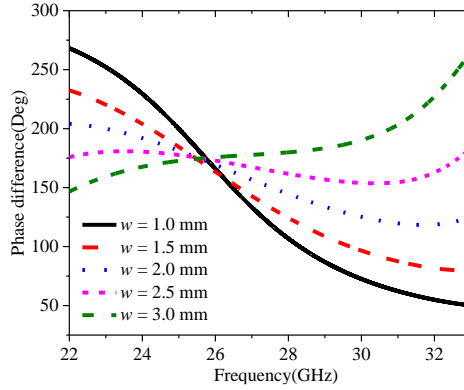


Fig. C. 3. The phase difference of the UC under TE and TM normal incident waves with different values of w .

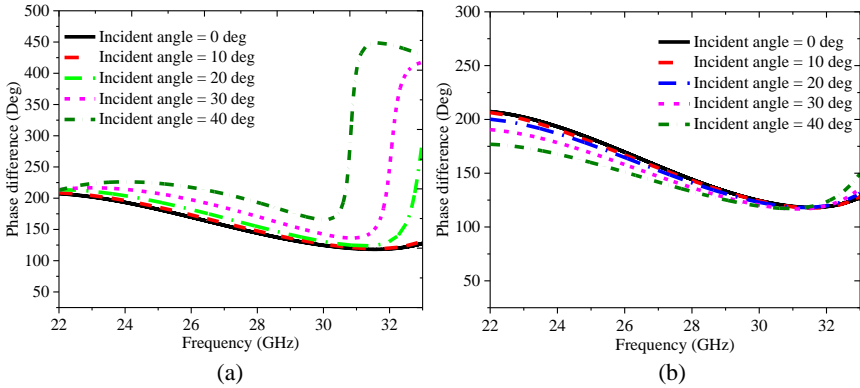


Fig. C. 4. The reflection phase difference of the proposed UC under oblique incidences. (a). TE oblique incident wave (b). TM oblique incident wave.

The reflection phase difference of the proposed UC for TE and TM oblique incidence waves are also simulated and presented. Fig. C. 4 presents the phase differences of the state “0” and state “1”, where it is observed that the phase differences are relatively stable for TE and TM oblique incidence waves until the oblique incidence angle reaches 40 deg from 22 to 30 GHz. The stable phase differences make the proposed UCs good candidates for a RA antenna

design.

III Implementation of the Proposed Antenna

In this section, the proposed UCs with a 1-bit reflection phase are fully employed to construct a RA antenna with mechanically 2-D beam-steerable capabilities. Fig. C. 5 presents a schematic diagram of a RA antenna. It consists of a feeding source and a reflective array with full reflectance and phase compensating properties. A linearly-polarized horn antenna with a model of “PASTERNAK PE9851/2F-10” operating from 22 to 33 GHz is adopted as the feeding source. The dimensions and radiation patterns of the feeding source are available from its datasheet [27]. The simple centrally-fed method is adopted here to verify the concept and effectiveness of the proposed RA antenna. An offset-fed method can be chosen to replace the centrally-fed one to lower its blockage effects on the gain of a RA antenna [28]-[30]. It is widely acknowledged that the phase distributions on the reflective array plane are closely associated with the distance of F and the frequency of interest, and the aperture efficiency of a RA antenna is typically determined by the size of reflective array D , distance F , and the radiation beam of the feeding source that is usually characterized with $\cos^4(\theta)$ [31]. In our design, a low profile and small size are desired, so we select the values of F and D 40 mm and 70 mm, respectively. The polarization of the linearly-polarized feeding source is y -polarized as depicted in Fig. C. 5. Once the dimensions of the proposed RA antenna are determined, the electric fields and phase distributions on the reflective array plane at 26 GHz can be obtained by simulations.

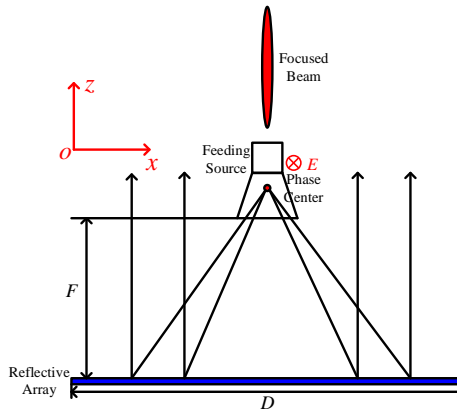


Fig. C. 5. Schematic diagram of a RA antenna.

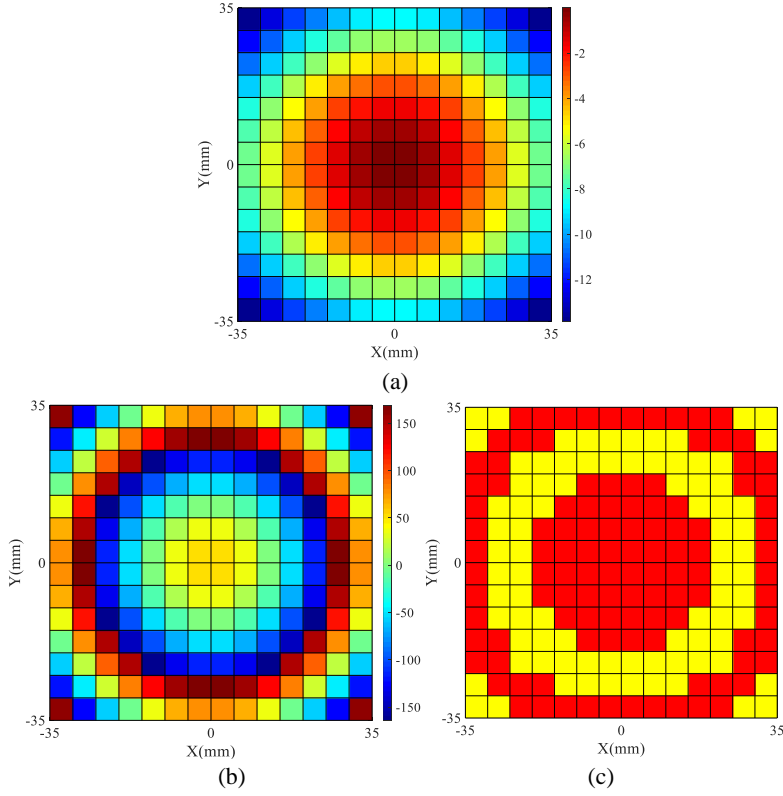


Fig. C. 6. The electric fields and phase distributions on the reflective array surface at 26 GHz. (a). Electric field distributions. (b). Desired phase distributions. (c). Actual phase distributions that the proposed UCs provide. (The red and yellow blocks represent π and 0, respectively.)

Fig. C. 6 plots the electric fields and phase distributions on the reflective array surface at 26 GHz for a broadside radiation pattern. As seen in Fig. C. 6(a), the electric fields reach peak values on the center of the reflective array surface, and the illumination taper of the electric field is about -9 dB at the edge of the reflective array surface. It is also clearly observed that the desired phase on every UC ranges from -180 to 180 degrees in Fig. C. 6(b). However, the proposed UC can only provide a 1-bit reflection phase (e.g., 0 and π). Therefore, some approximations should be made to make the UCs suitable for the proposed RA antenna design:

$$\varphi_{actual} = \begin{cases} 0, & -\frac{\pi}{2} < \varphi_{desired} < \frac{\pi}{2} \\ \pi, & \text{Otherwise} \end{cases} \quad (5)$$

where φ_{desired} is the desired phase on every unit pixel obtained from the simulations, and φ_{actual} is the actual phase that the proposed UC can provide for the corresponding unit pixel. Using the above approximations, the phase distributions on the preselected reflective array plane are updated as shown in Fig. C. 6(c). Based on the actual phase distributions, a RA antenna can be easily implemented by the proposed UCs with proper rotations.

If the main beam of a RA antenna is off-broadside, some phase gradients on the reflective array plane should be imposed. To determine the desired phase compensation on every UC to achieve a beam off-broadside, we can consider the reflective array as a planar array. Every UC in the reflective array can be equivalently regarded as a radiation element. Supposed that a radiation beam is pointing toward (θ_0, φ_0) , the progressive phases of two adjacent UCs in x and y -direction can be calculated by:

$$\beta_x = -kd_x \sin \theta_0 \cos \varphi_0 \quad (6\text{-a})$$

$$\beta_y = -kd_y \sin \theta_0 \sin \varphi_0 \quad (6\text{-b})$$

where β_x and β_y are progressive phases in x - and y -direction, respectively. k is the wavenumber in free space, d_x and d_y are element space in x - and y -direction, respectively. Once the required main beam direction (θ_0, φ_0) , the element space in x - and y -direction, and the interested frequency are all determined, the progressive phases are readily calculated by using Eq. (6).

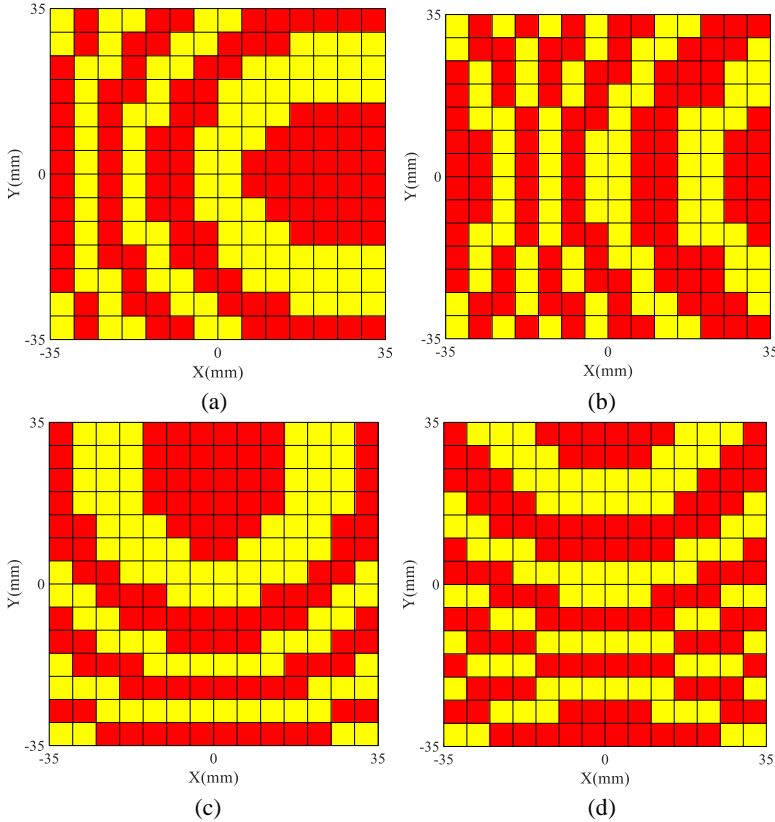
Here, six different main beam directions at 26 GHz are demonstrated: a). broadside direction; b). 30 deg off-broadside in E-plane; c). 60 deg off-broadside in E-plane; d). 30 deg off-broadside in H-plane; e). 60 deg off-broadside in H-plane; f). $\theta = 45$ deg and $\varphi = 45$ deg.

It should be noted that the additions of phase gradients should be added based on a uniform phase distribution. Specifically speaking, for the desired main beam of 30 deg off-broadside in E-plane, the desired phase distributions on the reflective array plane should be obtained by adding the progressive phase in x -direction calculated with Eq. (6-a) to the uniform phase distribution shown in Fig. C. 6(c). Once the desired phase distributions for the main beam of 30 deg off-broadside in E-plane are obtained, the actual phase distributions are determined by using the approximations illustrated in Eq. (5). The final phase distributions on the reflective array plane with the main beam of 30 deg off-broadside in E-plane are presented in Fig. C. 7(a). The actual phase distributions for the remaining four cases are all obtained by using the same

approach, as shown in Figs. C. 7(b)-(e).

Based on the actual phase distributions shown in Fig. C. 6(c) and Fig. C. 7, it is interesting found that a 2-D beam-steerable capability can be achieved by simply adjusting the rotation of every UC of the RA antenna. In this paper, we adjust the rotation of every UC manually to validate the effectiveness of the proposed RA antenna with 2-D beam-steerable capabilities.

As the feeding source is linearly-polarized, the proposed RA antenna has the same polarization accordingly. It should be noted, however, that the proposed RA antenna would be dual-polarized when a dual-polarized feeding source is used. The directions of the main beam for the two polarizations are the same since we adopt a proper phase quantization (0 and π) to implement the reflective array. Even though the proposed UCs don't have abilities to covert a linear polarization of feeding source to a circular polarization for the proposed RA antenna, a circularly-polarized RA antenna would be obtained when the feeding source is a circular polarization as reported in [21].



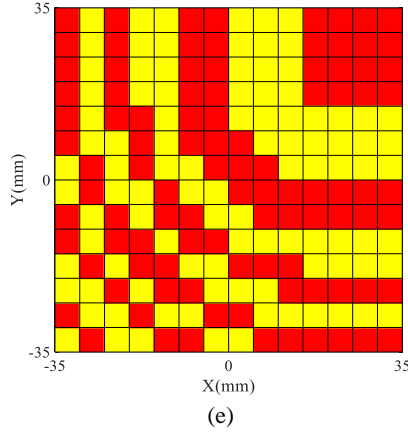


Fig. C. 7. The phase distributions on the reflective plate plane at 26 GHz. (a). 30 deg off-broadside in E-plane. (b). 60 deg off-broadside in E-plane. (c). 30 deg off-broadside in H-plane. (d). 60 deg off-broadside in H-plane. (e). $\varphi = 45$ deg and $\theta = 45$ deg. (The red and yellow blocks represent π and 0, respectively.)

IV Fabrication, Measurement, and Discussion

In this section, the proposed RA antenna is fabricated and its performance is evaluated experimentally. The base and UCs are all manufactured with material Aluminium by using mechanical milling technologies. The UCs are all tightly attached and fixed on the base with metallic screws, pads, and springs to avoid the air gap between the UCs and the base. A 3-D printed fixture is used to hold the feeding source and make the accurate separation from the feeding source to the reflective array. The assembled antenna prototype is shown in Fig. C. 8. Its reflection coefficients are measured with keysight Power Network Analyzer (PNA), radiation patterns and realized gains are evaluated with our advanced anechoic chamber.

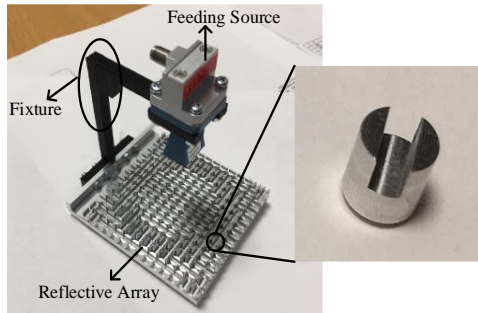


Fig. C. 8. The photograph of the proposed RA antenna.

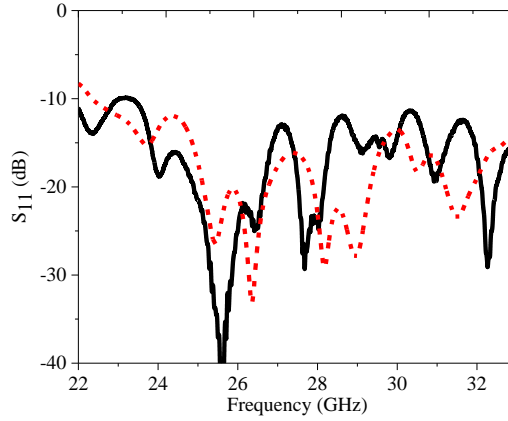


Fig. C. 9. Measured and simulated reflection coefficients of the proposed RA antenna at broadside direction.

A. Reflection coefficients.

Fig. C. 9 presents the measured reflection coefficients of the proposed RA antenna with radiation pattern at broadside, where the simulated counterpart is also plotted for comparison. It is observed that the measured and simulated results agree well with each other, revealing that the reflection coefficients are all below -10 dB from 22 to 33 GHz. Since the blockage of the feeding source would impact the reflection coefficient of the proposed RA antenna with radiation patterns at broadside, it is sufficiently reasonable to predict that the measured reflection coefficients for the other five scenarios are all below -10dB from 22 to 33 GHz, which are all verified by the corresponding measured results that are not presented here.

B. Realized gain and radiation patterns

Fig. C. 10 gives the measurement environment and setup. The measurement setup can be used to measure 3-D radiation patterns of an antenna. The dual-polarized horn antenna at the top ceiling is served as a receiving antenna. The rotary arm connecting to the receiving antenna can rotate in the vertical plane ($yo\bar{z}$ -plane). The rotary table can rotate 360 deg in the horizontal plane (xoy -plane). It should be mainly pointed out that the rotation directions of the rotary table and arm correspond to ϕ and θ , respectively, as marked in Fig. C. 10. The rotary arm can rotate clockwise continuously. The 0 deg means that the receiving antenna is located at the top ceiling or we can consider the receiving antenna is in the z -axis. The rotation resolution of the rotary arm and table can be controlled independently with a computer. Since the proposed RA antenna has six different radiation patterns to be measured, we set the rotation

resolution of the rotary arm and table as 5 and 2 deg to save time and ensure the measurement accuracy at the same time. On the other hand, the radiation patterns of the proposed RA antenna are mainly concerned from -90 to 90 deg, the rotary arm, therefore, is set from 0 to 90 deg to further save measurement time with the rotary table from 0 to 360 deg in the horizontal plane (xy -plane).

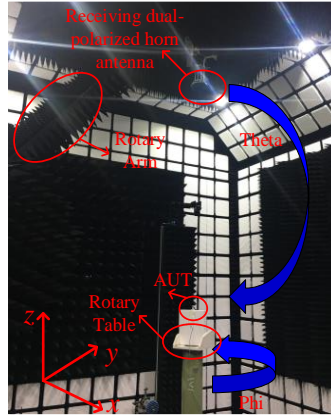


Fig. C. 10. Measurement setup.

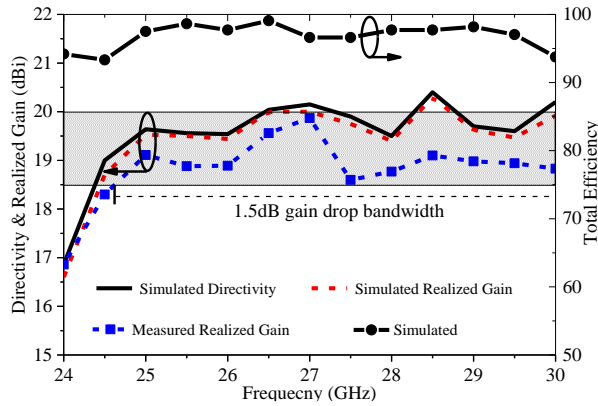
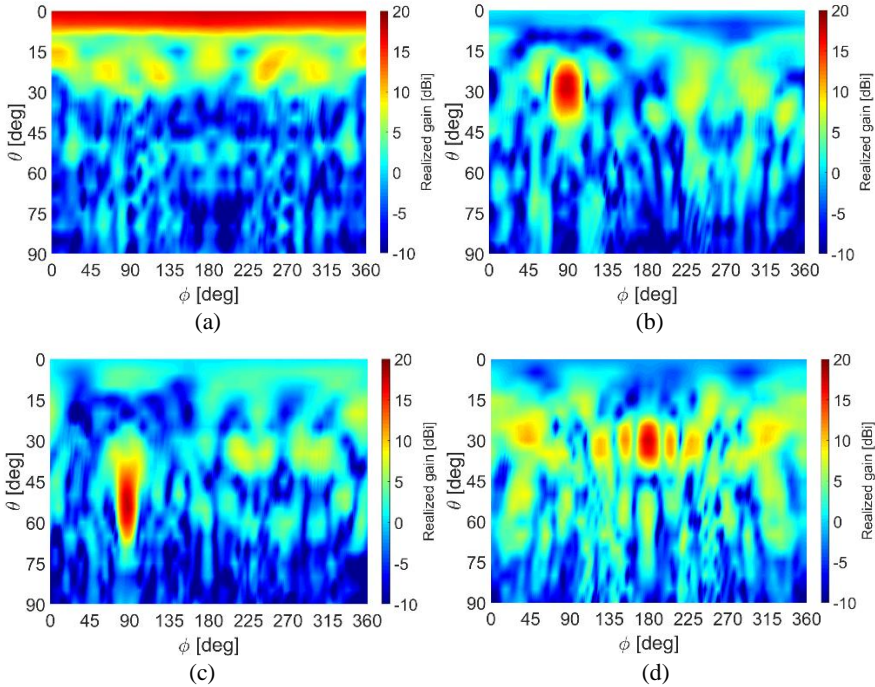


Fig. C. 11. Simulated directivity, realized gain, total efficiency, and measured realized gain of the proposed RA antenna with radiation beam at broadside.

The realized gains of the proposed RA antenna with the main beam at broadside direction are measured from 24 to 30 GHz, where the simulated directivities and realized gains are also plotted for comparison. As seen in Fig. C. 11, the measured realized gains are smaller than the simulated results, the discrepancies are mainly attributed to the following reason besides

measurement and assembling tolerances: the effects of the coaxial to waveguide transition of the feeding source are not considered in simulations since its specific dimensions are not available from its datasheet. However, the measured realized gains include the losses of the coaxial to waveguide transition structure, leading to the lower measured realized gains compared with the simulated ones. The measured and simulated realized gains at 26 GHz are 19.5 dBi and 18.9 dBi with a gain difference of only 0.6 dB. From Fig. C. 11, it is observed that the maximal gain discrepancy between simulated and measured results is less than 1.0 dB from 24 to 30 GHz. Since the proposed RA antenna is a full-metal structure, only conductor losses (no substrate losses) are dominated, leading to the simulated realized gains very close to the simulated directivities as can be seen in Fig. C. 11. Here, the total efficiency defined by “realized gain/directivity” is proposed to evaluate the low losses properties of the proposed RA antenna. Since the measured directivities are not available from the measurement setup, Fig. C. 11 plots the simulated total efficiencies with frequencies, where the total efficiency of more than 90 % is obtained from 24 to 30 GHz. Besides, it is observed from Fig. C. 11 that the measured 1.5 dB gain drop bandwidth of the proposed RA antenna reaches approximately 20 % from 24.7 to 30 GHz.



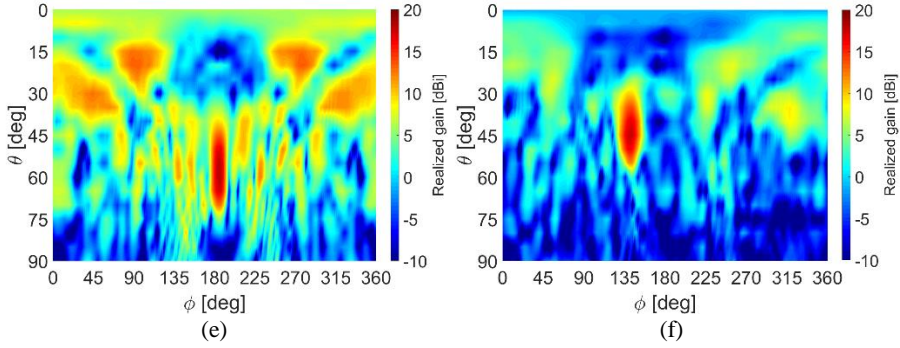
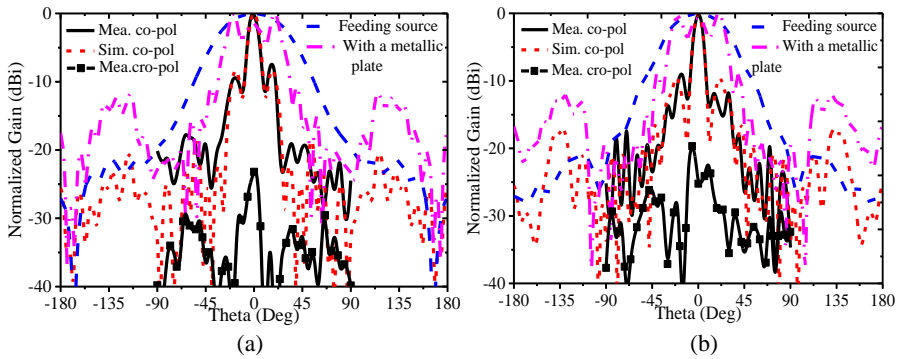


Fig. C. 12. Measured 3-D realized gains of the proposed RA antenna with six different radiation beam directions at 26 GHz. (a). At broadside. (b). At 30 deg off-broadside in E-plane. (c). At 60 deg off-broadside in E-plane. (d). At 30 deg off-broadside in H-plane. (e). At 60 deg off-broadside in H-plane. (f). At $\theta = 45$ deg and $\phi = 135$ deg.

To give more intuitive views on radiation patterns with the different main beam directions. The 3-D radiation patterns of the proposed RA antenna with six different main beam directions are measured and presented at 26 GHz. It should be noted that $\phi = 90$ deg and $\phi = 180$ deg in Fig. C. 12 correspond the E- and H-plane of the RA antenna, respectively according to the relative positions of the measurement setup. From Fig. C. 12(a), it is observed that maximum gains are always concentrated at the location of $\theta = 0$ deg and ϕ ranging from 0 to 360 deg, which means the main beam points to broadside direction. From Figs. C. 12(b)-(f), it is clearly seen that the maximum gains are located at a certain position. Figs. C. 12(b)-(c) present the 3-D beam-steerable radiation patterns in E-plane, it is observed that the measured maximum gain is pointing to 30 and 60 deg approximately, respectively. Likewise, as seen in Figs. C. 12(d)-(e), the measured maximum gain is pointing to 30 and 60 deg in H-plane approximately, respectively. Fig. C. 12(f) shows the measured 3-D radiation pattern whose beam points to $\theta = 45$ deg and $\phi = 45$ deg (135 deg). All the measured main beam directions are highly consistent with the prescribed and calculated main beam directions.

The 2-D radiation patterns of the proposed RA antenna capable of six different main beam directions are also presented and compared. Figs. C. 13(a)-(b) give the measured normalized radiation patterns of the RA antenna in E- and H-plane with the main beam at broadside at 26 GHz, where the simulated counterparts are also plotted for comparison. It is observed that the measured and simulated results are consistent. The main beams, first radiation nulls, and sidelobes are almost identical. To clearly reflect the beam focusing

property of the proposed RA antenna, the simulated radiation patterns in E- and H-plane of the feeding source and a RA antenna whose reflective array surface is replaced by the same size metallic plate are also supplied in Figs. C. 13(a) and (b) at the same frequency. It is seen that the proposed RA antenna (18.9 dBi) has a much higher gain compared to the feeding source (10.3 dBi). Due to the finite size of the metallic plate, there are some minor gain dips in radiation patterns of a RA antenna with a metallic plate as shown in Fig. C. 13(a) and (b). Since the proposed RA antenna is implemented by UCs with only a 1-bit reflection phase, the phase quantization errors would increase the sidelobe of the RA antenna as comprehensively investigated in [32]. The sidelobes in E- and H-plane are -8 dB and -9 dB, respectively. Figs. C. 13(c)-(f) present the normalized radiation patterns with the different main beam directions in E- and H-plane, respectively. Except for Fig. C. 13(e) that the measured sidelobes are slightly higher than that of simulated results, the measured and simulated results shown in Fig. C. 13(c), (d), and (f) are highly consistent regarding the main beams, radiation nulls, and sidelobes. Fig. C. 12(g) shows the normalized radiation pattern of the proposed RA antenna whose main beam points toward $\theta = 45$ deg and $\phi = 45$ deg, where it is observed that the measured and simulated results have extremely great agreements in terms of main beams, radiation nulls, and sidelobes. As seen in Fig. C. 13, the sidelobes of the proposed RA antenna with the different beam pointing directions are all below -10 dB. Besides, the measured cross-polarization (cro-pol) levels on interested cut planes are also plotted in Fig. C. 13, where a -20 dB cross-polarization level is observed for the proposed RA antenna no matter what the main beam direction is.



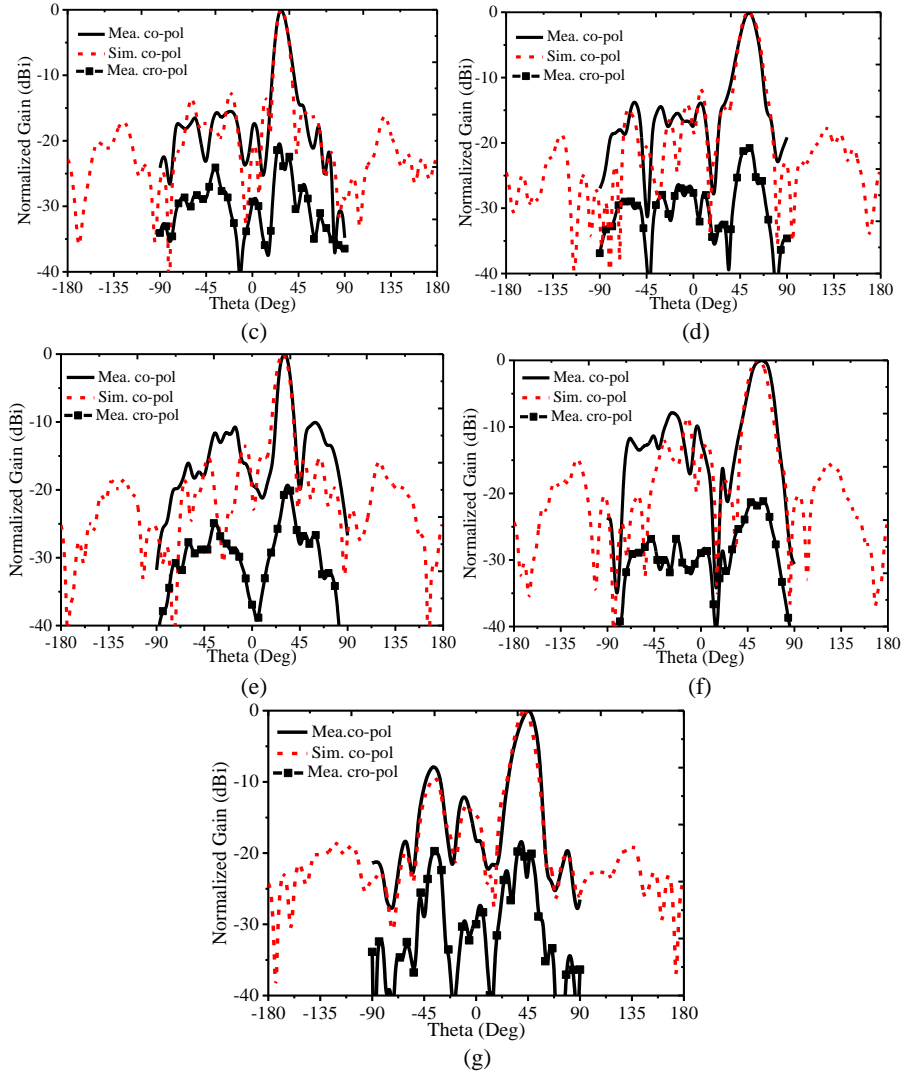


Fig. C. 13. Measured and simulated normalized realized gains of the proposed RA antenna with different radiation beam directions at 26 GHz. (a). E-plane at broadside. (b). H-plane at broadside. (c). 30 deg off-broadside in E-plane. (d). 60 deg off-broadside in E-plane. (e). 30 deg off-broadside in H-plane. (f). 60 deg off-broadside in H-plane. (g). $\theta = 45$ deg and $\phi = 45$ deg.

The radiation performance of the proposed RA antenna is summarized at 26 GHz as listed in Tab. C. II when its main beam points in a different direction. The simulated total efficiencies are all above 97.0 % at six different main beam directions, which is extremely high. Even though the measured

directivities of the proposed RA antenna are not available, it still can be deduced that the total efficiencies of the proposed RA antenna should be high since the measured realized gains considering the heating losses (dielectric, conductor loss) and impedance mismatch of the proposed RA antenna are close to the simulated counterparts very well. Besides, the measured realized gains of the proposed RA antenna at different main beam directions are relatively stable. The measured maximum gain variation of 2.0 dB is observed for the main beam at broadside and 60 deg off-broadside in H-plane.

Tab. C. II. Radiation performance summary of the proposed RA antenna at 26 GHz.

	Simulated directivity & realized gain	Measured realized gain	Simulated total efficiency	Gain variation over the beam-steerable coverage
$\theta = 0$ deg $\phi = 0$ deg	19.6 dBi & 19.5 dBi	18.9 dBi	97.7 %	0 dB
$\theta = 30$ deg $\phi = 0$ deg	18.5 dBi & 18.4 dBi	17.9 dBi	97.7 %	1.0 dB
$\theta = 60$ deg $\phi = 0$ deg	18.7 dBi & 18.6 dBi	18.2 dBi	97.7 %	0.7 dB
$\theta = 30$ deg $\phi = 90$ deg	19.0 dBi & 18.9 dBi	18.3 dBi	97.7 %	0.6 dB
$\theta = 60$ deg $\phi = 90$ deg	17.5 dBi & 17.4 dBi	16.9 dBi	97.7 %	2.0 dB
$\theta = 45$ deg $\phi = 45$ deg	18.8 dBi & 18.7 dBi	18.3 dBi	97.7 %	0.6 dB

C. Discussion

The proposed RA antenna has some potential application scenarios. First, the proposed RA antenna can provide a fixed beam in any direction, it, therefore, can be served as an antenna with a beam pointing to a prescribed and desired direction. Sometimes, the 2-D beam-steerable capabilities are required but the speed for beam switching is not instant, the proposed RA antenna is a good solution as thoroughly demonstrated in the sections above. For a high-speed beam switching application scenario, the proposed RA antenna is still applicable, where some mini-motors [33] with suitable footprints can be employed to electrically control the rotations of the UCs individually to achieve high-speed manipulations on the main beam directions. The controls of these mini-motors are usually performed by a Field Programmable Gate Array (FPGA) system [20], [21].

We have evaluated the costs of our proposed RA antenna with the

previously-reported printed beam-steerable RA antennas by loading PIN diodes. First, the price of metal is relatively cheaper than that of a good quality substrate (Rogers type), and metal is much more available than Rogers type substrates. Second, the price of a PIN diode at the Ka-band is a little expensive than a motor. Most importantly, the PIN diodes seem impossible to be reused again when they are taken off from PCB boards. In contrast, the motors served as control tools can be reused many times. Third, for PIN diodes loaded beam-steerable RA antennas, the configuration of such antenna is multilayer structure (at least two substrate layers) since extra substrate layers are needed to deploy the DC feeding networks. Sometimes, shorting vias should be drilled within multiple substrate layers for a perfect grounding. The multilayer and shorting vias within multiple substrate layers fabrications are all increasing the costs of such antennas. Considering the prices of PIN diodes, substrates, mini-motors, fabrication costs, reuse possibilities, our proposed RA antenna is relatively low-cost and can be produced massively.

IV Conclusion

In summary, a low-cost, high-efficiency and full-metal reflectarray (RA) antenna with mechanically 2-D beam-steerable capabilities is described in this paper. The UC to construct the RA antenna is implemented by a full-metal structure with a cuboid-shaped notch to provide a 1-bit reflection phase for TE and TM normal incidence waves. By adjusting the rotations of UCs manually, the main beam direction of the RA antenna can be easily manipulated on purpose. For demonstration, the main beam at six different directions is presented and measured to validate the concept and effectiveness of the proposed RA antenna for 2-D beam-steerable capabilities. The measured and simulated results on reflection coefficients, radiation patterns, and realized gains are highly consistent. Due to the low-cost, high-efficiency, and high-power handling properties, the proposed RA antenna is a good candidate for 5G millimeter-wave communication applications to provide a fixed or scanning beam.

Acknowledgement

The authors would like to thank the lab engineers, Ben Krøyer and Jesper Dejgaard Meyer for the fruitful discussions on the antenna assembling, Kim Olesen for his kind help with the measurement setup. P. Mei would like to thank Mr. P. Liu from the APMS section at Aalborg University for his warm assistance in processing the data. Also, the valuable comments from the

reviewers and the associate editor are highly appreciated to improve the quality of the manuscript.

References

- [1] Miura, Y. Fujino, S. Taira, N. Obara, M. Tanaka, T. Ojima, and K. Sakauchi, "S-band active phased array antenna with analog phase shifters using double-balanced mixers for mobile SATCOM vehicles," *IEEE Transactions on Antennas and Propagation*, vol. 53, no. 8, pp. 2533-2541, Aug 2005.
- [2] Patterson, et al., "A lightweight organic X-band active receiving phased array with integrated SiGe amplifier and phase shifters," *IEEE Transactions on Antennas and Propagation*, vol. 59, no. 1, pp. 100-109, Jan 2011.
- [3] M. Abdalla, K. Phang, and G. Eleftheriades, "A planar electronically steerable patch array using tunable PRI/NRI phase shifters," *IEEE Transactions on Microwave and Theory Technique*, vol. 57, no. 3, pp.531-541, March 2009.
- [4] H. Chou, T. Hsiao, and J. Chou, "Active phased array of cavity-backed slot antenna with modified feeding structure for the applications of direction-of-arrival estimation," *IEEE Transactions on Antennas and Propagation*, vol. 66, no. 5, pp. 2667-2672, May 2018.
- [5] X. Ding, B. Wang, and G. He, "Research on millimeter-wave phased array with wide-angle scanning performance," *IEEE Transactions on Antennas and Propagation*, vol. 61, no. 10, pp. 5319-5324, Oct 2013.
- [6] J. Doane, K. Sertel, and J. Volakis, "A wideband, wide scanning tightly coupled dipole array with integrated balun (TCDA-IB)," *IEEE Transactions on Antennas and Propagation*, vol. 61, no. 9, pp. 4538-4548, Sep 2013.
- [7] Y. Cao, L. Chin, W. Che, W. Yang, and E. Li, "A compact 38 GHz multibeam antenna array with multifolded bulter matrix for 5G applications," *IEEE Antennas and Wireless Propagation Letters*, vol. 16, pp. 2996-2999, 2017.
- [8] W. Yang, Y. Yang, W. Che, C. Fan, and Q. Xue, "94-GHz compact 2-D multibeam LTCC antenna based on multifolded SIW beam-

- forming network,” *IEEE Transactions on Antennas and Propagation*, vol. 65, no. 8, pp. 4328-4333, Aug 2017.
- [9] R. Gong, Y. Ban, J. Lian, Y. Liu, and Z. Nie, “Circularly polarized multibeam antenna array of ME dipole fed by 5*6 bulter matrix,” *IEEE Antennas and Wireless Propagation Letters*, vol. 18, no. 4, pp. 712-717, Apr 2019.
 - [10] W. Moulder, W. Khalil, and J. Volakis, “60-GHz two-dimensionally scanning array employing wideband planar switched beam network,” *IEEE Antennas and Wireless Propagation Letters*, vol. 9, pp. 818-821, 2010.
 - [11] Y. Li, J. Wang, and K. M. Luk, “Millimeter-wave multibeam aperture-coupled magnetoelectric dipole array with planar substrate integrated beamforming network for 5G applications,” *IEEE Transactions on Antennas and Propagation*, vol. 65, no. 12, pp. 6422-6431, Dec. 2017.
 - [12] Mohamed, and A. Sebak, “60 GHz 2-D scanning multibeam cavity-backed patch array fed by compact SIW beamforming,” *IEEE Transactions on Antennas and Propagation*, vol. 67, no. 4, pp. 2320-2331, Apr. 2019.
 - [13] J. Lian, Y. Ban, Q. Yang, B. Fu, Z. Yu, and L. Sun, “Planar millimeter-wave 2-D beam-scanning multibeam array antenna fed by compact SIW beam-forming network,” *IEEE Transactions on Antennas and Propagation*, vol. 66, no. 3, pp. 1299-1310, March 2018.
 - [14] H. Kamoda, T. Iwasaki, J. Tsumochi, T. Kuki, and O. Hashimoto, “60- GHz electronically reconfigurable large reflectarray using single-bit phase shifter,” *IEEE Transactions on Antennas and Propagation*, vol. 59, no. 7, pp. 2524-2531, July 2011.
 - [15] H. Yang, F. Yang, S. Xu, Y. Mao, M. Li, X. Cao, and J. Gao, “A 1-bit 10*10 reconfigurable reflectarray antenna: design, optimization, and experiment,” *IEEE Transactions on Antennas and Propagation*, vol. 64, no. 6, pp. 2246-2254, Jun. 2016.
 - [16] Carrasco, M. Barba, and J. Encinar, “X-band reflectarray antenna with switching-beam using PIN diodes and gathered elements,” *IEEE Transactions on Antennas and Propagation*, vol. 64, no. 6, pp. 2246-2254, Jun. 2016.

- [17] M. Zhang, *et al.*, “Design of novel reconfigurable reflectarrays with single-bit phase resolution for Ku-band satellite antenna applications,” *IEEE Transactions on Antennas and Propagation*, vol. 64, no. 5, pp. 1634-1641, May. 2016.
- [18] H. Zhang, X. Chen, Z. Wang, Y. Ge, and J. Pu, “A 1-bit electronically reconfigurable reflectarray antenna in X-band,” *IEEE Access*, vol. 7, pp.66567-66576, 2019.
- [19] T. Debogovic, and J. Perruisseau-Carrier, “Low loss MEMS-reconfigurable 1-bit reflectarray cell with dual-linear polarization,” *IEEE Transactions on Antennas and Propagation*, vol. 62, no. 10, pp. 5055-5060, Oct. 2014.
- [20] J. Han, L. Li, G. Liu, Z. Wu, and Y. Shi, “A wideband 1 bit 12 *12 reconfigurable beam-scanning reflectarray: design, fabrication, and measurement,” *IEEE Antennas and Wireless Propagation Letters*, vol. 18, no. 6, pp. 1268-1272, Jun. 2019.
- [21] X. Yang, S. Xu, F. Yang, M. Li, Y. Hou, S. Jiang, and L. Liu, “A broadband high-efficiency reconfigurable reflectarray antenna using mechanically rotational elements,” *IEEE Transactions on Antennas and Propagation*, vol. 65, no. 8, pp. 3959-3966, Aug. 2017.
- [22] H. Luyen, Z. Yang, M. Gao, J. H. Booske, and N. Behdad, “A wideband, single-layer reflectarray exploiting a polarization rotating unit cell,” *IEEE Transactions on Antennas and Propagation*, vol. 67, no. 2, pp. 872-883, Feb 2019.
- [23] H. Luyen, Z. Zhang, J. Booske, and N. Behdad, “Wideband, beam-steerable reflectarrays based on minimum-switch topology, polarization-rotation unit cells,” *IEEE Access*, vol. 7, pp. 36568-36578, 2019.
- [24] M. Afzal, and K. Esselle, “Steering the beam of medium-to-high gain antennas using near-field phase transformation,” *IEEE Transactions on Antennas and Propagation*, vol. 65, no. 4, pp. 1680-1690, Apr 2017.
- [25] W. Hong, *et al.*, “Multibeam antenna technologies for 5G wireless communications,” *IEEE Transactions on Antennas and Propagation*, vol. 65, no. 2, pp. 6231-6249, Dec 2017.
- [26] T. Rappaport, *et al.*, “Millimeter-wave mobile communications for

- 5G cellular: it will work,” *IEEE Access*, vol. 1, pp. 335-349, 2013.
- [27] <https://www.everythingrf.com/products/waveguide-horn-antennas/pasternack-enterprises-inc/617-20-pe9851-2f-10>
- [28] P. Mei, S. Zhang, Y. Cai, X. Q. Lin, and G. F. Pedersen, “A reflectarray antenna designed with gain filtering and low-RCS properties,” *IEEE Transactions on Antennas and Propagation*, vol. 67, no. 8, pp. 5362-5371, Aug 2019.
- [29] P. Nayeri, M. Liang, R. A. Sabory-Garcia, M. Tuo, F. Yang, H. Xin, and A. Elsherbeni, “3D printed dielectric reflectarrays: low-cost high gain antennas at sub-millimeter waves,” *IEEE Transactions on Antennas and Propagation*, vol. 62, no. 4, pp. 2000-2008, Apr 2014.
- [30] R. Deng, Y. Mao, S. Xu, and F. Yang, “A single-layer dual-band circularly polarized reflectarray with high aperture efficiency,” *IEEE Transactions on Antennas and Propagation*, vol. 63, no. 7, pp. 3317-3320, July 2015.
- [31] Yu, F. Yang, A. Elsherbeni, J. Huang, and Y. Rahamt-Samii, “Aperture efficiency analysis of reflectarray antennas,” *Microwave and Optical Technology Letters*, vol. 52, no. 3, pp. 771-779, Mar. 2004.
- [32] H. Yang, F. Yang, S. Xu, M. Li, X. Cao, J. Gao, and Y. Zheng, “A study of phase quantization effects for reconfigurable reflectarray antennas,” *IEEE Antennas and Wireless Propagation Letters*, vol. 16, pp. 302-305, 2017.
- [33] <https://www.vibrationmotors.com/>

Paper D

A Dual-Polarized and High-Gain X-/Ka-Band Shared-Aperture Antenna with High Aperture Reuse Efficiency

Peng Mei, Shuai Zhang, Gert Frølund Pedersen

This paper has been published at the
IEEE Transactions on Antennas and Propagation, vol. 69, no. 3, pp. 1334
-1344, Mar 2021.

© 2021 IEEE

The layout has been revised and reprinted with permission.

Abstract

This paper describes a dual-polarized and high-gain shared-aperture antenna operating in X and Ka-band. The proposed shared-aperture antenna is implemented by combining a folded transmitarray (TA) antenna operating in Ka-band and a Fabry-Perot (FP) cavity antenna operating in X-band together. In this configuration, the shared aperture serves as a phase-shifting surface for the TA antenna, and as a partially reflective surface for the FP antenna simultaneously. Since both of the two antennas radiate into free space through the same physical aperture, the aperture reuse efficiency of the proposed shared-aperture antenna is 100%. A four-layered, metallic double-ring structure is selected as the unit cell (UC) to implement the shared aperture to fulfill the aforementioned requirements. It is found that the frequency responses of the UC in X- and Ka-band are highly independent, which can be controlled separately to facilitate the antenna design and optimization. Two dual-polarized patch antennas operating in X and Ka-bands are utilized to enable a dual-polarized manner of the proposed shared-aperture antenna. The simulated results reveal that the proposed shared-aperture antenna has -10-dB bandwidth of 9.8-10.2 GHz and 26.5-29.0 GHz with the realized gain of 14.8 dBi (at 10 GHz) and 24.4 dBi (at 28 GHz) in two polarizations. All the simulations are experimentally verified.

I Introduction

Shared-aperture antennas are emerging antennas, attracting lots of attention and interests recently due to their unique advantages of dual-band/multi-band, compact size, low cost, low mass, high space utilization efficiency, etc [1]-[13], which can be potentially deployed and applied in synthetic aperture radar (SAR) [3], [7]-[9], satellite communications [11], and base station communications [12]. The shared-aperture antenna, by its name, is a kind of antenna that is usually composed of several antennas operating in different frequency bands together, where these antennas radiate into free space efficiently by sharing a partial or entire aperture. To this end, the keys to designing a shared-aperture antenna are to find out proper types of antennas and integrating them in an efficient architecture, where the properties of these antennas usually determine the performance of the established shared-aperture antenna to some extent. There are some design considerations for a shared-aperture antenna: a). Polarization. Dual- polarization is preferred since it can provide polarization diversity and increase the traffic handling capacity of a system; b). Frequency ratio (FR), which is defined by the ratio of the highest

and lowest frequency of a shared-aperture antenna. A large FR is reasonable, otherwise, a wideband antenna such as a wideband ridge horn antenna can replace a shared-aperture antenna in function; c). Aperture reuse efficiency, defined by the ratio of the actual radiation aperture areas of a shared- aperture antenna in different frequency bands. It should be emphasized here that when defining the aperture reuse efficiency, the shared aperture is essential for all sub antennas of a shared-aperture antenna.

A slot and slot arrays are one kind of the popular sub antennas to form a shared-aperture antenna [1]-[5]. In [1], the authors reported a shared-aperture antenna operating in *S/K*-band. In this design, the *S/K*-band sub antennas were in the same layer, where the slot operating at *S*-band was embedded within the *K*-band slot arrays. A metasurface located above the sub antennas was served as the radiator of the *S*-band antenna but was transparent to the *K*-band antenna. A *L/X*-band shared- aperture antenna was formed by etching crossed slots and the slot arrays on the surface of a metal cavity in an interleaved configuration [3], where the *L/X*-band slot arrays radiate through different areas within the same aperture. The main drawbacks of such shared-aperture antennas based on slot and slot arrays (e.g., [1]-[5]) are single-polarization and a SIW- based feeding network is needed for high frequency to achieve high gain.

Patch antennas (or arrays) combining with feeding networks are another technique to design shared-aperture antenna with dual polarizations [6]-[10]. A triple-band shared-aperture antenna was reported in [9], where the authors employed patches with different sizes for *X/Ku/Ka*-band radiations. To excite the *X/Ku/Ka*-band patches in a dual-polarized manner, three complicated feeding networks are designed and configured in different layers, which would be lossy in the high frequency. Such dual-polarized shared-aperture antennas (e.g., [6]-[10]) are achieved at the expense of lossy and complicated feeding networks.

Referring to the definition of aperture reuse efficiency, a shared-aperture antenna with an aperture reuse efficiency of 0.77 was reported in [5], where the authors served the radiating patch of a patch antenna operating at 3.5 GHz as the metal ground for the 60 GHz slot array antenna. A dual-band reflectarray in [11] achieved a perfect aperture reuse efficiency, where the unit cells are served as the phase-shifting elements in *X*- and *Ka*-band simultaneously. However, the dual-band reflectarray antenna suffers from the bulky volume (high profile) and high dependence of the two bands.

In this paper, a dual-polarized and high-gain *X/Ka*-band shared-aperture antenna is proposed with a high aperture reuse efficiency of 100%. The proposed shared-aperture antenna has a low profile and is formed by a folded transmitarray (TA) antenna in *Ka*-band and a Fabry-Perot (FP) antenna in *X*-band since both of the antennas have the similar geometries. To this end, it is required that the shared aperture should not only be served as phase-shifting surfaces for the TA antenna but also as a partial reflectance/transmission surface for the FP antenna. As a result, both of the antennas radiate into free space through the physically same aperture, leading to a perfect aperture reuse efficiency. A four-layered, metallic double-ring structure is proposed as the unit cell (UC) to perform the shared aperture to fulfill the aforementioned requirements. The simulated results indicate the UC offers the phase-shifting abilities in *Ka*-band and partial reflectance/transmission in *X*-band simultaneously. Moreover, the frequency responses of the UC in *X*- and *Ka*-band can be controlled independently. Two dual-polarized patch antennas with very simple geometries, operating in *X*- and *Ka*-band, are designed to achieve the dual-polarization of the proposed shared-aperture antenna. The measured results reveal the -10 dB bandwidth of 26.7- 29.4 GHz and 9.75-10.2 GHz with the average isolation of around 15 dB and 30 dB between two polarizations, respectively. A realized gain of 13.8 dBi at 10 GHz and 23.6 dBi at 28 GHz of the proposed shared-aperture antenna are experimentally obtained as well. Besides, the performance of the shared- aperture design in two polarizations is highly consistent based on the measurements.

Compared with the existing work [1]-[11], it is obvious to conclude the contributions and advantages of the proposed shared-aperture antenna:

- a). By fully taking advantage of working mechanisms and geometries of the folded TA antenna and FP antenna, both of the antennas radiate into free space through the same physical aperture, leading to a perfect aperture reuse efficiency of 100%;
- b). Without any complicated feeding networks, it is very easy to achieve high gains and dual-polarization while keeping a relatively low profile;

The outlines of the paper are organized as follows: Section II explains the concept of the proposed shared-aperture antenna; the desired UC is analyzed and its frequency responses are fully elaborated in section III; the implementations of the proposed shared-aperture antenna operating in *X* and *Ka*-band are presented in Section IV; the proposed shared- aperture antenna is fabricated and measured, which is also compared with the simulated results in Section V. Some remarkable conclusions are drawn in Section VI.

II Concept

An evolutionary diagram is presented to explain the concept of the proposed shared-aperture antenna. Fig. D. 1(a) is the configuration of a folded TA antenna. It consists of a metal plate, phase-shifting surfaces, and a feeding source, where the feeding source and the phase-shifting surfaces are located on the same plane. A focused beam at broadside would be achieved when the electromagnetic waves radiating from the feeding source propagate through the phase-shifting surfaces. In contrast, Fig. D. 1(b) shows the configuration of a FP resonant antenna, where a partially reflective surface is placed above a feeding source with a certain separation. Electromagnetic waves radiating from the feeding source would experience multiple reflections between the PRS and metal ground, where the separation between them is decided to make the electric fields at the aperture of PRS in-phase so that a high gain can be achieved.

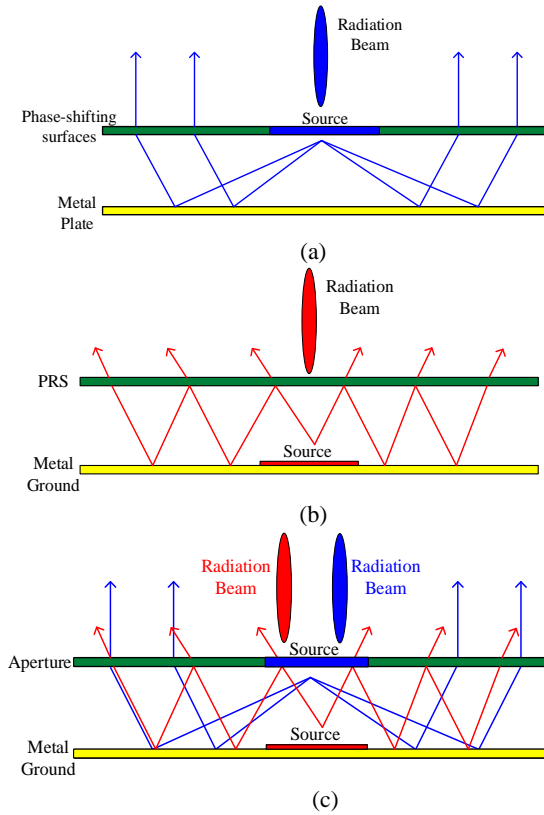


Fig. D. 1. Evolutions of the proposed shared-aperture antenna. The configurations of (a) a folded transmitarray antenna, (b) a Fabry-Perot antenna, and (c) the proposed shared-aperture antenna.

From Fig. D. 1(a) and (b), it is observed that the geometries and configurations of the folded TA antenna and the FP antenna are very similar to each other, which both of the two antennas include a feeding source, a metal ground and a superstrate located above a metal ground with a separation. To this end, it inspires one to combine the two antennas to realize a shared-aperture antenna as shown in Fig. D. 1(c), where the folded TA antenna and FP antenna are responsible for radiating in the high- and low-frequency band, respectively. Since both of the folded TA and the FP antennas radiate into free space through the same physical aperture, a 100 % aperture reuse efficiency is obtained for the proposed shared-aperture antenna.

To achieve the proposed shared-aperture antenna, one of the challenges is to find out a proper UC to implement the shared aperture. Specifically speaking, the desired shared aperture is required to be served as a phase-shifting surface with a small attenuation in the high-frequency band for the folded TA antenna and show partially reflective/transmissive properties in the low-frequency band for the FP antenna simultaneously. Moreover, independent controls of the frequency responses of the shared aperture in the low- and high-frequency band are also preferred.

III Unit Cell Design and Analysis

A. Configuration of the unit cell

Fig. D. 2 presents the geometries of the proposed UC. It consists of four identical layers, where the metallic double-ring patterns are printed on each supporting substrate. The supporting substrate is Rogers RO4003C with a thickness of 0.305 mm, a dielectric constant of 3.55, and a loss tangent of 0.0027. Considering that the UC will serve as a phase-shifting element at 28 GHz, the periodicity of the UC (a) and air separation (H) between each layer are 5 mm and 2.5 mm (corresponding to $\lambda/2$ and $\lambda/4$ at 28 GHz approximately), respectively. The dimensions of the metallic double-ring are initially given as follows: $r_4 = 2.25$ mm, $r_3 = 1.75$ mm, $r_2 = 1.05$ mm, and $r_1 = 0.55$ mm. The S-parameter of the UC is simulated and evaluated by using CST Microwave Studio software, where periodic boundary conditions (PBC) are imposed on the UC to emulate an infinite surface. Fig. D. 3 shows the S-parameter of the UC from 5 to 40 GHz with a normal incidence wave. It is found that the UC

can be regarded as a phase-shifting element in the high-frequency band from 24 to 34 GHz, and as a partial reflectance/transmission element in the low-frequency band from 8 to 12 GHz or 13 to 14 GHz, which is a candidate for the desired shared aperture implementation.

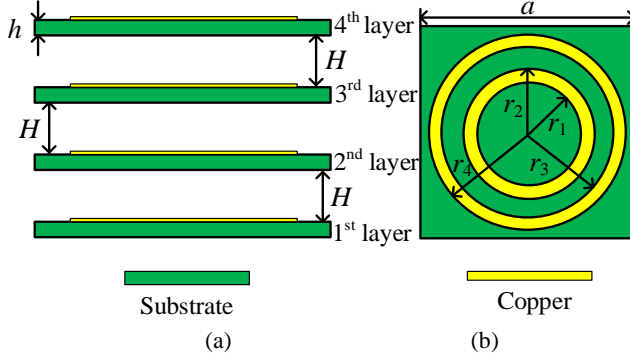


Fig. D. 2. The geometries of the UC. (a). Side view. (b). Front view. ($h = 0.305$ mm, $H = 2.5$ mm, $r_4 = 2.25$ mm, $r_3 = 1.75$ mm, $r_2 - r_1 = 0.5$ mm)

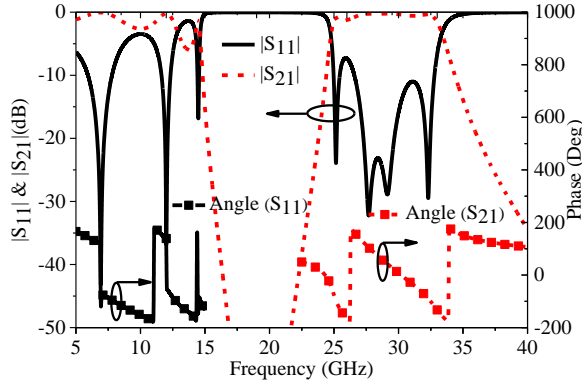


Fig. D. 3. The S-parameter of the UC. ($r_4 = 2.25$ mm, $r_3 = 1.75$ mm, $r_2 = 1.15$ mm, $r_1 = 0.5$ mm)

B. High-frequency analysis

It has been proved that a four-layered, metallic double-ring (square) UC is typically employed as a phase-shifting element for a TA antenna design since it can not only provide a full phase-cycle (2π) but also offer an acceptable attenuation (less than 1dB) [14]. To figure out the working mechanisms of the UC well, a single layer of the UC is investigated from its equivalent circuit and current distributions. Fig. D. 4(a) gives the equivalent circuit of the single-layer double-ring structure, where two shunt LCs caused by the outer and

inner metallic rings are in parallel. It is also known that a shunt LC shows a bandstop frequency response at a specific frequency that is usually calculated by $f = 1/(2\pi\sqrt{LC})$, resulting in a transmission zero in the frequency spectrum. Since the dimensions of the outer and inner metallic rings are different, the frequencies of the two transmission zeros are distinguished accordingly. Between the two transmission zeros, there exists a reflection pole [15], which has been verified by the simulated results. Therefore, it can be sufficiently predicted that the proposed UC can generate four reflection poles since it is formed by cascading four identical layers [15]. The theoretical analysis is highly consistent with the simulated results shown in Fig. D. 3, where four reflection poles are observed in the high-frequency band. The current distributions on the metallic double-ring at the reflection pole are presented in Fig. D. 4(b), where it is observed that currents are mainly concentrated in the outer periphery of the inner ring and inner periphery of the outer ring. The current distributions on the metallic double-ring would be served as a guideline to manipulate the frequency responses of the UC in the low- and high-frequency bands.

Based on the equivalent circuit and current distributions, there are two possible techniques to control the frequency responses of the UC in the high-frequency band: one is to tune the radius of the inner ring with other parameters fixed, and the other is to modify the radius of the outer ring with other parameters fixed. Here, we adopt the former one to manipulate the frequency responses of the UC in the high-frequency band since the outer ring has a relatively large physical dimension that is expected to be employed to control the frequency responses in the low-frequency band. Here, we vary the radius of the inner ring but keep its width. Fig. D. 5 presents the amplitude of S_{11} , reflection phases, and transmission phases of the UC with different values of r_2 . It is observed that the passband is shifting toward higher frequencies when the value of r_2 decreases, while the frequency responses in the low-frequency band (from 5 to 15 GHz) are almost the same.

It is also observed that the transmission phases of the UC vary regularly with a different value of r_2 as shown in Fig. D. 5, which can offer a full phase-cycle (2π) transmission phase coverage. The transmission amplitude and phase of the UC at 28 GHz with different values of r_2 extracted from Fig. D. 5 are plotted to further check its abilities to be served as a phase-shifting element. From Fig. D. 6, it is observed that a full phase-cycle is achieved with an average transmission attenuation of less than 1.0 dB when the value of r_2 varies from 0.85 to 1.40 mm.

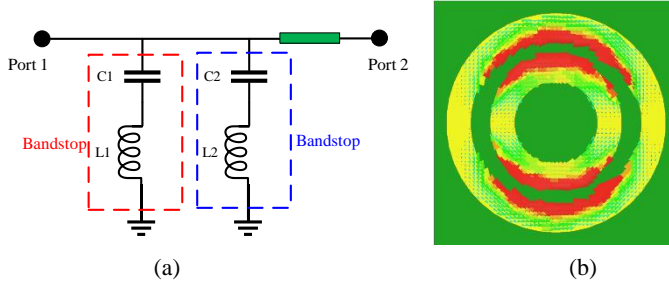


Fig. D. 4. The single layer of the proposed unit cell. (a). Equivalent circuit. (b). Current distributions on the double rings at the reflection pole.

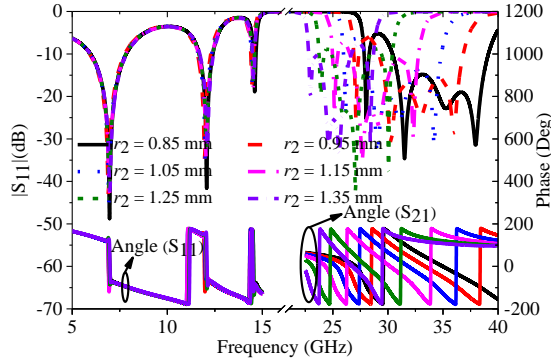


Fig. D. 5. The reflection coefficients of the proposed UC with different values of r_2 . ($h = 0.305$ mm, $H = 2.5$ mm, $r_4 = 2.25$ mm, $r_3 = 1.75$ mm, $r_2 - r_1 = 0.5$ mm)

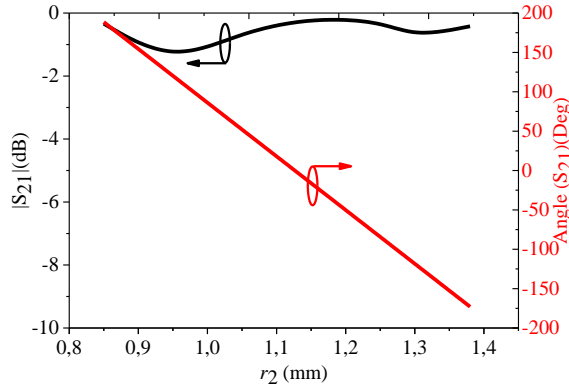


Fig. D. 6. The simulated transmission amplitude and phase of the UC with different values of r_2 at 28 GHz. ($h = 0.305$ mm, $H = 2.5$ mm, $r_4 = 2.25$ mm, $r_3 = 1.75$ mm, $r_2 - r_1 = 0.5$ mm)

C. Low-frequency analysis

As we know, FP antennas are a kind of resonant antennas, composed of a

superstrate generally named PRS and a feeding source. The PRS is typically formed by lots of UCs periodically distributed or pure dielectric substrates [16]-[18]. The main consideration for a PRS is that the transmission/reflection phase and the reflective/transmissive amplitude on any position of it should be the same even if the PRS is not implemented by periodically distributed identical UCs. Then, by calculating the separation between the PRS and the feeding source, it is expecting to make the electric fields on the PRS aperture in-phase to achieve high gain at a certain frequency. In our design, the UCs to construct the PRS are not physically identical since the value of r_2 is required to be varied to fulfill the desired phase compensations for the folded TA antenna in the high-frequency band. However, such non-identical UCs can still work for a PRS implementation since both of the reflective/transmissive amplitudes and transmission/reflection phases remain the same, which will be further presented in the following.

In Fig. D. 5, it is observed that the reflection amplitudes and phases of the UC in the low-frequency band (from 5 to 15 GHz) are extremely stable when the value of r_2 varies from 0.85 to 1.40 mm. It should further check the transmission phases of the UC in the low-frequency band with different values of r_2 . To this end, the reflection amplitude, reflection phase, and transmission phase of the UC at 10 GHz are plotted with different values of r_2 . As seen in Fig. D. 7, the reflection amplitude, reflection phase, and transmission phase of the UC is around -3.5 dB, -151.0 deg, and 130 deg when the value of r_2 varies from 0.75 to 1.45 mm, respectively. The variations of reflection amplitude, reflection phase, and transmission phase are 0.08 dB, 1.6 deg, and 1.0 deg, respectively. The simulated results in Fig. D. 5 and Fig. D. 7 sufficiently indicate the high feasibility of a PRS composed of the designed UCs to implement a FP antenna even though they are not physically identical.

The approaches to control the UC's frequency responses in the low-frequency band are discussed in the following to provide detailed instructions and guidelines for the FP antenna design. Since the dimension of the inner ring has been used to obtain a full phase-cycle in the high-frequency band, we focus on tuning the dimension of the outer ring to adjust the UC low-frequency responses. As seen in Fig. D. 4(b), the currents are mainly concentrated on the inner periphery of the outer ring. We can expect the UC high-frequency responses should be maintained when the values of r_3 , r_1 , and r_2 are fixed, while the values of r_4 can potentially adjust the UC low-frequency responses. Here, we introduce and validate the following two approaches:

a). Varying the values of r_4 of every layer of the UC simultaneously while

keeping the other parameters fixed. As seen in Fig. D. 8, the operating band shifts toward lower frequencies with the increment of r_4 while the high-frequency responses keep almost identical;

b). Only varying the values of r_4 of the second and third layers while keeping the values of r_4 of the first and fourth layers of the UCs and the other parameters fixed. As observed in Fig. D. 9, the operating bandwidth of the UCs in the low-frequency band is broadened with r_4 decreasing, and the frequency responses in the high-frequency band are still nearly the same.

From Fig. D. 5, Fig. D. 8 and Fig. D. 9, it can be concluded that the frequency responses of the UCs in X- and Ka-band are highly independent with each other, and can be controlled separately by adjusting the specific parameters. This is a very important feature to facilitate the shared-aperture antenna design.

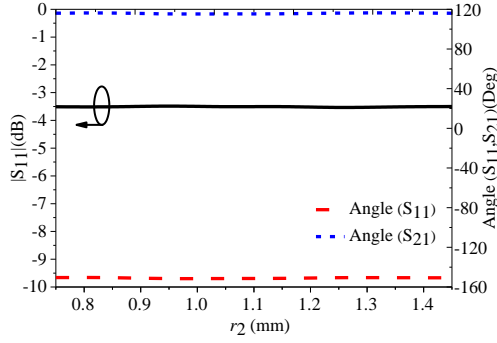


Fig. D. 7. The reflection amplitude, reflection phase and transmission phase of the UC at 10 GHz when the value of r_2 varies from 0.75 to 1.45 mm.

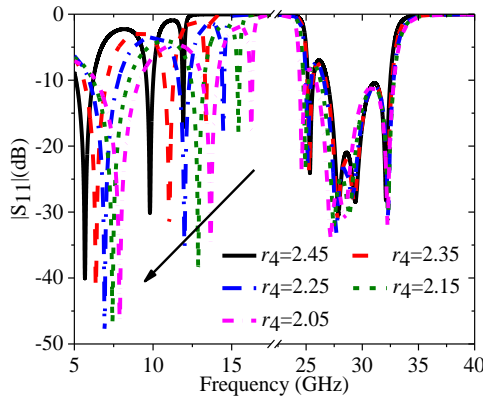


Fig. D. 8. The reflection coefficients of the UC when the value of r_4 varies from 2.05 to 2.45

mm with the other parameters fixed. ($h = 0.305$ mm, $H = 2.5$ mm, $r_3 = 1.75$ mm, $r_2 = 1.05$ mm, $r_1 = 0.55$ mm)

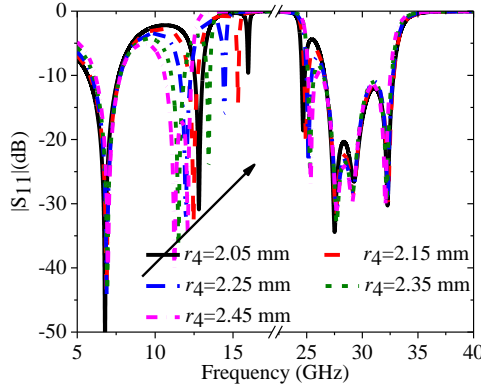


Fig. D. 9. The reflection coefficients of the UC when the value of r_4 varies from 2.05 to 2.45 mm with the other parameters fixed.

IV Shared-Aperture Antenna Implementation

Since the UCs to construct the shared aperture are axially symmetrical, the shared aperture is feasible for dual- and circularly-polarized applications when the feeding sources of the shared-aperture antenna is dual- or circularly-polarized. In this section, a dual-polarized shared-aperture antenna is mainly investigated and presented. Two dual-polarized feeding sources are utilized for the proposed shared-aperture antenna to realize dual-polarization. According to the configurations shown in Fig. D. 1, the feeding source operating at 28 GHz would be integrated with the shared aperture. Since the shared aperture is a four-layered structure, there are three possible solutions to deploy the feeding source operating at 28 GHz as shown in Fig. D. 10. The feeding source can be located at either the first or the fourth layer of the shared aperture. It should be noted that the air separation between the first layer and the metal ground is determined by the FP antenna operating in the low-frequency band, which is chosen to make the electric fields on the shared aperture in-phase to realize a high gain. If the distance is small, it would affect the reflection coefficient of the proposed shared- aperture in the high-frequency band. On the other hand, the feeding source operating at 28 GHz is fed with our available MMPX connectors [as shown in Fig. D. 11(c)] that have large footprints, resulting in the difficult assembling with the shared aperture if the feeding source is mounted on the first layer.

Alternatively, the feeding source can be located at the fourth layer as shown

in Fig. D. 10(b). In this configuration, there is much space for MMPX connectors assembling. However, it suffers from a disadvantage that the remaining three layers (1st, 2nd, 3rd layer) would affect the radiation patterns of the feeding source and the perturbations are difficult to predict and evaluate, leading to some effects on the final radiation performance of the shared-aperture antenna in the high-frequency band. To solve this problem, a metal cavity is mounted to shield the feeding source from electromagnetic interferences with the remaining three layers as shown in Fig. D. 10(c). Furthermore, the metal cavity can constrain the electromagnetic fields and make the radiation patterns of the feeding source more symmetrical.

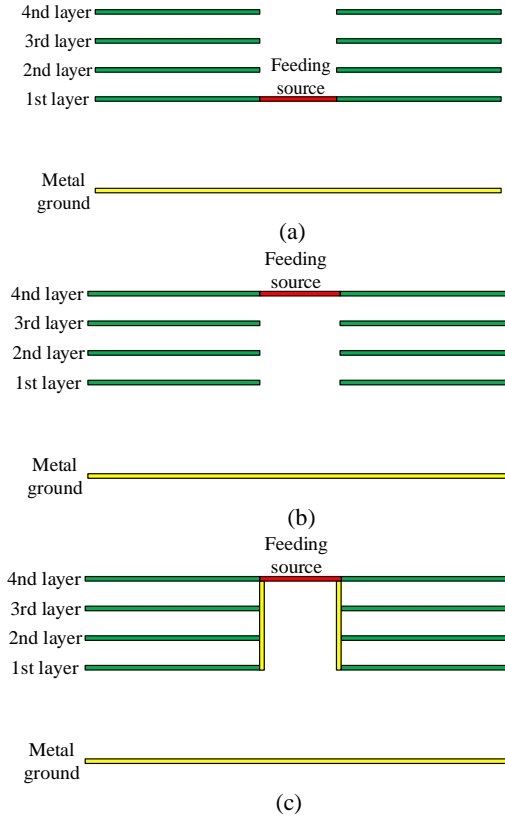
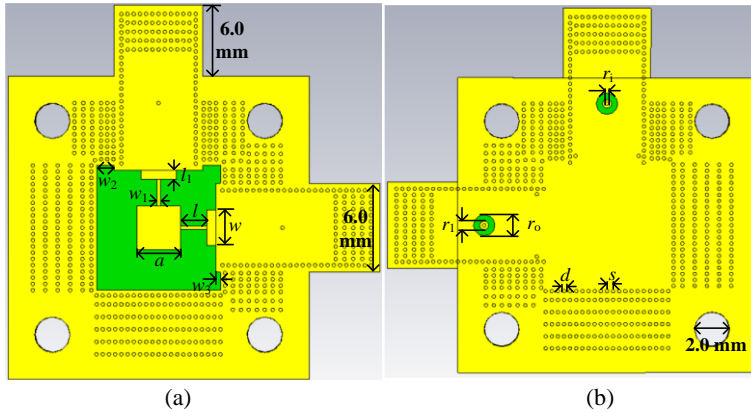


Fig. D. 10. Three solutions to place the feeding sources in the shared aperture. The feeding source is located at: (a) the first layer, (b) the fourth layer without a metal cavity, and (c) the fourth layer with a metal cavity.

A. Dual-polarized SIW-based patch antenna at 28GHz

The geometries of the dual-polarized SIW-based patch antenna are shown in Fig. D. 11. The substrate used here is also Rogers RO4003C with a dielectric constant of 3.55, and a loss tangent of 0.0027. To obtain a wider bandwidth, a thickness of 0.813 mm is adopted. The shape of the radiating patch is selected as a square to make the resonant frequencies the same in two polarizations. To excite the square patch antenna efficiently, a SIW to microstrip line transition and a quarter- wavelength impedance transformer are introduced. A coaxial to SIW transition is also adopted to feed the SIW cavity. The dimensions of the square patch are modified to make it resonant at 28 GHz. The height of the metal cavity exactly fits the total thickness of the shared aperture as shown in Fig. D. 11(d). Fig. D. 12(a) shows the S-parameter of the dual-polarized SIW-based patch antenna, where -10-dB bandwidth from 26.9 to 29.4 GHz with an absolute bandwidth of 2.5 GHz is observed. The isolation between the two ports is better than 15 dB at 28 GHz.

The radiation patterns of the dual-polarized SIW-based patch antenna are simulated at 28 GHz. As seen in Fig. D. 12(b), -10-dB gain edge tapers in E- and H-plane are very close, leading to a beamwidth of 150 and 137 degrees, respectively. Even though the 10 dB beamwidths in E- and H-plane are not completely identical, they are feasible as a feeding source for a folded transmitarray antenna. The simulated peak realized gain is 7.74 dBi at 28 GHz. Besides, 10-dB beamwidths of the dual-polarized SIW-based patch antenna are also checked from 26.5 to 29.5 GHz, which are 143-153 degrees and 136-140 degrees in E- and H-plane, respectively.



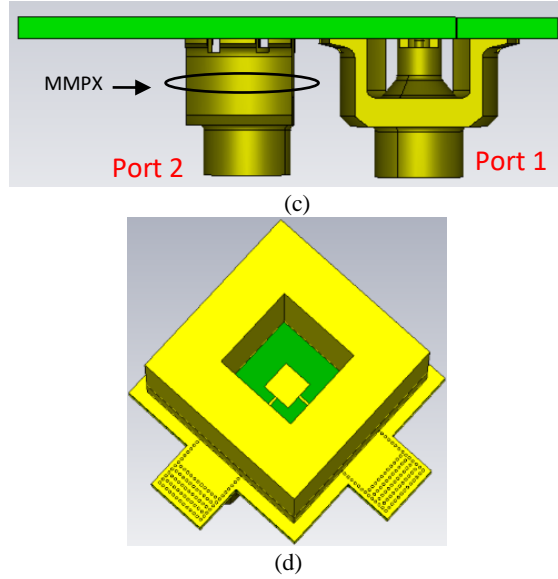


Fig. D. 11. The geometries of the dual-polarized SIW-based antenna. (a). Front view. (b). Back view. (c). Side view. (d). Perspective view with a metal cavity.

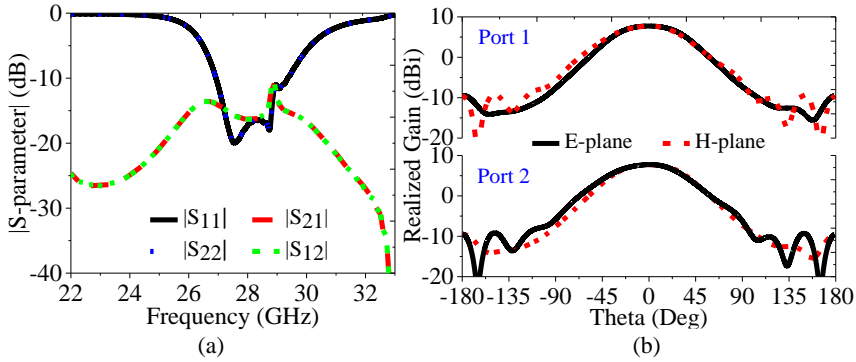


Fig. D. 12. (a). S-parameter of the dual-polarized SIW-based patch antenna. (b). The simulated co-polarizations of the dual-polarized SIW-based patch antenna at 28 GHz with port 1 and 2 excited, respectively.

B. Dual-polarized patch antenna at 10GHz

The geometries of the dual-polarized patch antenna at 10 GHz are shown in Fig. D. 13. The side feeding technique is adopted to feed the square patch for convenient measurements. Likewise, a quarter-wavelength impedance transformer is also used to achieve a good impedance match. The dimensions of the square patch are roughly determined to make it resonant around 10 GHz

since the final reflection coefficient would be slightly different with the counterpart of a single dual-polarized patch antenna when it is served as a feeding source for the proposed shared-aperture antenna in the low-frequency band because a superstrate (the shared aperture) is located above the patch antenna with a certain separation.

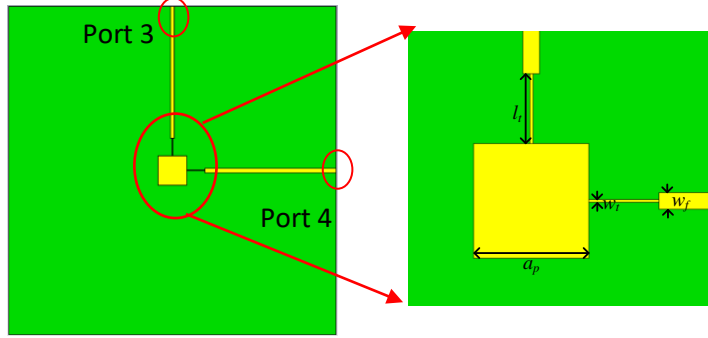


Fig. D. 13. Geometries of the dual-polarized patch antenna at 10 GHz.

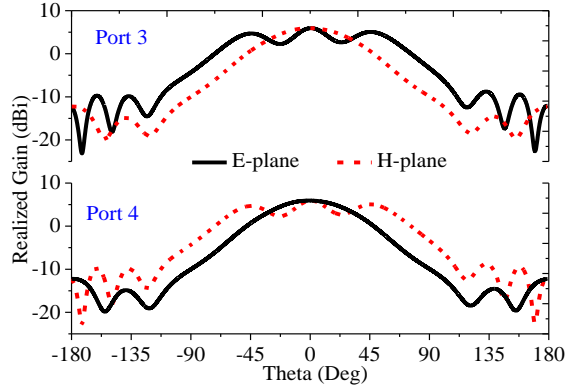


Fig. D. 14. Simulated co-polarizations of the dual-polarized patch antenna at 10GHz with ports 3 and 4 excited, respectively.

The simulated radiation patterns of the dual-polarized patch antennas are also presented at 10 GHz. Here, we choose the dimension of the metal ground consistent with the size of the shared aperture. It is observed in Fig. D. 14 that the radiation pattern in E-plane is not as good as the counterpart in H-plane at 10 GHz since the relatively large size of a metal ground usually affects the radiation patterns of a patch antenna as thoroughly investigated in [19], [20]. The simulated peak realized gain of the dual-polarized patch antenna is 5.9 dBi at 10 GHz. The radiation patterns are also checked at frequencies of 9.75

and 10.25 GHz. The simulated results indicate radiation patterns of the dual-polarized antenna at frequencies of 9.75 and 10.25 GHz highly consistent with that at 10 GHz. Since the dual-polarized patch antenna is served as a feeding source for the proposed shared-aperture antenna in the low-frequency band. Even though the radiation patterns in E-plane are not ideal, the final radiation patterns of the proposed shared-aperture antenna are improved significantly at 10 GHz, which will be presented in the next subsection.

C. Implementation of the proposed shared-aperture antenna

The proposed shared-aperture antenna is constructed with the proposed UCs and two dual-polarized feeding sources. The size of the shared aperture is 85 mm × 85 mm, corresponding to 17 × 17 UCs in x- and y-directions. Firstly, the air separation between the metal ground and first layer of the shared aperture is determined by the following equation [21]:

$$-2\frac{2\pi}{\lambda}h - \varphi_{PRS} - \varphi_{Ground} = 2n\pi, n = 0, \pm 1, \pm 2, \pm 3, \dots \quad (1)$$

where φ_{PRS} and φ_{Ground} are the reflection phases of the shared aperture and the metal ground at 10 GHz, respectively. Based on the reflection phase of the UC at 10 GHz, it is calculated that the air separation h equals to 17.0 mm.

Once the air separation is determined, the phase compensation plane for the folded TA antenna is also decided accordingly. It should be mentioned here that the far-field zones of the two feeding sources at 10 and 28 GHz are calculated according to the equation of $d = 2D^2/\lambda$, where D is the length or diameter of an antenna, λ is the wavelength. It is found that the far-field distances of the two feeding sources at 10 and 28 GHz are 7.6 and 2.24 mm, respectively. According to the calculated air separation of 17.0 mm, the shared aperture is located at the far-field zone of both the two feeding sources. Therefore, it is reasonable to only consider the radiation patterns (far-field) of the two feeding sources shown in Figs. D. 12 and D. 14.

Due to the slightly structural asymmetry of the dual-polarized feeding source at 28 GHz shown in Fig. D. 11 (radiation patterns in E- and H-plane are not completely identical), it can be reasonably predicted that the phase distributions on the phase compensation plane should be slightly different when port 1 or port 2 is excited, respectively. On the other hand, it should be noted that each single UC cannot provide two different transmission phases simultaneously. To this end, the final phase distributions are calculated by

averaging the transmission phases as follows:

$$\varphi_{Final} = \frac{\varphi_1(i, j) + \varphi_2(i, j)}{2} \quad (2)$$

where $\varphi_1(i, j)$ and $\varphi_2(i, j)$ are transmission phases at the same UC with a position of (i, j) when port 1 and port 2 are excited, respectively. The adoption of the average value of the two transmission phases can minimize the difference of realized gain of the shared-aperture antenna in two polarizations. Fig. D. 15 plots the final phase distributions on the phase compensation plane. Based on the phase distributions, the final shared aperture is established with the proposed UCs according to the relation shown in Fig. D. 6.

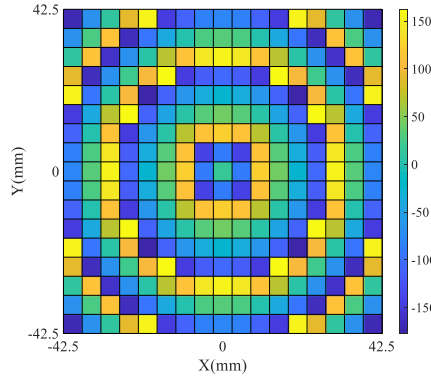
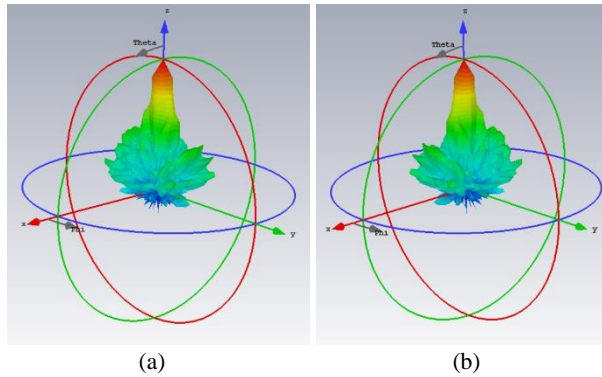


Fig. D. 15. The final phase distributions on the phase compensation plane at 28 GHz.



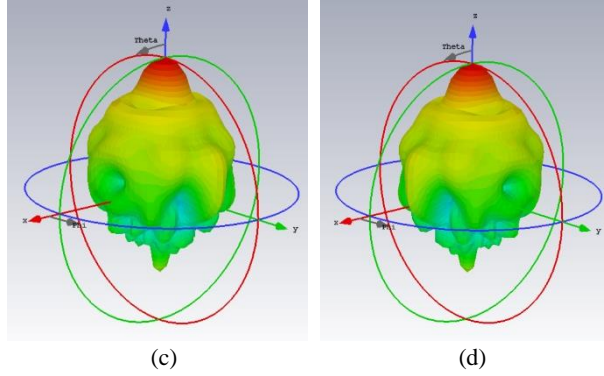
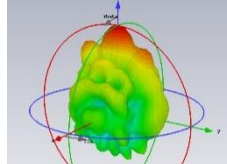


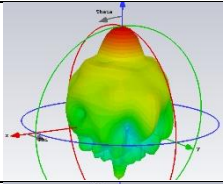
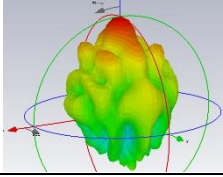
Fig. D. 16. The simulated 3D radiation patterns of the proposed shared-aperture antenna when different ports are excited at 10 GHz. (a). Port 1 is excited. (b). Port 2 is excited. (c). Port 3 is excited. (d). Port 4 is excited.

The radiation patterns of the proposed shared-aperture antenna are simulated and evaluated at 10 GHz and 28 GHz, respectively. When one port is excited, the remaining ports are all terminated with matching loads. As shown in Fig. D. 16, the realized gain is 14.8 dBi at broadside when port 3 or 4 is excited at 10 GHz. At 28 GHz, the boresight realized gains are 24.4 dBi when port 1 or 2 is excited.

For a FP antenna, the gain is mainly associated with the reflective/transmissive amplitude and the aperture size of the PRS [21]. As stated in section III, the reflective/transmissive amplitude of the UC can be controlled independently in the low-frequency band. Here, the realized gains of the proposed shared-aperture antenna at 10 GHz are compared with three different reflective/transmissive amplitudes of the PRS as tabulated in Table. D. I. It is observed that when the reflective amplitude is -3.50 dB, the proposed shared-aperture antenna has an optimal radiation pattern under a fixed shared aperture size (85 mm×85 mm), and also has the smallest air separation at 10 GHz.

Table D. I. Radiation performance comparisons of the proposed shared-aperture antenna with three different reflection/transmission amplitudes of the shared-aperture.

	R-A (dB)	R-P (Deg)	A-S (mm)	R-G (dBi)	3D radiation pattern at 10 GHz
#1	-1.4	-103.4	17.0	14.9	

#2	-3.5	-150.9	16.2	14.8	
#3	-5.94	-94	18.6	13.7	

R-A: reflection amplitude; R-P: reflection phase; A-S: air separation; R-G: realized gain.

Table. D. II. The dimension of the proposed shared-aperture antenna. (Unit: mm)

a	l	l_1	w	w_1	w_2	w_3	r_i
2.45	1.5	0.5	2.0	0.2	1.0	0.275	0.4
r_o	r_1	d	s	a_p	w_t	l_t	w_f
1.23	0.5	0.2	0.35	7.56	0.2	4.6	1.1

V Measuement and Discussion

In this section, the proposed shared-aperture antenna has been fabricated with the dimensions as listed in Table. D. II and measured. Fig. D. 17 gives photographs of dual-polarized antennas, the proposed shared-aperture antenna, and its different parts. All boards are produced with printed circuit board (PCB) technologies. There are 8 air holes with diameters of 3 mm uniformly distributed in the edges of every board for alignments. To support four-layered phase-shifting surfaces, some lightweight foams with relative permittivity of approximately 1.00 and required thicknesses are inserted between adjacent layers to make layers parallel with each other. It has been verified from the simulated results that the performance of the proposed shared-aperture antenna is still maintained when the relative permittivity of the foam is varied from 1.00 to 1.10 with an interval of 0.05 or the exact separation between layers is slightly bigger or smaller than the required one. The metal cavity is produced with CNC (computer numerical control) milling technologies [22]. Because the thickness of the substrate of the dual-polarized patch antenna at 10 GHz is only 0.508 mm, a metal plate with a thickness of 5 mm is also produced with mechanical milling technologies to be attached underneath the dual-polarized patch antenna at 10 GHz for supporting. The separation between the shared aperture and the dual-polarized patch antenna at 10 GHz is fixed with some metallic pillars with certain thicknesses.

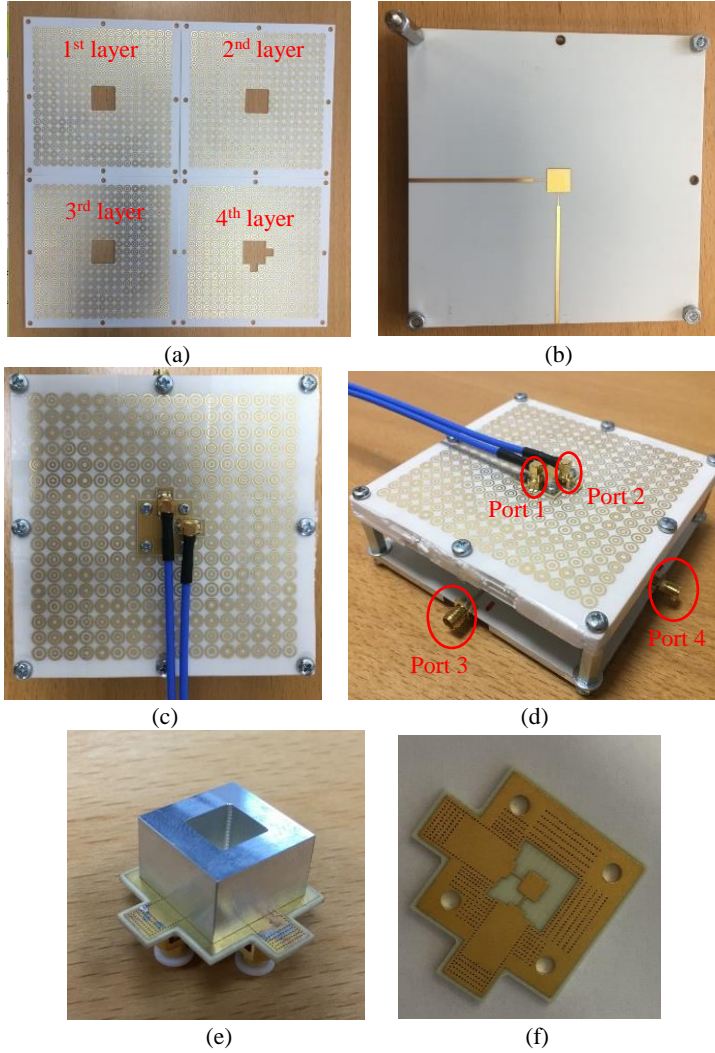


Fig. D. 17. Prototypes of the proposed shared-aperture antenna. (a). The front view of the four layers used to construct the shared aperture. (b). Front view of the dual-polarized patch antenna in the low-frequency band. (c). Front view of the proposed shared-aperture antenna. (d). Perspective view of the proposed shared-aperture antenna. (e). Perspective view of the dual-polarized SIW-based patch antenna in the high-frequency band. (f). Front view of the dual-polarized SIW-based patch antenna in the high-frequency (metal cavity is not shown here) (Notes: Port 1 and Port 3 have the same polarization, Port 2 and Port 4 have the same polarization.)

A. *S*-parameter

The *S*-parameters of the proposed shared-aperture antenna are measured with

Keysight N5227A Power Network Analyzer (PNA). Firstly, the S-parameter of the proposed shared- aperture antenna in the low-frequency band is measured and shown in Fig. D. 18(a), where the simulated results are also plotted for comparison. As seen in Fig. D. 18(a), the measured and simulated results agree with each other well except for a small frequency shifting (around 50 MHz). The measured results show a -10-dB bandwidth from 9.75 to 10.2 GHz with an absolute bandwidth of 450 MHz, the isolations between the two ports are better than 30 dB within the entire bandwidth.

The S-parameter of the proposed shared-aperture antenna in the high-frequency band is also measured. As seen in Fig. D. 18(b), the measured results agree very well with the simulated ones, revealing a -10-dB bandwidth from 26.7 to 29.4 GHz with an absolute bandwidth of 2.7 GHz, and isolations between the two ports better than 15 dB.

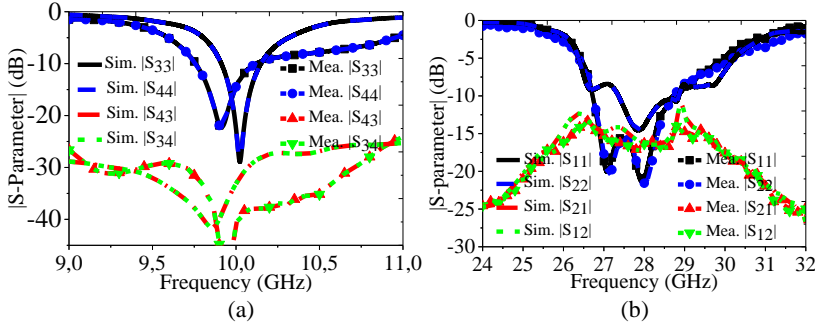


Fig. D. 18. The measured and simulated S-parameter of the proposed shared-aperture antenna. (a). In the low-frequency band. (b). In the high- frequency band.

B. Realized gain and radiation patterns

According to the measured reflection coefficients, the radiation patterns and realized gains are all measured in our available anechoic chamber. A dual-polarized horn antenna is used as a probe to measure the radiation patterns and realized gains of the proposed shared-aperture antenna. Besides, it should be mentioned that when one port is excited to measure the radiation patterns, the remaining ports in the low- and high-frequency bands are terminated with matching loads and the feeding cables for the high-frequency band are also kept since the four ports of the shared-aperture antenna may be excited simultaneously in practical applications.

The normalized radiation patterns of the proposed shared- aperture antenna are evaluated at 10 GHz. Port 3 and Port 4 (see Fig. D. 17) are measured and

shown in Fig. D. 19 and Fig. D. 20, respectively. The normalized co-polarizations in E- and H-plane are consistent between the simulated and measured results. The measured sidelobes are all better than -10 dB in both E- and H-plane. The measured normalized cross- polarizations in E- and H-plane are below -20 dB.

The normalized radiation patterns of the proposed shared-aperture antenna at 28 GHz are then measured. To minimize the blockage effects of the cables on the radiation patterns of the proposed shared-aperture antenna at 28 GHz, we fix the cables in the ± 45 deg planes of the shared aperture to alleviate their effects on radiation patterns in E- and H-plane as much as possible. Fig. D. 21 and Fig. D. 22 show the measured normalized radiation patterns when Port 1 and Port 2 are excited, respectively, where the simulated results are also plotted for comparison. It is observed that the co-polarizations in E- and H-plane between simulated and measured results are consistent with each other. Particularly, the measured main beam and the first radiation null are almost identical to the simulated counterparts. The measured sidelobes are all better than -18 dB in E- and H-plane. The measured normalized cross- polarizations in E- and H-plane are all below -30 dB at 28 GHz.

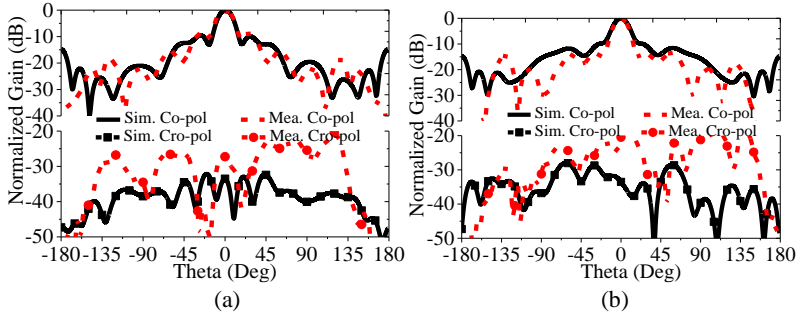


Fig. D. 19. Measured and simulated normalized radiation patterns of the proposed shared-aperture antenna at 10 GHz. (a). E-plane with Port 3 excited. (b). H-plane with Port 3 excited.

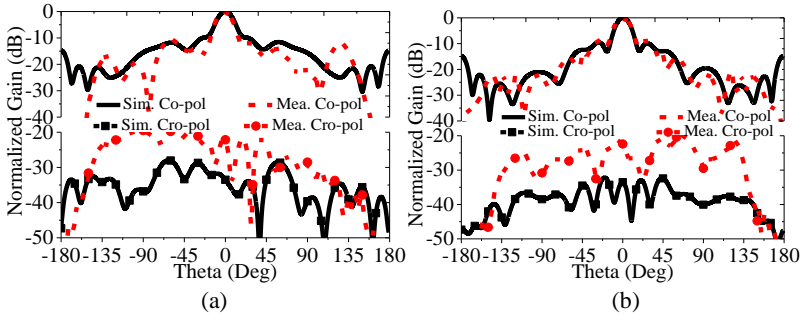


Fig. D. 20. Measured and simulated normalized radiation patterns of the proposed shared-aperture antenna at 10 GHz. (a). E-plane with Port 4 excited. (b). H-plane with Port 4 excited.

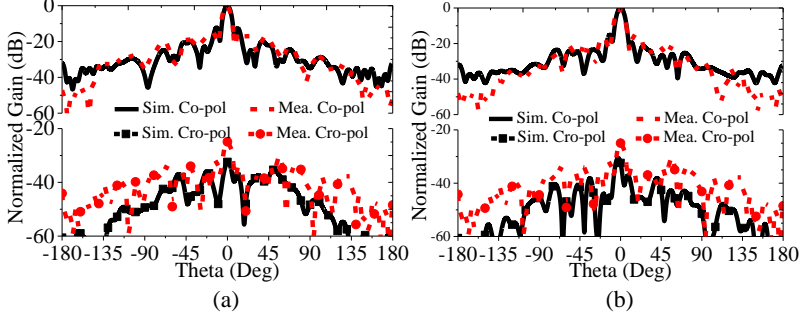


Fig. D. 21. Measured and simulated normalized radiation patterns of the proposed shared-aperture antenna at 28 GHz. (a). E-plane with Port 1 excited. (b). H-plane with Port 1 excited.

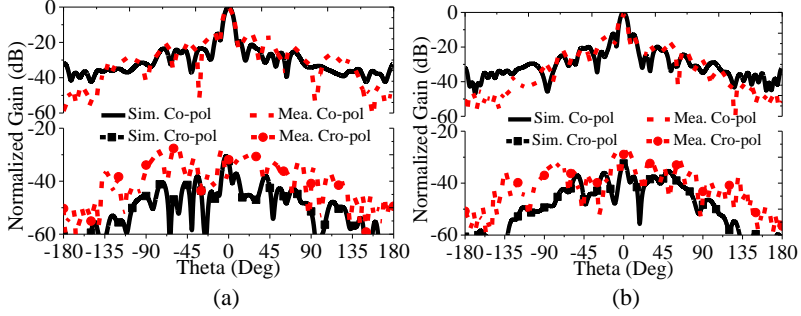


Fig. D. 22. Measured and simulated normalized radiation patterns of the proposed shared-aperture antenna at 28 GHz. (a). E-plane with Port 2 excited. (b). H-plane with Port 2 excited.

The realized gains of the proposed shared-aperture antenna in the low- and high-frequency band are also measured in the two orthogonal polarizations. It is found that the measured realized gains are highly consistent in the two polarizations both in low- and high-frequency bands. Fig. D. 23 shows the measured realized gains over the frequencies from 8 to 12 GHz and 26 to 29 GHz in the polarization that Port 1 and Port 3 operate for brevity. The corresponding simulated results are presented for comparison. As seen in Fig. 23, the measured realized gains are 13.8 dBi at 10 GHz and 23.6 dBi at 28 GHz.

Tab. D. III compares the proposed shared-aperture antenna with other state-of-the-art and similar works on some figure of merits. It is observed that the proposed shared-aperture antenna is highlighted by its easy realizations of

dual-polarization and high gain compared to references [1], [2], [5], [6] in which big footprint and complicated feeding networks are essential for dual-polarization and high gain implementations. In contrast, the proposed shared-aperture antenna does not need any feeding networks to achieve high gain and dual-polarization. The bandwidth of the proposed shared-aperture antenna in X-band is 6.0 %, which is mainly restricted by the inherently narrowband characteristics of a FP antenna that is typically characterized as a kind of resonant-based antenna. The similarly narrow bandwidths are also obtained in [2], [6], where FP antennas are adopted. It should be emphasized here that both of the feeding sources of the proposed shared-aperture antenna in X- and Ka-band radiate into free space through the physically same aperture like a dual-band reflectarray antenna reported in [11], resulting in a perfect aperture reuse efficiency. However, the dual-band reflectarray antenna in [11] suffers from the bulky volume (high profile) and high dependence of the two bands.

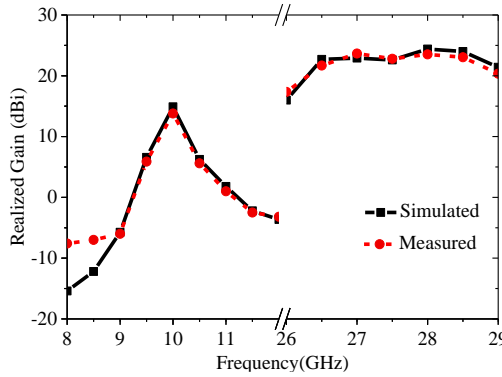


Fig. D. 23. Measured and simulated realized gains of the proposed shared-aperture antenna in the polarization that Port 1 and Port 3 operate.

Tab. D. III. Performance comparison of the proposed shared-aperture antenna with state-of-the-art and similar works

Ref	[1]	[2]	[5]	[6]	[11]	Proposed
f (GHz)	3.6; 25.8	3.6; 28	3.5; 60	5.3; 9.6	10.2; 22.0	10.0; 28.0
Gain (dBi)	10.88; 22.4	10.0; 14.0	7.3; 24	16.0; 20.0	26.2; 29.7	13.8; 23.6
*3dB bandwidth	27%; 5.8%	23.4%; 9.76%	5.7%; 3.3%	4.7%; 6.25%	16%; 9.1%	6.0%; 10.7%
#Pol	Single	Single	Single	Dual	Single	Dual
Size (mm * mm * mm)	90 * 90 *	92 * 92 *	80 * 86 *	140 * 140 *	300 * 300 *	85 * 85 *

	6.9	7.34	2.6	31	245	17
Aperture Reuse Efficiency	–	0.425	0.77	–	1.00	1.00
Feeding Network	Yes	Yes	Yes	Yes	No	No
Type	§MS; Slot	Slot; FP	Patch; Slot Array	FP; FP	Reflect arrays	FP; Folded TA antenna

*: 3dB gain drop bandwidth; #: Polarization; §: metasurface antenna; -: the shared-aperture antenna radiates through the different physical apertures in two different bands.

VI Conclusion

A dual-polarized and high-gain X/Ka-band shared-aperture antenna with a perfect aperture reuse efficiency is proposed in this paper. It is the first attempt to combine a Fabry-Perot and a folded transmitarray antenna operating in X- and Ka-band, respectively, to form a shared-aperture antenna. To implement the required shared aperture, a four-layered double-ring-based unit cell is configured and analyzed, where it is found that frequency responses of the unit cell in the low- and high- frequency bands are highly independent. Two dual-polarized patch antennas operating in X- and Ka-band are introduced to make the proposed shared-aperture antenna work in a dual-polarized manner. Since both of the two antennas radiate into free space through the same physical aperture, the aperture reuse efficiency of the proposed shared-aperture antenna is 100 %. The measured results are highly consistent with the simulated results, verifying the effectiveness of the proposed shared-aperture antenna.

Acknowledgement

The authors would like to thank the lab engineer Ben Krøyer for his help in soldering the connectors for the antenna, Kim Olesen for his kind assistance in the measurement setup.

Reference

- [1] T. Li, and Z. N. Chen, “Metasurface-based shared-aperture 5G S-/K-Band antenna using characteristic mode analysis,” *IEEE Transactions on Antennas and Propagation*, vol. 66, no. 12, pp. 6742-6750, Dec 2018.

- [2] T. Li, and Z. N. Chen, "Shared-aperture dual-band antenna for 5G applications," *IEEE Transactions on Antennas and Propagation*, vol. 68, no. 2, pp. 1128-67501133, Feb 2020.
- [3] Y. Chen, and R. Vaughan, "Dual-polarized L-band and single-polarized X-band shared-aperture SAR array," *IEEE Transactions on Antennas and Propagation*, vol. 66, no. 7, pp. 3391-3400, July 2018.
- [4] T. Li, H. Meng, and W. Dou, "Design and implementation of dual-frequency dual-polarization slotted waveguide antenna array for Ka-band application," *IEEE Antennas and Wireless Propagation Letters*, vol. 13, pp. 1317-1320, 2014.
- [5] J. Zhang, Y. Cheng, Y. Ding, and C. Bai, "A dual-band shared-aperture antenna with large frequency ratio, high aperture reuse efficiency, and high channel isolation," *IEEE Transactions on Antennas and Propagation*, vol. 67, no. 2, pp. 853-860, Feb 2019.
- [6] Qin, S. Gao, Q. Luo, C. Mao, C. Gu, G. Wei, J. Xu, J. Li, C. Wu, K. Zheng, and S. Zheng, "A simple low-cost shared-aperture dual-band dual-polarized high-gain antenna for synthetic aperture radars," *IEEE Transactions on Antennas and Propagation*, vol. 64, no. 7, pp. 2914-2922, July 2016.
- [7] Pozar, and S. Targonski, "A shared-aperture dual-band dual-polarized microstrip array," *IEEE Transactions on Antennas and Propagation*, vol. 49, no. 2, pp. 150-157, Feb 2001.
- [8] L. Kong, and X. Xu, "A compact dual-band dual-polarized microstrip antenna array for MIMO-SAR applications," *IEEE Transactions on Antennas and Propagation*, vol. 66, no. 5, pp. 2374-2381, May 2018.
- [9] C. Mao, S. Gao, Q. Luo, T. Rommel, and Q. Chu, "Low-cost X/Ku/Ka-band dual-polarized array with shared aperture," *IEEE Transactions on Antennas and Propagation*, vol. 65, no. 7, pp. 3520-3527, July 2017.
- [10] J. Zhang, W. Wu, and D. Fang, "Dual-band and dual-circularly polarized shared-aperture array antennas with single-layer substrate," *IEEE Transactions on Antennas and Propagation*, vol. 64, no. 1, pp. 109-116, Jan 2016.
- [11] R. S. Malfaiani, and Z. Atlasbaf, "Design and implementation of a dual-band single layer reflectarray in X and Ka bands," *IEEE*

- Transactions on Antennas and Propagation*, vol. 62, no. 8, pp. 4425-4431, Aug 2014.
- [12] Y. Chen, J. Zhao, and S. Yang, "A novel stacked antenna configuration and its applications in dual-band shared-aperture base station antenna array design," *IEEE Transactions on Antennas and Propagation*, vol. 67, no. 12, pp. 7234-7241, Feb 2019.
 - [13] K. Naishadham, R. Li, L. Yang, T. Wu, W. Hunsicker, and M. Tentzeris, "A shared-aperture dual-band planar array with self-similar printed folded dipoles," *IEEE Transactions on Antennas and Propagation*, vol. 61, no. 2, pp. 606-613, Feb 2013.
 - [14] Abdelrahman, A. Elsherbeni, and F. Yang, "Transmission phase limit of multilayer frequency selective surfaces for transmitarray designs," *IEEE Transactions on Antennas and Propagation*, vol. 62, no.2, pp. 690-697, Feb 2014.
 - [15] M. Pozar, *Microwave Engineering*, 3rd, John Wiley & Sons, Inc., New York, 2005.
 - [16] P. Mei, S. Zhang, X. Lin, and G. F. Pedersen, "Design of an absorptive Fabry-Perot polarizer and Its application on antenna," *IEEE Antennas and Wireless Propagation Letters*, vol. 18, no.7, pp. 1352-1356, July 2019.
 - [17] N. Nguyen-Trong, H. Tran, T. Nguyen, and A. Abbosh, "Wideband Fabry-Perot antennas employing multilayer of closely spaced thin dielectric slabs," *IEEE Antennas and Wireless Propagation Letters*, vol. 17, no.7, pp. 1354-1358, July 2018.
 - [18] N. Guerin, S. Enoch, G. Tayeb, P. Sabouroux, P. Vincent, and H. Legay, "A metallic Fabry-Perot directive antenna," *IEEE Transactions on Antennas and Propagation*, vol. 54, no. 1, pp. 220-224, Jan. 2006.
 - [19] J. S. Colburn, Y. R. Samii, "Patch antennas on externally perforated high dielectric constant substrates," *IEEE Transactions on Antennas and Propagation*, vol. 47, no. 12, pp. 1785-1794, Dec. 1999.
 - [20] J. Huang, "The finite ground plane effect on the microstrip antenna radiation patterns," *IEEE Transactions on Antennas and Propagation*, vol. AP-31, pp. 649-653, July. 1983.
 - [21] V. Trentini, "Partially reflecting sheet arrays," *IRE Transaction on*

Antennas and Propagation, vol. AP-4, no. 4, pp. 666-671, Oct. 1956.

- [22] <https://fractory.com/cnc-machining-services/>

Paper E

Design of a Triple-band Shared-Aperture Antenna with
High Figures of Merit

Peng Mei, Xian Qi Lin, Gert Frølund Pedersen, Shuai
Zhang

This paper has been published as early access by
IEEE Transactions on Antennas and Propagation, DOI:
10.1109/TAP.2021.3090837

© 2021 IEEE

The layout has been revised and reprinted with permission.

Abstract

This communication develops a triple-band shared-aperture antenna operating at X/K/Ka-band with high figures of merit such as high aperture reuse efficiency, simple configuration to achieve high gain. The proposed antenna is implemented by integrating a Fabry-Perot (FP) cavity antenna operating at X-band into a dual-band reflectarray antenna enabled by frequency selective surfaces (FSSs). The unit cells (UCs) to form the phase-shifting surfaces for the dual-band reflectarray antenna can offer partial reflectance/transmission abilities at X-band simultaneously, thereby enabling the implementation of a FP cavity antenna. The frequency responses of the proposed antenna are highly independent at X/K/Ka-band, which facilitates the design and optimization. For demonstration, a prototype has been described, fabricated, and measured. The simulated results present 3-dB gain bandwidths of 11.2% (8.4 to 9.4 GHz), 10.0% (24 to 26.6 GHz), and 13.3% (35 to 40 GHz), which are all experimentally verified. The measured results also present a peak gain of 16.8 dBi at 9.0 GHz, 23.8 dBi at 26 GHz, and 26.7 dBi at 38 GHz.

I Introduction

A shared-aperture antenna is a kind of antenna that typically combines multiple antennas in an efficient architecture to make all sub-antennas radiation through a shared aperture. Shared-aperture antennas, therefore, feature high space reuse efficiencies and multiband for multiservice applications, attracting lots of attention and interest in wireless communications.

The past few years have witnessed the developments and progress of shared-aperture antennas [1]-[13]. Most of the reported literature mainly focused on implementations of dual-band shared-aperture antennas [1]-[10]. A straightforward approach to realize a dual-band shared-aperture antenna is to interleave two patch antenna arrays with different sizes in the same aperture as reported in [1],[2], where two feeding networks are needed accordingly to excite the two antenna arrays. This approach is, however, not suitable for large-scale antenna arrays as the feeding networks would be very complicated and their losses would be high as well, especially at the millimeter-wave bands. Subsequently, other types of antennas are attempted to design shared-aperture antennas. Among them, a slot antenna (array) is one of the widely used sub-antennas, which usually operates at the millimeter-wave band [3]-[6]. The main drawback of a slot antenna (array) lies in its difficulties in the realization

of dual-polarization for the corresponding shared-aperture antenna. In [7], Chen et al. proposed a dual-polarized shared-aperture antenna by stacking dipole antennas operated at 600-900 MHz and 3.5-4.9 GHz, where the dipole array operating at the high-frequency band was located above the one operating at the low-frequency band with a certain separation. The stacking configuration makes full use of the space but is not suitable at the millimeter-wave band.

One of the considerations for a shared-aperture antenna is its number of operating bands. From the practical application viewpoint, a shared-aperture antenna covering as many as possible different bands is preferred for multiservice applications. To the authors' best knowledge, there is rare literature to report triple-band shared-aperture antennas [11]-[13] since it is challenging to find out three sub-antennas and combine them efficiently to radiate through the same aperture. In [11], [12], the authors achieved triple-band and dual-polarized shared-aperture antennas by employing the approach used in [1],[2]. It could be observed that feeding networks were much more complicated. The stacking configuration used in [7] was also expanded to design a triple-band shared-aperture antenna operated at sub-6GHz as reported in [13].

This communication proposed a design methodology that is distinguished from the techniques described in [11]-[13] to achieve a triple-band shared-aperture antenna with high figures of merit, such as high aperture reuse efficiency, simple configuration to achieve high gain. The methodology is inspired by dual-band reflectarray antennas [9], [10], [14], [15] and Fabry-Perot (FP) cavity antennas [8], [16], [17], where a FP cavity antenna can be properly integrated into a dual-band reflectarray antenna. For demonstration, a triple-band shared-aperture antenna operated at X/K/Ka-band has been described, fabricated, and measured. The FP cavity is designed to work from 8.25 to 9.4 GHz, while the operating bands of the dual-band reflectarray antenna are 24 to 28 GHz and 35 to 40 GHz, respectively. Besides, the proposed antenna is possible to realize dual/circular polarization if a dual-/circular-polarized feed source is applied, since the unit cells of the design are symmetrical and polarization-insensitive. Compared to our previous work in [8], where a dual-band shared-aperture antenna was performed by combining a FP cavity antenna and a folded transmitarray antenna, the proposed shared-aperture here is triple-band, and the bandwidth of the FP cavity antenna at the low-frequency band is much wider as the bandwidth of partial reflectance/transmission of the proposed UC is wider and a matching layer is

introduced to improve the impedance match. Moreover, the proposed antenna shows high independence among the three operating bands, where the operating frequencies and radiation performance can be controlled separately.

The rest of this communication is organized as follows. The UCs to construct the phase-shifting surfaces are presented in Section II. The implementation of the proposed triple-band shared-aperture antenna is given in Section III. The simulated and measured results are then given in Section IV. Finally, conclusions are drawn in Section V.

II Unit cell designs and analysis

The schematic diagram of the proposed triple-band shared-aperture antenna is presented in Fig. E. 1. It consists of two reflectarray antennas and a Fabry-Perot (FP) cavity antenna, where the two reflectarray antennas respectively operate at the middle- and high-frequency bands, and the FP cavity antenna works at the low-frequency band. To implement such a triple-band shared-aperture antenna, the phase-shifting surface for high frequency should satisfy the following conditions: a). phase-shifting capability at the high-frequency band; b). be transparent at the middle-frequency band; c). partial reflection/transmission at the low-frequency band. By contrast, the phase-shifting surface for middle frequency is required to provide: a). phase-shifting ability at the middle-frequency band; b). be fully reflective at the low-frequency band. It is also preferred that the frequency responses at the low-, middle-, and high-frequency bands are highly independent so that we can control the performance at different bands separately to facilitate the design.

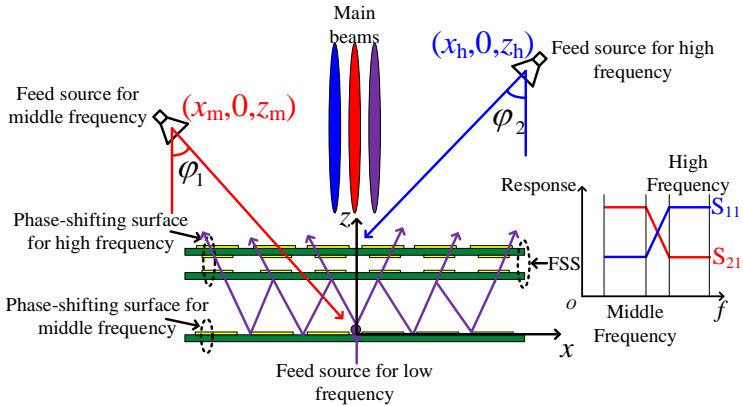


Fig. E. 1. The schematic diagram of the proposed triple-band shared-aperture antenna.

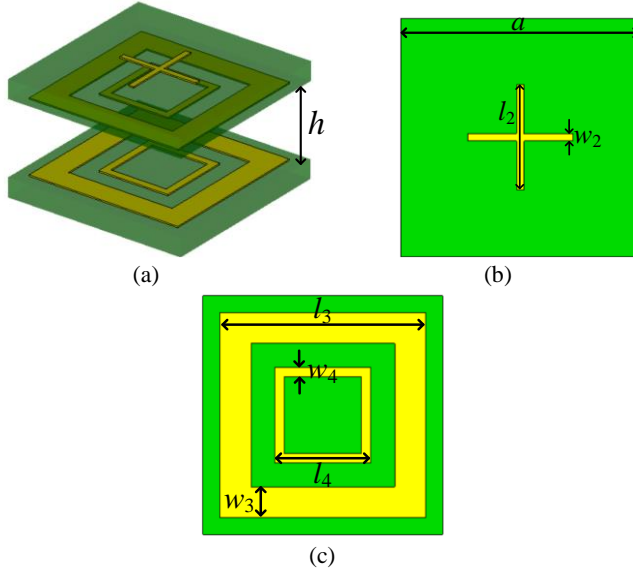


Fig. E. 2. Geometries of the UC for implementation of phase shifting surface at the high-frequency band. (a). Perspective view (transparent) (b). Front view. (c). Front view of the FSS. ($a = 5$ mm, $h = 2$ mm, $w_2 = 0.15$ mm, $l_3 = 4.3$ mm, $w_3 = 0.65$ mm, $l_4 = 2.0$ mm, $w_4 = 0.2$ mm.)

A. Analysis of the UC for implement of the phase-shifting surface at the high-frequency band.

The geometries shown in Figs. E. 2(a) and (b) are perspective and front views of the UC for the implementation of the phase-shifting surface at the high-frequency band. This UC consists of two double-square loops and a cross-shaped dipole. Two double-square loops are printed on two substrates with a separation of h , and a cross-shaped dipole is printed on the other side of the substrate. The substrates used here are Rogers RO4003C with a dielectric constant of 3.55, a loss tangent of 0.004, and a thickness of 0.508 mm. The two-layered double-square loops act as a frequency selective surface (FSS). In this design, the dimensions of the FSS are properly decided to make it fully reflective at the high-frequency band of 35-40 GHz and transparent at the middle-frequency band of 24-28 GHz simultaneously.

The frequency responses of the UC are simulated with CST Microwave Studio Software, where the periodic boundary conditions are imposed on the UC to simulate an infinite surface to obtain the desired results. As seen in Fig. E. 3(a), the UC can offer a partial reflection/transmission from 5 to 11 GHz, a bandpass response from 24 to 28 GHz, and a full reflection from 35 to 40 GHz.

The full reflection implies that the FSS can act as a metal ground from 35 to 40 GHz functionally. For such a UC, the cross-shaped dipole on the substrate can be properly sized to offer desired phase shifts at the high-frequency band by varying its length.

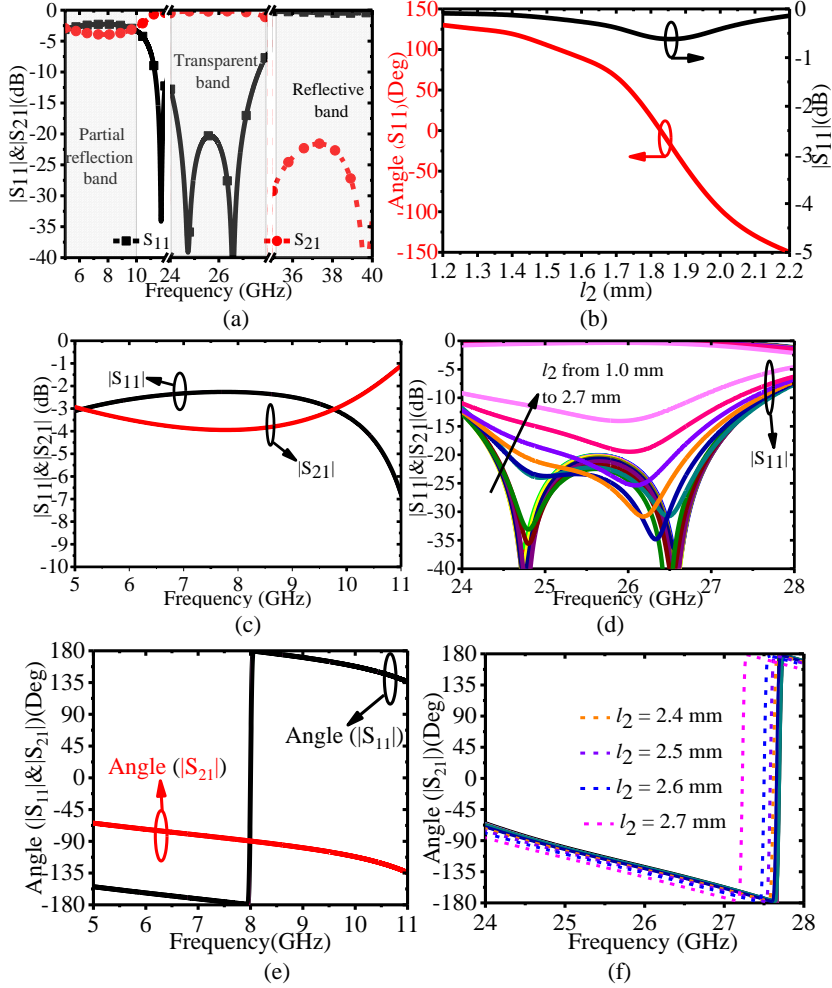


Fig. E. 3. Frequency responses of the UC: (a). $|S_{11}|$ and $|S_{21}|$ in three bands. (b). Reflection phase and amplitude with different l_2 at 38 GHz. (c). $|S_{11}|$ and $|S_{21}|$ from 5 to 11 GHz with l_2 varied from 1.0 to 2.7 mm. (d). $|S_{11}|$ and $|S_{21}|$ from 24 to 28 GHz with l_2 varied from 1.0 to 2.7 mm. (e). Reflection and transmission phases from 5 to 11 GHz with l_2 varied from 1.0 to 2.7 mm. (f). Transmission phase of the UC from 24 to 28 GHz with l_2 varied from 1.0 to 2.7 mm.

To check the effects of the length of the cross-shaped dipole on the UC frequency responses at low and middle frequencies, the reflection/

transmission amplitudes and phases are simulated with different values of l_2 . As seen in Figs. E. 3(c) and (e), the frequency responses of the UC are quite stable from 5 to 11 GHz as all curves are completely overlapped when l_2 changes from 1.0 to 2.7 mm, which implies the high independence of the UC between the low- and high-frequency bands. Likewise, the frequency responses of the UC from 24 to 28 GHz with different l_2 are plotted in Figs. E. 3(d) and (f). It is observed that $|S_{11}|$ starts to be worse when l_2 is longer than 2.4 mm. Besides, the transmission phase of the UC provides more phase delay when l_2 is larger than 2.2 mm. Specifically speaking, the transmission phase of the UC is a fixed value (-118 degree at 26 GHz for example) when l_2 is tuned from 1.0 to 2.2 mm; while it is varied from -118 to -135 degrees gradually when l_2 is tuned from 2.2 to 2.7 mm.

The frequency responses in Figs. E. 3(c)-(f) also indicate that the UC is more vulnerable to be affected with different values of l_2 at the middle-frequency band, which should be avoided in the proposed triple-band shared-aperture antenna design. Here, we adopt a compromising approach that keeps l_2 less than 2.2 mm to eliminate the impacts. As seen in Fig. E. 3, the S-parameter at the middle-frequency band is extremely stable when l_2 is tuned from 1.2 to 2.2 mm; and within this tuning range, the UC can offer 270 degrees reflection phase coverage at 38 GHz as observed from Fig. E. 3(b). This approach, however, will sacrifice the phase-shifting abilities of the UC, resulting in a slightly degraded realized gain of the proposed antenna at the high-frequency band.

Compared to our previous work in [8], the bandwidth of the partial reflection/transmission of the proposed UC at the low-frequency band is much wider, which is mainly attributed to the two-layered UC used here while it is a four-layered one in [8]. The four-layered UC can introduce more reflection zeros at the low-frequency band to generate multiple narrow bands, resulting in the narrow bandwidth of the partial reflectance/transmission of the UC. The wider bandwidth of the proposed two-layered UC can contribute to the wide bandwidth of the FP cavity antenna, which will be demonstrated in the following.

B. Analysis of the UC for implement of the phase-shifting surface at the middle-frequency band.

The geometries of the UC to implement the phase-shifting surface at the middle-frequency band are shown in Fig. E. 4, where a short cross-shaped dipole is stacked on a long and grounded cross-shaped dipole. The length of

the short cross-shaped dipole is proportional to the long one. Both the cross-shaped dipoles are printed on Rogers RO4003C substrate with a dielectric constant of 3.55, a loss tangent of 0.004, and a thickness of 0.508 mm. A bonding film made of Rogers RO4450F is sandwiched between the two substrates to firmly connect them. The Rogers RO4450F used here is with a dielectric constant of 3.52, a loss tangent of 0.0029, and a featured thickness of 0.202 mm.

Likewise, for such a UC, the phase shifts can be tuned by simply varying the length of the cross-shaped dipole. Fig. E. 5 gives the reflection phase and amplitude of the UC at 26 GHz with different values of l , where a full phase-cycle (2π) is observed and the reflection loss is less than 0.5 dB when l is tuned from 2.4 to 4.0 mm.

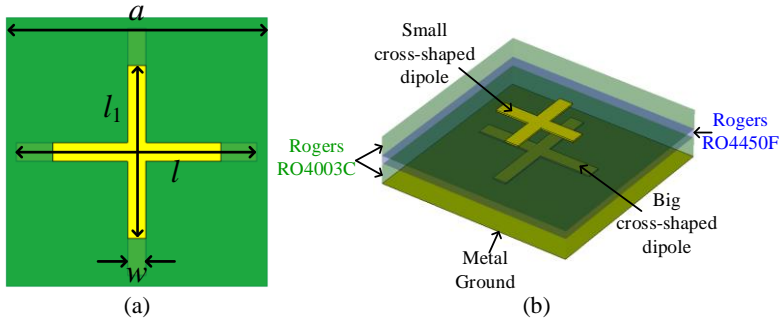


Fig. E. 4. Geometries of the UC for implementation of phase shifting surface at the middle-frequency band. (a). Front view. (b). Perspective view (transparent). ($a = 5$ mm, $h = 2$ mm, $l_1 = 0.7l$, $w = 0.35$ mm.)

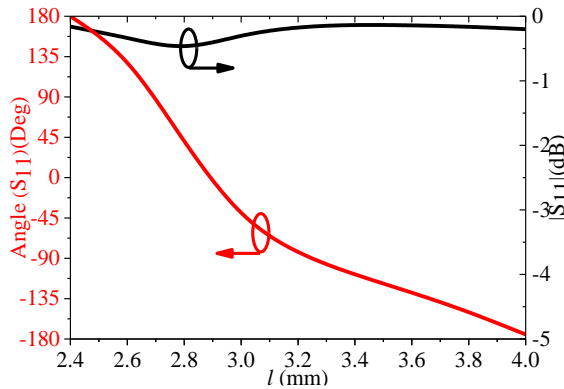


Fig. E. 5. Reflection phase and amplitude of the UC shown in Fig. 4 with different values of l at 26 GHz.

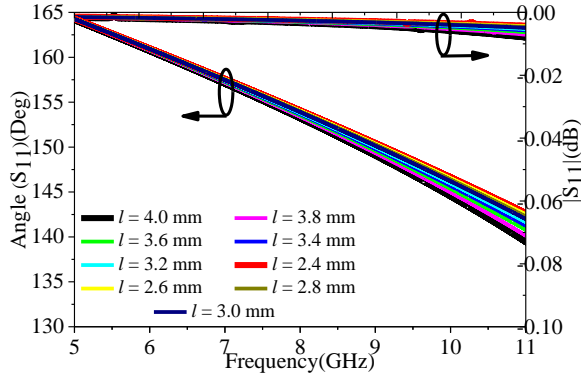


Fig. E. 6. Reflection phase and amplitude of the UC shown in Fig. 4 at the low-frequency band with different values of l from 5 to 12 GHz.

The reflection phase and amplitude of the UC at the low-frequency band are also examined with different values of l . As seen in Fig. E. 6, a full reflectance can be observed from 5 to 11 GHz with different l , where at 5 and 11 GHz the reflection amplitude difference is 0.00027 and 0.00517 dB, respectively, while the reflection phase difference is around 0.12 and 3.0 degrees, respectively. Fig. E. 6 also indicates good independence of the UC at low and middle frequencies.

C. Analysis of the UC for implement of the phase-shifting surface at the low-frequency band.

The phase-shifting surfaces for the middle and high-frequency bands should also satisfy the conditions to form a FP cavity antenna as seen in Fig. E. 1. As is known to all, the superstrate and metal ground for a FP cavity antenna are usually uniform and homogenous so that they can provide the same reflection/transmission amplitudes and reflections at any point on them to make the electric field on the aperture of the superstrate in phase, leading to a high gain. However, since the UCs constituting the phase-shifting surfaces are not physically identical, their reflection/transmission amplitudes and phases should be examined with different dimensions at the low-frequency band to check their feasibilities for the implementation a FP cavity antenna.

We extract the reflection/transmission amplitudes and phases at 9 GHz from Figs. E. 3(c) and (f) to plot their relations with different l_2 as shown in Fig. E. 7(a), it is observed that the reflection/transmission amplitudes and phases can keep the same when l_2 varies from 1.2 to 2.2 mm. Likewise, the reflection amplitude and phase at 9 GHz are also extracted from Fig. E. 6 and plotted

with different values of l as shown in Fig. E. 7(b), where the reflection amplitudes are almost the same and the imbalance of the reflection phase is about 1.3 degrees when l changes from 2.4 to 4.0 mm. The stable properties of the phase-shifting surfaces at the low-frequency band indeed make them feasible to implement a FP cavity antenna. Besides, the reflection/transmission amplitudes at the low-frequency band can be controlled by tuning the dimensions of the outer square loops of the FSS, which was described in detail in our previous work [8].

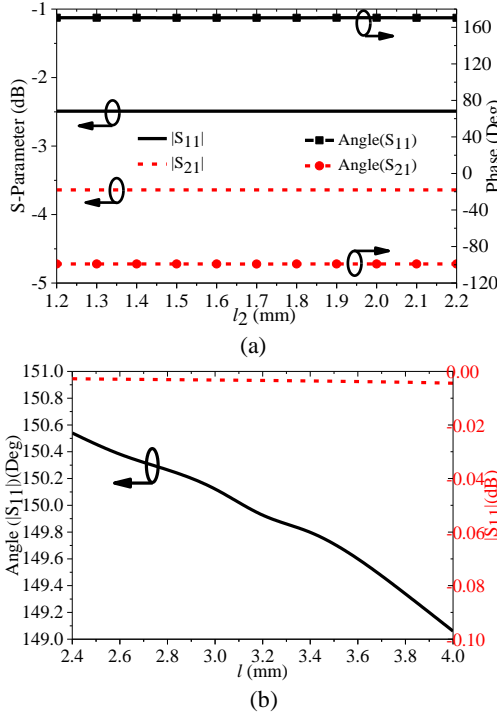


Fig. E. 7. Phases and amplitudes of the UCs. (a). Reflection/transmission amplitudes and phases at 9.0 GHz from Figs. 3 (c) and (f). (b). Reflection amplitude and phase at 9.0 GHz from Fig. E. 6.

III Triple-band shared-aperture antenna implementation

In this section, the proposed triple-band shared-aperture antenna is implemented based on the proposed UCs. For demonstration, both the phase-shifting surfaces for middle and high-frequency bands are composed of 400 UCs (20×20 UCs) considering the compromise between the realized gains and simulation time. As seen from the schematic diagram in Fig. E. 1, the

positions of the feed sources for middle and high frequency are associated with the air separation h_a . The value of h_a is calculated by using the following formula:

$$-2\frac{2\pi}{c}fh_a - \varphi_{PSH} - \varphi_{PSM} = 2n\pi, n = 0, \pm 1, \pm 2, \pm 3, \dots \quad (1)$$

where φ_{PSH} and φ_{PSM} are reflection phases of the phase-shifting surfaces for the high and middle frequency at the low-frequency band, respectively, as can be obtained from Fig. E. 7. c is the light velocity, and f is the frequency of interest. Using Eq. (1), the value of h_a equals 15.0 mm when f is 9.0 GHz.

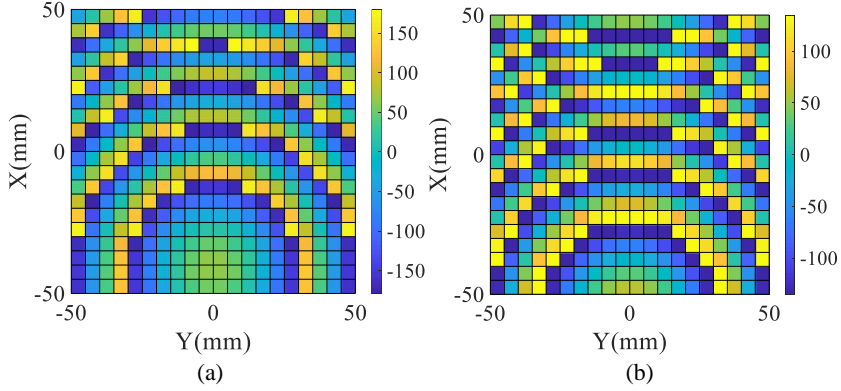


Fig. E. 8. Phase distribution on the plane of the phase-shifting surface. (a). At 26 GHz. (b). At 38 GHz.

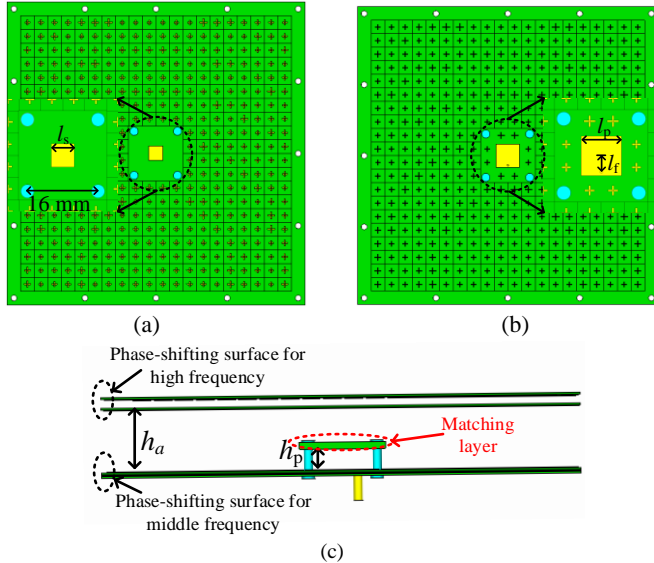


Fig. E. 9. The final model of the proposed triple-band shared-aperture antenna. (a). Front view of the matching layer. (b). Front view of the phase-shifting surface for middle frequency band, where a patch antenna operated at X-band is integrated into it. (c). Side view. (The feed sources for middle and high frequency removed, $l_s = 5.2$ mm, $l_p = 8.6$ mm, $l_f = 3.5$ mm.)

In order to decrease the blockage effects of the feed sources, the offset feeding technique is adopted as shown in Fig. E. 1, where the feed sources are located at the two sides of the phase-shifting surfaces. We select an ultra-wideband and linearly-polarized commercial horn antenna with a small footprint as the feed source for both middle- and high-frequency bands to further minimize its blockage. Its gains and beamwidths with frequencies are fixed for the horn antenna, which can be obtained by simulating its model with CST software and verified by experimental measurements. In our design, the sizes of the phase-shifting surfaces and beamwidths of the horn antenna are known, only the height and offset angle of the feed sources need to be determined, where the illumination coverage and the edge/corner element effect can be evaluated accordingly. In [18], the authors claimed that a better efficiency is usually obtained when the feeding beam is directed to a point between the aperture center and the bisecting point of the aperture angle. After some trial and error simulations, the optimal positions (height and offset angle) of the feed sources are listed as follows: $x_m = 50$ mm, $z_m = 60$ mm, $\varphi_1 = 36^\circ$, $x_h = 55$ mm, $z_h = 110$ mm, $\varphi_2 = 30^\circ$.

Once the positions of the feed sources are determined, the phase distributions on the planes of the phase-shifting surfaces can be obtained at 26 and 38 GHz, which are plotted in Fig. E. 8. Besides, the illumination coverages can also be evaluated by checking the electric field distributions on the planes of the phase-shifting surfaces. The electric field at the edge element is around 12dB lower than the peak electric field at 26 and 38 GHz, which is a common value in reflectarray and transmitarray antenna designs. For very few corner elements, the electric field is around 14 dB lower than the peak value at 26 and 38 GHz. Such illumination coverages of the phase-shifting surfaces contribute to the sidelobe level of the proposed antenna at the middle- and high-frequency bands, which will be demonstrated from the radiation patterns at 26 and 38 GHz. Based on the phase distributions, the phase-shifting surfaces are implemented by the proposed UCs.

From Fig. E. 1, the feed source for low frequency should locate between the two phase-shifting surfaces. Here, the feed source is integrated into the phase-shifting surfaces for middle frequency as shown in Fig. E. 9, where a square patch is properly sized to make it work at around 9 GHz. The inner and

outer radius of the coaxial cable to excite the square patch are 0.27 and 0.81 mm, respectively.

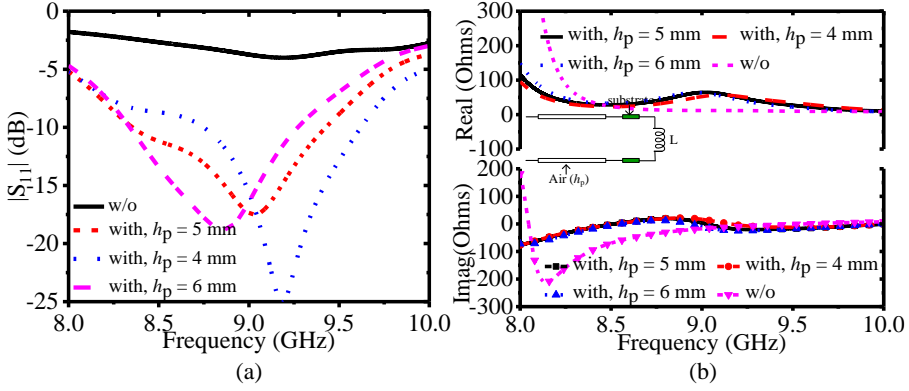


Fig. E. 10. The reflection coefficient and input impedance of the proposed triple-band shared-aperture antenna at the low-frequency band. (a). Reflection coefficient. (b). Input impedance.

For such a square patch antenna, the movement of the feeding point (l_f) is a widely-used technique to optimize the impedance match and reflection coefficient. However, for the FP cavity antenna in the proposed triple-band shared-aperture antenna, the patch antenna only serves as a feed source, both the phase-shifting surfaces affect the input impedance of the FP cavity antenna. The simulations reveal that the movement of the feeding point (l_f) and resizing the square patch are not able to improve the impedance match and reflection coefficient. Here, a matching layer (ML) located above the square patch (as shown in Fig. E. 9(c)) is introduced to improve the impedance match. The substrate of the matching layer is a 1.524 mm-thick Rogers RO4003C. Fig. E. 10 gives the reflection coefficient of the proposed triple-band shared-aperture antenna from 8 to 10 GHz. It is observed that the use of the ML improves the impedance match significantly. Moreover, the reflection coefficient can also be tuned by adjusting the value of h_p . The mechanism of the ML be able to improve the impedance match at the low-frequency band can be explained from the equivalent circuit and input impedance. The approximate equivalent circuit of the ML is shown in the inset of Fig. E. 10(b), where the square metal patch contributes to the inductor. As the electrical lengths of the air space (h_p) and 1.524mm-thick substrate are much smaller than the wavelength at 9.0 GHz, the input impedance of the equivalent circuit can be inductive. The inductive impedance can compensate for the original capacitive impedance to modify the input impedance as observed in Fig. E. 10(b), thereby improving the impedance match of the proposed triple-band shared-aperture antenna at

the low-frequency band. It should be mentioned here that even though the ML is introduced, Eq.(1) still holds to calculate h_a as the size of the ML is much smaller than the phase-shifting surfaces and most of the electromagnetic waves still experience multiple reflections among the phase-shifting surfaces.

IV Measurement and discussion

In this section, the proposed triple-band shared-aperture antenna has been fabricated and measured. All boards are produced with printed circuit board (PCB) technologies. Sixteen air holes with a diameter of 2 mm are drilled and distributed uniformly on the edges of every board for alignments. Fig. E. 11 shows the photograph of the proposed triple- band shared-aperture antenna and different board layers.

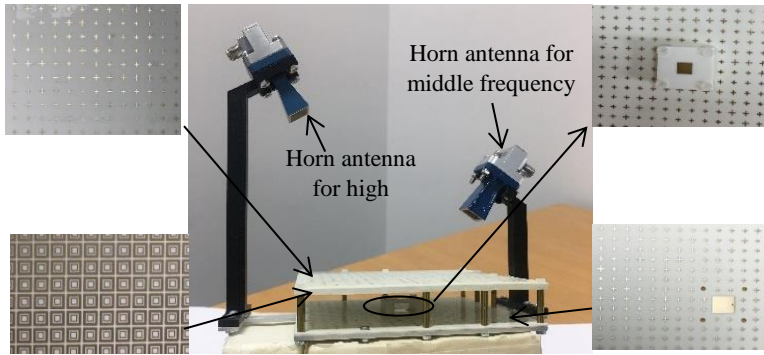


Fig. E. 11. The photograph of the proposed triple-band shared-aperture antenna.

A. *S-parameter*

The S-parameters of the proposed triple-band shared-aperture antenna are measured with Keysight N5227A Power Network Analyzer (PNA). The measured reflection coefficients at the low-, middle-, and high-frequency bands are shown in Fig. E. 12, where the simulated results are also plotted for comparison. As seen in Fig. E. 12, the measured and simulated results agree with each other. The measured reflection coefficients below -10 dB from 8.25 to 9.3 GHz, 24 to 28 GHz, and 35 to 40 GHz are demonstrated. The reflection coefficient at around 39.5 GHz is slightly higher than -10 dB, which is mainly due to the effects of the coaxial to waveguide transition instead of the proposed antenna itself.

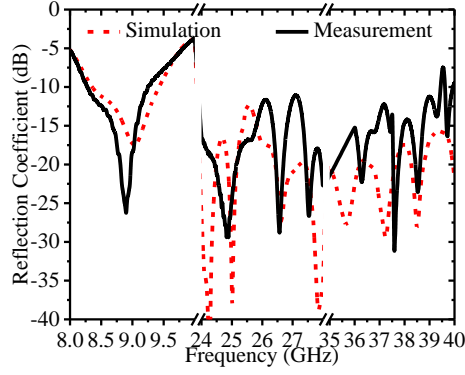


Fig. E. 12. Measured and simulated reflection coefficients of the proposed shared-aperture antenna at three different frequency bands.

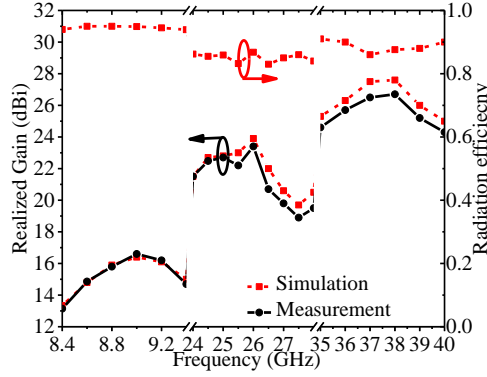


Fig. E. 13. Measured and simulated realized gains, and simulated radiation efficiency of the proposed shared-aperture antenna at three frequency bands.

B. Realized gain and radiation patterns

According to the measured reflection coefficients, the realized gains and radiation patterns are measured in our anechoic chamber. It should be mentioned that when one port is excited, the remaining ports operating at other frequency bands should be terminated with matching loads. As seen in Fig. E. 13, the measured and simulated realized gains of the proposed triple-band shared-aperture antenna at the low-frequency band are highly consistent, achieving a peak gain of 16.8 dBi at 9 GHz. The 11.2% 3dB gain bandwidth (from 8.4 to 9.4 GHz) mainly attributes to the wide bandwidth of the partial reflection/transmission and proper reflection phases of the phase-shifting surfaces at the low-frequency band. By contrast, the measured realized gains at the middle and high-frequency bands are slightly smaller (less than 1.0 dB)

than the simulated results. The aperture efficiency of the proposed antenna is 41.4 % at 9.0 GHz, 26.0 % at 26 GHz, and 29.2 % at 38 GHz, respectively. The gain-drop beyond 26 GHz at the middle-frequency band mainly due to the phase errors attributed by the oblique incidence effects of the UCs. The relatively big difference between the simulated and measured results at the high-frequency band is mainly due to the non-constant distance between the layers of the phase-shifting surface for high frequency (as shown in Fig. E. 9(c)) since there exists a slight bending and the air space (ha) is not exactly equal to 15.0 mm in the antenna assembling. The simulated radiation efficiency of the proposed antenna is also presented in Fig. E. 13, where above 85 % radiation efficiency can be observed over the three bands.

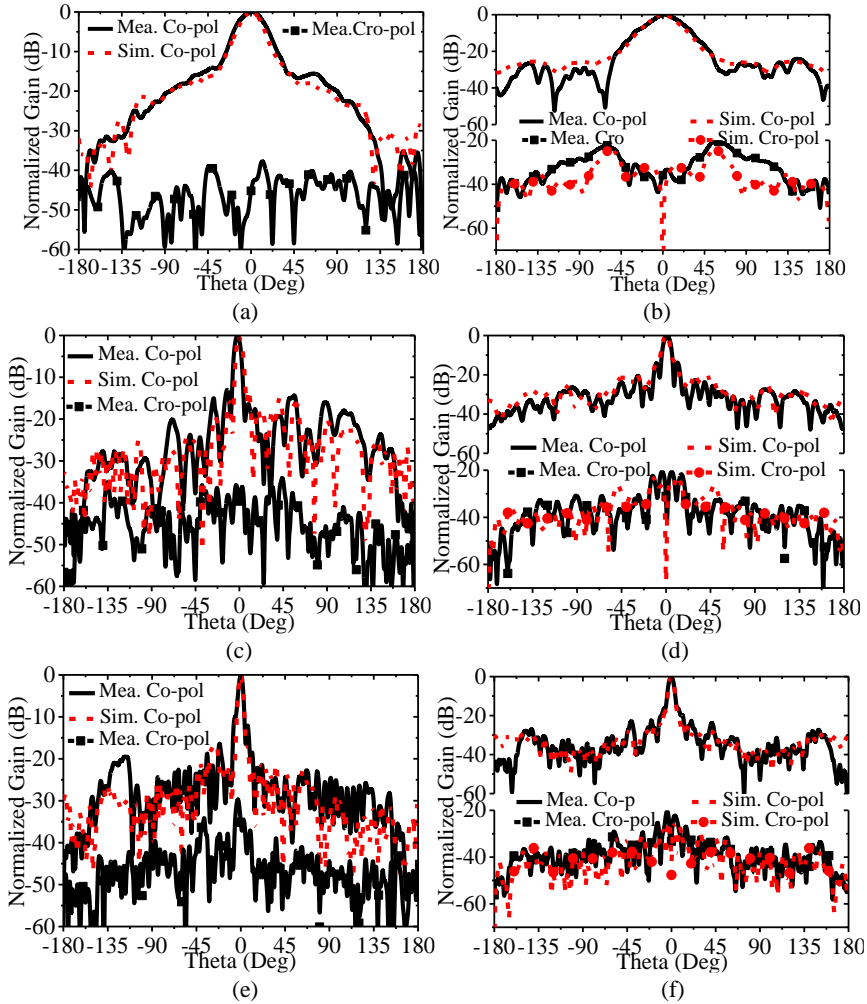


Fig. E. 14. Measured and simulated normalized realized gains of the proposed shared-aperture antenna. E-plane at: (a) 9.0 GHz, (c) 26.0 GHz, and (e) 38.0 GHz. H-plane at: (b) 9.0 GHz, (d) 26.0 GHz, and (f) 38.0 GHz.

The radiation patterns of the proposed triple-band shared-aperture antenna are measured. Fig. E. 14 presents the measured normalized radiation patterns at 9.0, 26.0, and 38.0 GHz, where the simulated counterparts are also plotted for comparison. As seen in Figs. E. 14(a) and (b), the measured co-polarization (co-pol) in E- and H-plane is highly consistent with the simulated result. The measured cross- polarization (cro-pol) in E- and H-plane is below -40 and -20 dB, respectively. At 26.0 GHz, the measured radiation patterns of co-pol in E- and H-plane agree with the simulated results. As seen in Figs. E. 14(c) and (d), the measured sidelobes are -18 and -20 dB in E- and H-plane, respectively; and the measured levels of cro-pol are below -35 and -20 dB in E- and H-plane, respectively. The measured and simulated radiation patterns of co-pol in E- and H-plane have a good agreement with each other at 38.0 GHz. From Figs. E. 14(e) and (f), the measured sidelobes are -19 and -20 dB in E- and H-plane, respectively; and the measured levels of cro-pol are below -30 and -20 dB in E- and H-plane, respectively.

The performance of the proposed antenna with other similar and state-of-the-art work is compared as shown in Tab. E. I. The proposed antenna is highlighted by its higher operating bands, the possibility of dual/circular polarization, simple configuration to achieve a high gain, and high aperture reuse efficiency as the FP cavity antenna makes full use of the phase-shifting surfaces for middle- and high-frequency bands. Since the frequency responses of the proposed antenna are highly independent among the three operating bands, the frequency ratio of the proposed antenna can be flexibly controlled by choosing the proper dimensions of the FSSs and phase-shifting unit cells.

Table. E. I. Comparison of the proposed antenna with other state-of-the-art triple-band shared-aperture antennas

Ref.	O_B, BW (GHz)	Gain (dBi)	R_E	F_R	ARE	Complex.
[11]	9.45-9.8, 3.6%	13.8	> 80%	1:	L	H
	14.6-15.6, 6.7%	18.1		1.57:		
	33-34.75, 5.3%	19.2		3.52		
	1.56-1.94, 21.7%	6.3		1:		

[12]	3.08-3.46, 11.6% 8.65-10.45, 18.9%	14.0 21.0	N. A	1.87: 5.46	L	H
#[13]	1.65-2.7, 50.2% 3.26-3.72, 13.1% 4.4-5.36, 17.5%	14.8 17.8 19.1	N. A	1: 1.60: 2.24	M	H
Pro.	*8.4-9.4, 11.2% 24-26.6, 10.0% 35-40, 13.3%	16.8 23.8 26.7	> 85%	1: 2.84: 4.21	H	S

O_B: operating band; BW: bandwidth; R_E: radiation efficiency; F_R: frequency ratio; ARE: aperture reuse efficiency; H: high; M: moderate; L: low; S: simple. #: 1×4 antenna array; *: 3dB gain bandwidth. Complex: complexity.

V Conclusion

A triple-band shared-aperture antenna with high figures of merit is described in this communication. A FP cavity antenna operated at X-band is integrated into a dual-band reflectarray antenna operated at K- and Ka-band to form the proposed antenna. By properly designing the phase-shifting surfaces for K- and Ka-band, the controls of the frequency responses of the proposed antenna can be highly independent at the three operating bands. For proof of the concept, a prototype has been designed, fabricated, and measured. It presents the 3-dB gain bandwidths of 11.2% (8.4 to 9.4 GHz), 10% (24 to 26.6 GHz), 13.3% (35 to 40 GHz), and the peak gains of 16.8 dBi at 9.0 GHz, 23.8 dBi at 26 GHz, 26.7 dBi at 38 GHz. Good agreement with the simulated results has been observed.

Reference

- [1] L. Kong, and X. Xu, "A compact dual-band dual-polarized microstrip antenna array for MIMO-SAR applications," *IEEE Transactions on Antennas and Propagation*, vol. 66, no. 5, pp. 2374-2381, May. 2018.
- [2] J. Zhang, W. Wu, and D. Fang, "Dual-band and dual-circularly polarized shared-aperture antenna with single-layer substrate," *IEEE Transactions on Antennas and Propagation*, vol. 64, no. 1, pp. 109-116, Jan. 2016.

- [3] T. Li, and Z. N. Chen, "Shared-surface dual-band antenna for 5G applications," *IEEE Transactions on Antennas and Propagation*, vol. 68, no. 2, pp. 1128-1133, Feb. 2020.
- [4] T. Li, and Z. N. Chen, "Metasurface-based shared-aperture 5G S-/K-Band antenna using characteristic mode analysis," *IEEE Transactions on Antennas and Propagation*, vol. 66, no. 12, pp. 6742-6750, Dec. 2018.
- [5] J. Zhang, Y. Cheng, Y. Ding, and C. Bai, "A dual-band shared-aperture antenna with large frequency ratio, high aperture reuse efficiency, and high channel isolation," *IEEE Transactions on Antennas and Propagation*, vol. 67, no. 2, pp. 853-860, Feb. 2019.
- [6] Y. Ding, and Y. Cheng, "Ku/Ka dual-band dual-polarized shared-aperture beam-scanning antenna array with high isolation," *IEEE Transactions on Antennas and Propagation*, vol. 67, no. 4, pp. 2413-2422, Apr. 2019.
- [7] Y. Chen, J. Zhao, and S. Yang, "A novel stacked antenna configuration and its applications in dual-band shared-aperture base station antenna array designs," *IEEE Transactions on Antennas and Propagation*, vol. 67, no. 12, pp. 7234-7241, Dec. 2019.
- [8] P. Mei, S. Zhang, and G. F. Pedersen, "A dual-polarized and high-gain X/Ka-band shared-aperture antenna with high aperture reuse efficiency," *IEEE Transactions on Antennas and Propagation*, vol. 69, no. 3, pp. 1334-1344, Mar. 2021.
- [9] R. S. Malfaiani, and Z. Atlasbaf, "Design and implementation of a dual-band single layer reflectarray in X and Ka bands," *IEEE Transactions on Antennas and Propagation*, vol. 62, no. 8, pp. 4425-4431, Aug. 2014.
- [10] T. Smith, U. Gothelf, O. Kim, and O. Breinbjerg, "An FSS-backed 20/30 GHz circularly polarized reflectarray for a shared-aperture L- and Ka-band satellite applications," *IEEE Transactions on Antennas and Propagation*, vol. 62, no. 2, pp. 661-668, Feb. 2014.
- [11] C. Mao, S. Gao, Q. Luo, T. Rommel, and Q. Chu, "Low-cost X/Ku/Ka-band dual-polarized array with shared aperture," *IEEE Transactions on Antennas and Propagation*, vol. 65, no. 7, pp. 3520-3527, Jul. 2017.

- [12] K. Li, T. Dong, and Z. Xia, "A broadband shared-aperture antenna L/S/X-band dual-polarized antenna for SAR applications," *IEEE Access*, vol. 7, pp. 51417-51425, June. 2019.
- [13] Zhou, B. Sun, Q. Liang, S. Wu, Y. Yang, and Y. Cai, "Tri-band dual-polarized shared-aperture antenna for 2G/3G/4G/5G base station application," *IEEE Transactions on Antennas and Propagation, Early Access*, vol. 69, no. 1, pp. 97-108, Jan. 2021.
- [14] R. Deng, F. Yang, S. Xu, and M. Li, "An FSS-backed 20/30-GHz dual-band circularly polarized reflectarray with suppressed mutual coupling and enhanced performance," *IEEE Transactions on Antennas and Propagation*, vol. 65, no. 2, pp. 926-931, Feb. 2017.
- [15] M. R. Chaharmir, and J. Shaker, "Design of a multilayer X-/Ka-band frequency-selective surface-backed reflectarray for satellite applications," *IEEE Transactions on Antennas and Propagation*, vol. 63, no. 4, pp. 1255-1262, Apr. 2015.
- [16] P. Mei, S. Zhang, X. Q. Lin, and G. F. Pedersen, "Design of an absorptive Fabry-Perot polarizer and its application on antenna," *IEEE Antennas and Wireless Propagation Letters*, vol. 18, no. 7, pp. 1352-1356, July. 2019.
- [17] N. Nguyen-Ttong, H. Tran, T. Nguyen, and A. Abbosh, "Wideband Fabry-Perot antennas employing multilayer of closely spaced thin dielectric slabs," *IEEE Antennas and Wireless Propagation Letters*, vol. 17, no. 7, pp. 1354-1358, July. 2018.
- [18] Yu, F. Yang, A. Z. Elsherbeni, J. Huang, and Y. Rahmat-Samii, "Aperture efficiency analysis of reflectarray antennas," *Microwave and Optical Technology Letters*, vol. 52, no. 2, pp. 364-372, Feb 2010.

ISSN (online): 2446-1628
ISBN (online): 978-87-7210-985-5

AALBORG UNIVERSITY PRESS